

AD-A040 030

DAYTON UNIV OHIO RESEARCH INST
NUMERICAL ANALYSES OF SOFT BODY IMPACTS ON RIGID AND DEFORMABLE--ETC(U)
DEC 76 M ROSENBLATT, G E EGGUM, L A DEANGELO F33615-75-C-5052

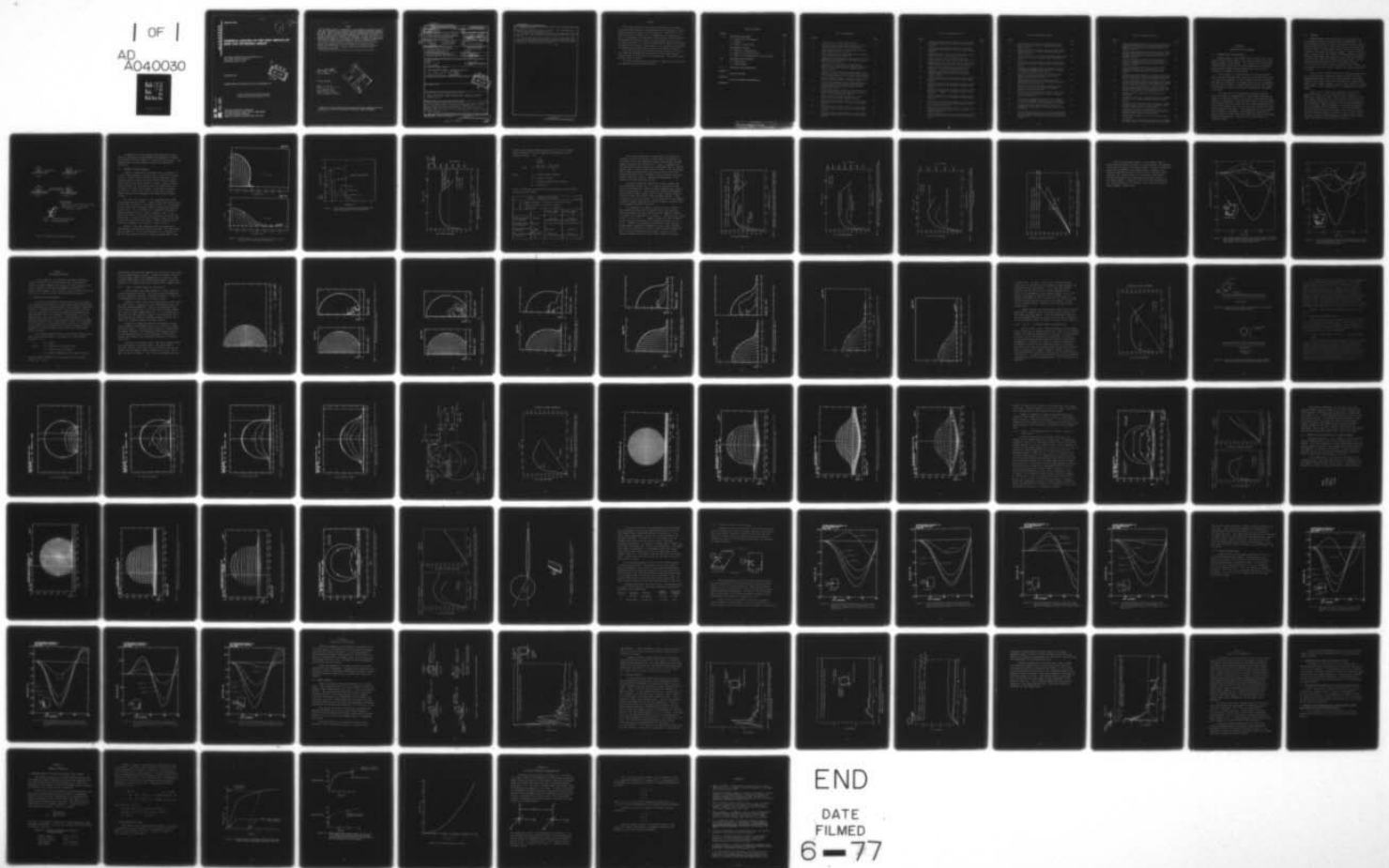
AFML-TR-76-202

F/G 21/5

NL

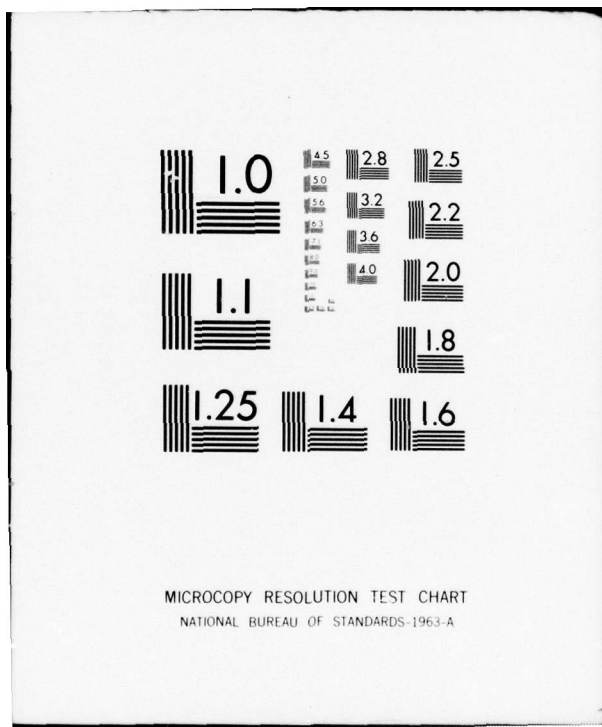
UNCLASSIFIED

| OF |
AD
A040030
EIE
EIE



END

DATE
FILMED
6-77



AU NO.
DDC FILE COPY

ADA040030

AFML-TR-76-2O2

1

1

NUMERICAL ANALYSES OF SOFT BODY IMPACTS ON RIGID AND DEFORMABLE TARGETS

CALIFORNIA RESEARCH AND TECHNOLOGY, INC.
6269 VARIET AVENUE, SUITE 200
WOODLAND HILLS CA 91367

DECEMBER 1976



INTERIM REPORT FOR PERIOD JULY 1975 to DECEMBER 1975

Approved for public release; distribution unlimited

AIR FORCE MATERIALS LABORATORY
AIR FORCE WRIGHT AERONAUTICAL LABORATORIES
AIR FORCE SYSTEMS COMMAND
WRIGHT-PATTERSON AIR FORCE BASE, OHIO 45433

NOTICE

When Government drawings, specifications, or other data are used for any purpose other than in connection with a definitely related Government procurement operation, the United States Government thereby incurs no responsibility nor any obligation whatsoever; and the fact that the government may have formulated, furnished, or in any way supplied the said drawings, specifications, or other data, is not to be regarded by implication or otherwise as in any manner licensing the holder or any other person or corporation, or conveying any rights or permission to manufacture, use, or sell any patented invention that may in any way be related thereto.

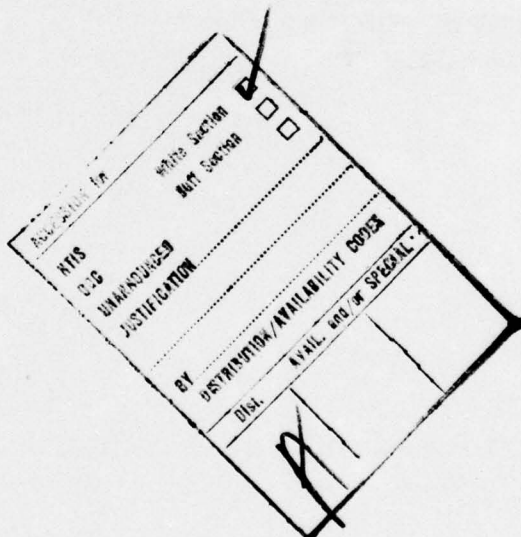
This report has been reviewed and cleared for open publication and/or public release by the appropriate Office of Information (OI) in accordance with AFR 190-170 and DODD 5230.9. There is no objection to unlimited distribution of this report to the public at large or by DDC to the National Technical Information Service (NTIS).

This technical report has been reviewed and is approved for publication.

James S. Wilbeck
J. S. Wilbeck, Capt. USAF
Project Engineer

FOR THE COMMANDER

G. E. Eichelman
G. E. Eichelman, Chief
Metals Behavior Branch
Metals & Ceramics Division
Air Force Materials Laboratory



Copies of this report should not be returned unless return is required by security considerations, contractual obligations, or notice on a specific document.

UNCLASSIFIED

SECURITY CLASSIFICATION OF THIS PAGE (When Data Entered)

(19) REPORT DOCUMENTATION PAGE

READ INSTRUCTIONS
BEFORE COMPLETING FORM

1. REPORT NUMBER AFML-TR-76-202	2. GOVT ACCESSION NO. 9	3. RECIPIENT'S CATALOG NUMBER
4. TITLE (and Subtitle) NUMERICAL ANALYSES OF SOFT BODY IMPACTS ON RIGID AND DEFORMABLE TARGETS		5. TYPE OF REPORT & PERIOD COVERED Interim Technical Report July 1975 - December 1975
6. AUTHOR(s) M. Rosenblatt, K. N. Kreyenhagen G. E. Eggum L. A. DeAngelo		7. PERFORMING ORGANIZATION NAME AND ADDRESS California Research and Technology, Inc. 6269 Variel Avenue, Suite 200 Woodland Hills CA 91367
8. CONTROLLING OFFICE NAME AND ADDRESS Air Force Materials Laboratory(LLN) Wright-Patterson Air Force Base OH 45433		9. PROGRAM ELEMENT, PROJECT, TASK AREA & WORK UNIT NUMBERS 62102F, 7351, 735106, 735106A1
10. MONITORING AGENCY NAME & ADDRESS (if different from Controlling Office) 12 92p.		11. REPORT DATE December 1976
		12. NUMBER OF PAGES 80
		13. SECURITY CLASS. (of this report) UNCLASSIFIED
		14a. DECLASSIFICATION/DOWNGRADING SCHEDULE
15. DISTRIBUTION STATEMENT (of this Report) Approved for public release; distribution unlimited. 16 7351 1706		
17. DISTRIBUTION STATEMENT (of the abstract entered in Block 20, if different from Report)		
18. SUPPLEMENTARY NOTES		
19. KEY WORDS (Continue on reverse side if necessary and identify by block number) Impact, Foreign Object Damage, Soft Body Impact, Bird Impact, Numerical Calculations of Impact, Finite Difference Codes, Impact Response, Jet Engine Fan Blades		
20. ABSTRACT (Continue on reverse side if necessary and identify by block number) A two-dimensional finite difference code, WAVE-L, was used to investigate the impact of soft bodies (birds) on both rigid and deformable targets. The soft body was numerically modeled as a water sphere. Three impact cases were examined: impacts onto rigid targets (both normal and oblique), impact onto a deformable target (a stainless steel disk) and impact onto the edge of a typical jet engine fan blade. For the impacts onto rigid targets the finite difference calculation was used to obtain the pressures produced at impact, the distribution of pressure over the		

105400

JF

UNCLASSIFIED

SECURITY CLASSIFICATION OF THIS PAGE(When Data Entered)

20. ABSTRACT (Continued)

target and the total force exerted on the target. These calculations were compared with experimentally measured values.

The impact onto a stainless steel disk was also modeled with the finite difference code. Plate deformation, impact pressures and forces were calculated.

The fan blade impacts were modeled in two phases. The impact loading pressures and forces were calculated with the finite difference model. The blade was then modeled with a three dimensional finite element code, NONSAP, using the finite difference pressures on impact.



UNCLASSIFIED

SECURITY CLASSIFICATION OF THIS PAGE(When Data Entered)

PREFACE

This report summarizes the numerical work performed by California Research and Technology, Inc., under subcontract to The University of Dayton Research Institute on Phase II of USAF Contract No. F33615-75-C-5052. The authors are Mr. M. Rosenblatt, Mr. G. E. Eggum, Mr. L. A. DeAngelo, and Mr. K. N. Kreyenhagen. The experimental work performed by The University of Dayton Research Institute on Phase II, entitled "Impact of Soft Bodies on Jet Engine Fan Blades", is presented in UDRI-TR-76-33 and will be published as an AFML Technical Report. Work on Phase I of this contract was presented in AFML-TR-76-34, entitled "Ordnance Impacts on Jet Engine Fan Blades".

The effort described was conducted in support of Project No. 7351 and Task 735106 for the Metals Behavior Branch of the Metals and Ceramics Division during the period July 1975 to December 1975. The contract monitor was Capt. James S. Wilbeck.

This report was submitted by the authors in August 1976 for publication as a Materials Laboratory Technical Report.

TABLE OF CONTENTS

SECTION		PAGE
I	INTRODUCTION AND SUMMARY	1
	1.1 Problem Area and Background	1
	1.2 Approach	2
	1.3 Summary of Major Results	4
II	THE NUMERICAL SOLUTION	17
	2.1 Impacts on a Rigid Surface	17
	2.2 Impacts on a Deformable Plate	30
	2.3 Impacts on the Leading Edge of Turbine Blades	44
III	COMPARISONS WITH EXPERIMENTS	62
	3.1 Normal Impacts	62
	3.2 Oblique Impacts	65
IV	CONCLUSIONS AND RECOMMENDATIONS	72
APPENDIX A	MATERIAL PROPERTIES	73
APPENDIX B	GALILEAN COORDINATE TRANSFORMATION	78
REFERENCES		80

LIST OF ILLUSTRATIONS

FIGURE		PAGE
1	Conditions for soft body impact analyses	3
2	Velocity fields for water sphere impact at 675 fps onto rigid surface (Case A) at 41 and 157 μ sec	5
3	Radial pressure profiles on rigid surface for water sphere impact at 675 fps (Case A)	6
4	Force history applied to rigid surface by 85 gm water sphere impact at 675 fps (Case A)	7
5	Comparison of force histories in normal and 25° oblique impacts of 85 gm water spheres onto rigid surface at 675 fps (Cases A and B)	10
6	Comparison of force histories on rigid surface and on 0.136-in. stainless steel plate due to 675 fps impact of 85 gm water spheres at normal incidence (Cases A and C)	11
7	Comparison of force histories on rigid surface and on 0.136-in. stainless steel plate due to 675 fps impacts of 85 gm water spheres at 25° obliquity (Cases B and D)	12
8	Normal component of impulse delivered to target versus time for 675 fps impacts of 85 gm water spheres	13
9	Vertical displacement histories of selected points on stainless steel (SS 403) turbine blades following 675 fps impacts of 85 gm water sphere at 25° on leading edge (Case E)	15
10	Vertical displacement histories of selected points on Bo-Al blade following 675 fps impact of 85 gm water sphere at 25° on leading edge (Case F)	16
11	Initial computation grid for 85 gm water sphere impact at 675 fps on rigid surface (Case A)	19
12	Velocity field and pressure field at 7.14 μ sec after 85 gm water sphere impact at 675 fps on rigid surface (Case A)	20
13	Velocity field and pressure field at 14.2 μ sec after 85 gm water sphere impact at 675 fps on rigid surface (Case A)	21
14	Velocity field and pressure field at 41.5 μ sec after 85 gm water sphere impact at 675 fps on rigid surface (Case A)	22

LIST OF ILLUSTRATIONS (CONT'D)

FIGURE		PAGE
15	Velocity field and pressure field at 71.8 μ sec after 85 gm water sphere impact at 675 fps on rigid surface (Case A)	23
16	Velocity field and pressure field at 102 μ sec after 85 gm water sphere impact at 675 fps on rigid surface (Case A)	24
17	Velocity field at 129.5 μ sec after 85 gm water sphere impact at 675 fps on rigid surface (Case A)	25
18	Velocity field at 157.0 μ sec after 85 gm water sphere impact at 675 fps on rigid surface (Case A)	26
19	Normalized force and impulse histories on rigid surface from 85 gm water sphere impact at 675 fps (Case A)	28
20	Geometry of 675 fps impact of water sphere at 25° obliquity on stationary rigid surface (Case B)	29
21	Dynamically equivalent configuration of normal incidence impact of water sphere on moving rigid surface (Case B)	29
22	Pressure contours at 49 μ sec after 85 gm water sphere impact at 675 fps and 25° obliquity on rigid surface (Case B)	31
23	Pressure contours at 100 μ sec after 85 gm water sphere impact at 675 fps and 25° obliquity on rigid surface (Case B)	32
24	Pressure contours at 164 μ sec after 85 gm water sphere impact at 675 fps and 25° obliquity on rigid surface (Case B)	33
25	Pressure contours at 240 μ sec after 85 gm water sphere impact at 675 fps and 25° obliquity on rigid surface (Case B)	34
26	Contact area and pressure distribution on rigid surface for 85 gm, 5.46 cm dia. water sphere impact at 675 fps and 25° obliquity (Case B)	35
27	Normalized force and impulse histories on rigid surface from 85 gm water sphere impact at 675 fps and 25° obliquity (Case B)	36
28	Initial computational grid for 85 gm water sphere impact at 675 fps on 0.136-in. stainless steel plate (Cases C and D)	37

LIST OF ILLUSTRATIONS (CONT'D)

FIGURE		PAGE
29	Velocity field at 65 μ sec after 85 gm water sphere impact at 675 fps on 0.136-in. stainless steel plate (Cases C and D)	38
30	Computational grid at 152 μ sec after 85 gm water sphere impact at 675 fps on 0.136-in. stainless steel plate (Cases C and D)	39
31	Velocity field at 152 μ sec after 85 gm water sphere impact at 675 fps on 0.136-in. stainless steel plate (Cases C and D)	40
32	Stress field at 75 μ sec after 85 gm water sphere impact at 675 fps on 0.136-in. stainless steel plate (Cases C and D)	42
33	Comparisons of normalized force and impulse histories on rigid and deformable targets due to 675 fps impacts of 85 gm water spheres (Cases A and C)	43
34	Velocity field at 68 μ sec after 85 gm water sphere impact at 675 fps and 25° obliquity on 0.136-in. stainless steel plate (Case D)	45
35	Computational grid at 144 μ sec after 85 gm water sphere impact at 675 fps and 25° obliquity on 0.136-in. stainless steel plate (Case D)	46
36	Velocity field at 144 μ sec after 85 gm water sphere impact at 675 fps and 25° obliquity on 0.136-in. stainless steel plate (Case D)	47
37	Stress field at 68 μ sec after 85 gm water sphere impact at 675 fps and 25° obliquity on 0.136-in. stainless steel plate (Case D)	48
38	Comparisons of normalized force and impulse histories on rigid and deformable targets due to 675 fps impacts at 25° obliquity of 85 gm water spheres (Cases B and D)	49
39	Configuration for 85 gm water sphere impact at 25° obliquity on leading edge of J79 Stage I turbine blade at 70% span	50
40	Vertical displacement histories at selected points downstream of impact of 85 gm water sphere at 25° obliquity on leading edge of stainless steel (SS 403) turbine blade (Case E)	53

LIST OF ILLUSTRATIONS (CONT'D)

FIGURE		PAGE
41	Vertical displacement histories at selected points along leading edge of stainless steel (SS 403) turbine blade impacted on leading edge by 85 gm water sphere at 25° obliquity (Case E)	54
42	Vertical displacement histories at selected points along trailing edge of stainless steel (SS 403) turbine blade impacted on leading edge by 85 gm water sphere at 25° obliquity (Case E)	55
43	Vertical displacement histories at selected points on surface of stainless steel (SS 403) turbine blade impacted on leading edge by 85 gm water sphere at 25° obliquity (Case E)	56
44	Vertical displacement histories at selected points downstream of impact of 85 gm water sphere at 25° obliquity on leading edge of Bo-Al turbine blade (Case F)	58
45	Vertical displacement histories at selected points along leading edge of Bo-Al turbine blade impacted on leading edge by 85 gm water sphere at 25° obliquity (Case F)	59
46	Vertical displacement histories at selected points along trailing edge of Bo-Al turbine blade impacted on leading edge by 85 gm water sphere at 25° obliquity (Case F)	60
47	Vertical displacement histories at selected points on surface of Bo-Al turbine blade impacted on leading edge by 85 gm water sphere at 25° obliquity (Case F)	61
48	Summary of impact conditions for calculations and experiments	63
49	Comparison of calculated and measured pressure histories at impact point: Normal-incidence impacts on rigid surface	64
50	Comparison of calculated and measured pressure histories in target surface 12.7 cm (1/2-in.) from impact point: Normal-incidence impacts on rigid surface	66
51	Comparison of calculated and measured pressure histories in target surface 25.4 cm (1-in.) from impact point: Normal-incidence impacts on rigid surface	67
52	UDRI pressure transducer data from 25° oblique impacts of cylinders	68
53	Comparison of calculated and measured pressure histories in target surface: 25° oblique impacts on rigid surface	70

SECTION I

INTRODUCTION AND SUMMARY

1.1 PROBLEM AREA AND BACKGROUND

Foreign objects (for example rocks, birds, tools, etc.) ingested into turbine engines can cause substantial or catastrophic damage to the blades. This problem is of particular importance with respect to the development and utilization of new, light-weight blade materials which may be quite vulnerable to damage by such impacts.

The response of a turbine blade to a foreign object impact can be separated into local (or short time) and global (or long time) response. Local response involves the force and impulse loading and the damage processes in the immediate vicinity of the impact. Global response involves the longer-term response of the entire blade, including the attachment to the hub.

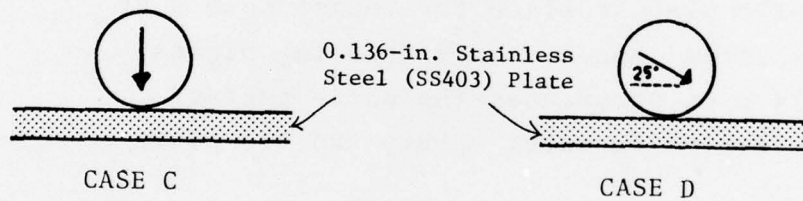
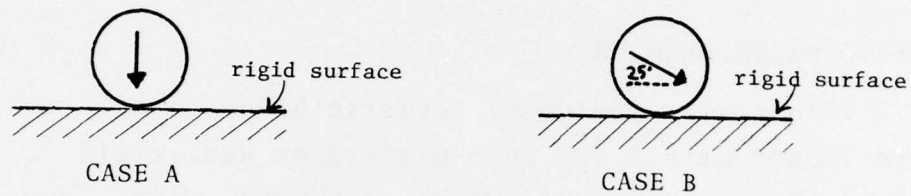
The objective of the exploratory program reported herein has been to investigate the local impact response of blades to soft body impacts (e.g. birds) using numerical and analytical techniques. Once the local impact force and impulse are characterized, these can be used as loading boundary conditions for separate analyses of the global response of blades and attachment structures. (In another part of this program, bullet impacts on titanium, boron aluminum, and graphite epoxy plates are being analyzed in both the normal and oblique impact configurations. That work will be described in a separate report.)

1.2 APPROACH

Computational codes were used as the primary tools to investigate local soft body impact phenomenology. The codes predict the time-resolved pressure and velocity fields in the impacting object. They also predict the spatial and temporal details of the impact forces acting on the target, as well as the resulting target response. Figure 1 shows the cases treated; these were chosen to qualitatively and quantitatively investigate the *phenomenology* of soft body impacts on the face as well as the edge of turbine blades. In all cases the impacting object was a 3-oz sphere of water ($r = 1.07$ in. or 2.73 cm) with a velocity of 675 ft/sec. In this study, water was used to simulate the impact properties of birds.

Cases A and B treat a normal and a shallow angle impact on a rigid surface, while Cases C and D treat the corresponding impacts on a 0.136-in. thick stainless steel plate. Comparisons of these cases show the effects of plate deformation on the impact loading. Cases E and F involve a shallow angle impact on the leading edge of a representative turbine blade.

Cases A, B, C, and D were analyzed using the two-dimensional WAVE-L finite difference code. WAVE-L is a HEMP-type¹ Lagrangian code. The initial conditions for the 25° oblique impact cases (Cases B and D) were treated in a moving frame of reference using a Galilean transformation; the 3-D oblique impact configuration is thereby simplified to an axisymmetric (2-D) geometry. This transformation and the rigid and SS403 plate impact cases (A, B, C, and D) are described in Sections 2.1 and 2.2. Cases E and F were analyzed using the three-dimensional NONSAP finite element code²; the results are described in Section 2.3.

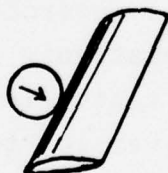


For all cases:

Impact velocity, $V_o = 675 \text{ fps (205.7 m/sec)}$

Impacting body is 3 oz water sphere

$m = 85 \text{ gms, } d_o = 5.46 \text{ cm}$



CASE E (Stainless steel SS403 blade)

CASE F (Boron-Aluminum blade)

Figure 1. Conditions for Soft Body Impact Analyses

In parallel to this computational/analytical effort, UDRI has performed an experimental investigation of normal and oblique soft body impacts on rigid and thin plates³. The computational and experimental results are compared in Section 3.

1.3 SUMMARY OF MAJOR RESULTS

Figure 2 illustrates the characteristic behavior of a water sphere impact at 675 fps onto a rigid or semi-rigid surface. Radial flow of material quickly develops, with radial velocities which are over twice the impact velocity occurring near the plate surface. Figure 3 shows pressure-radius profiles on the plate surface for impact Case A at a sequence of times after impact. Note that the highest pressures at 7 and 14 μ sec occur near the *outer* contact radius between the flattening water sphere and the plate surface.

The force on the plate is the integrated area under the pressure-radius profile. Figure 4 shows the force history on the plate for Case A. The sharp initial rise corresponds to the period when the impact shock is interacting with the droplet flow. It is followed by a relatively long period during which the force is nearly constant. This is the period when most of the axial flow diversion to radial flow takes place. Finally, the force begins to decay as the rear of the drop approaches the target. (When the axial-radial turning is complete, the force will drop to zero.)

Figure 4 uses both dimensional and non-dimensional (normalized) coordinates for force and time. The time normalization factor, τ , is the time required for the sphere to move its own diameter in the direction perpendicular to the

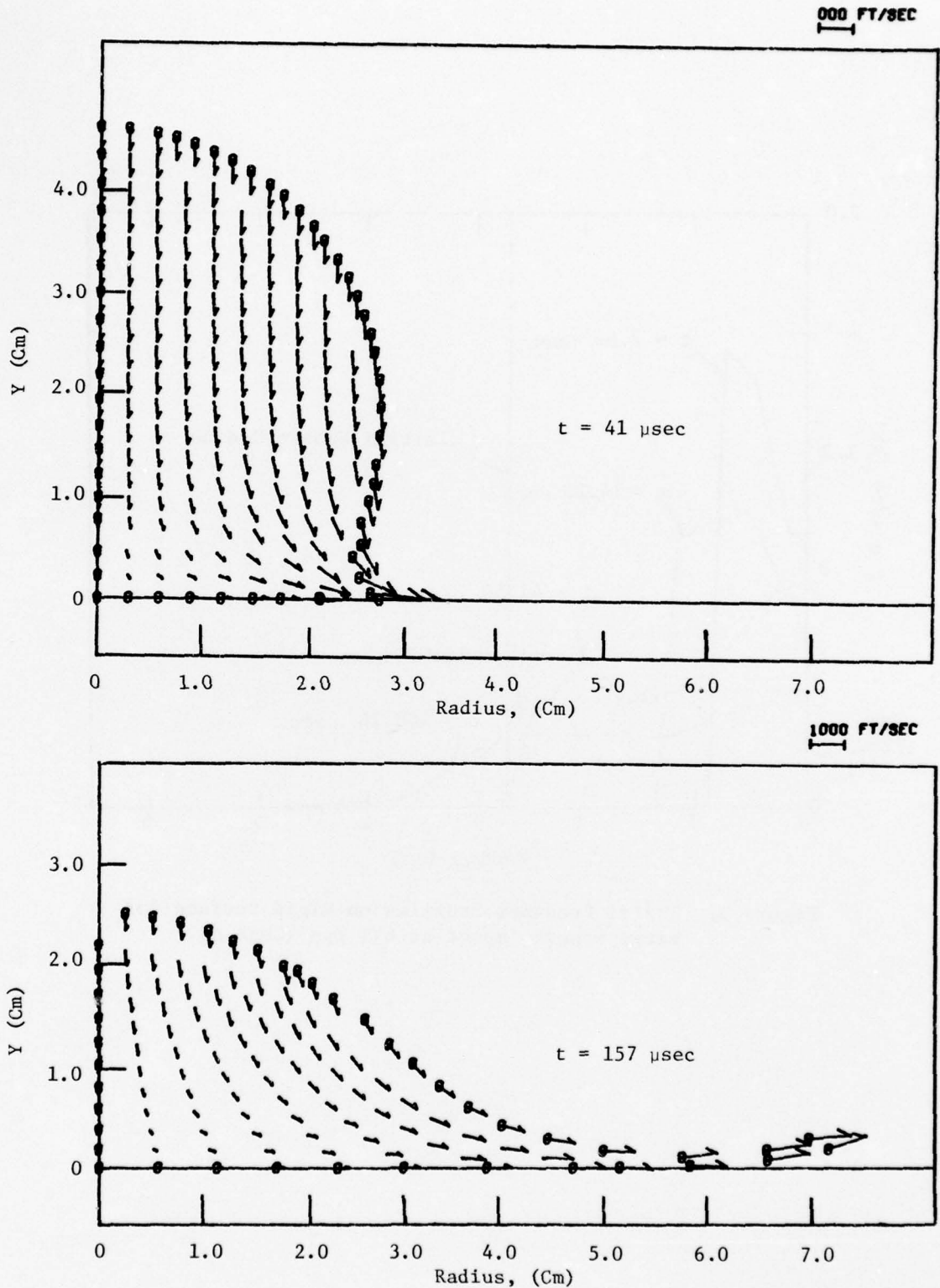


Figure 2. Velocity Field for a Water Sphere Impact at 675 fps onto a Rigid Surface (Case A) at 41 and 157 μ sec.

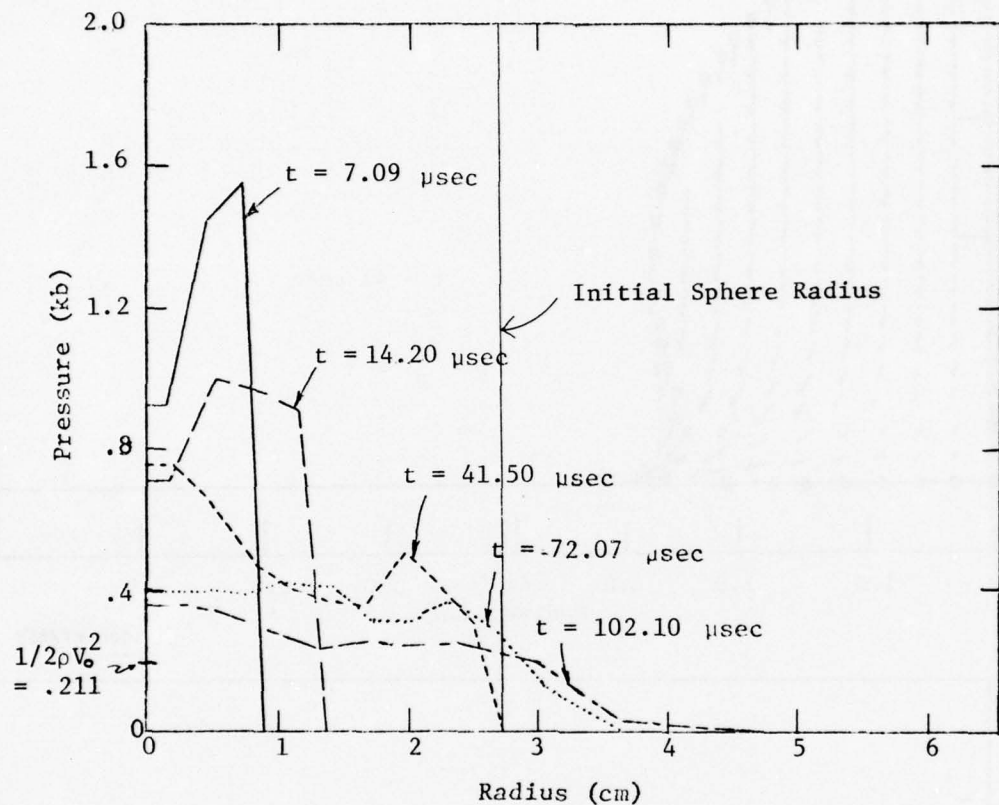


Figure 3. Radial Pressure Profiles on Rigid Surface for Water Sphere Impact at 675 fps (Case A).

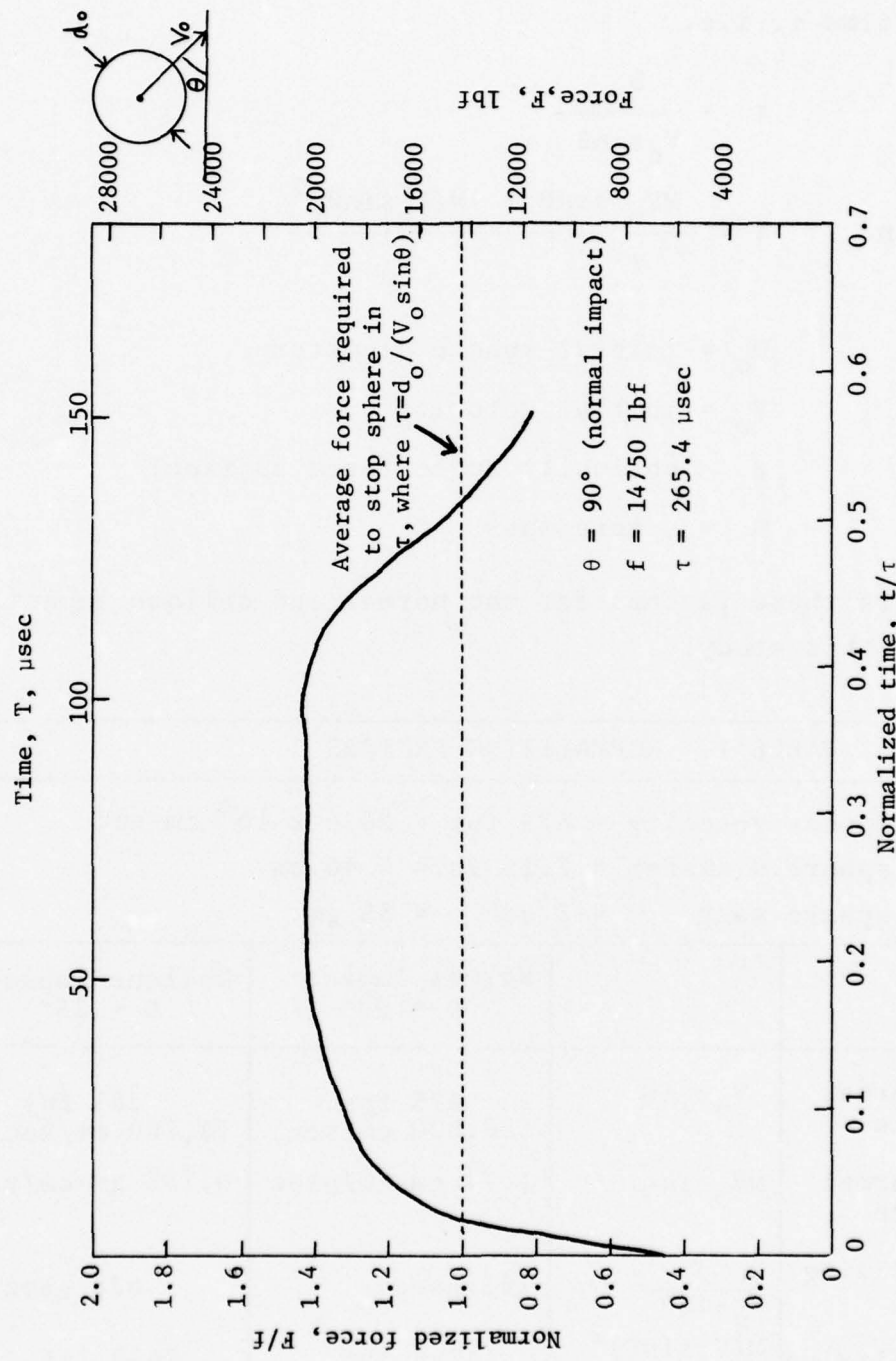


Figure 4. Force History Applied to Rigid Surface by 85 gm Water Sphere Impact at 675 fps (Case A)

surface; the force normalization factor, f , is the average force required to stop the momentum perpendicular to the surface in time τ , i.e.

$$\tau = \frac{D_o}{V_o \sin \theta}$$

$$\text{and } f = \frac{MV_o \sin \theta}{\tau} = \frac{M(V_o \sin \theta)^2}{D_o}$$

where

D_o = initial sphere diameter

V_o = initial velocity

θ = obliquity angle (from surface)

M = sphere mass

Table 1 lists these factors for the normal and oblique impacts analyzed in this study.

TABLE 1. NORMALIZING FACTORS

		Normal Impact $\theta = 90^\circ$	Oblique Impact $\theta = 25^\circ$
V_o	= impact velocity = 675 fps = 20.6×10^4 cm/sec		
D_o	= sphere diameter = 2.15 in. = 5.46 cm		
M	= sphere mass = 3 oz = 85 gm		
Velocity normal to surface	$V_o \sin \theta$	675 fps (20,600 cm/sec)	285 fps (8,700 cm/sec)
Momentum normal to surface	$MV_o \sin \theta$	1.74 gm-cm/ μ sec	0.735 gm-cm/ μ sec
Time normalizing factor, τ	$\frac{D_o}{V_o \sin \theta}$	265 μ sec	628 μ sec
Force normalizing factor, f	$\frac{M(V_o \sin \theta)^2}{D_o}$	14750 lbf (6.56×10^9 dynes)	2630 lbf (1.17×10^9 dynes)

Use of non-dimensional (normalized) time and force parameters allows the results of the numerical solutions to be scaled to any size impacting sphere, and perhaps to other impact velocities and obliquities. Figure 5 compares the non-dimensional force histories in the normal and 25° oblique impacts onto a rigid surface (Cases A and C). The relatively small difference between the two cases confirms that the normalizing factors are reasonably valid, at least for those impacts where the velocity component perpendicular to the surface is between 285 and 675 fps.

The force histories applied to a rigid surface and to a deformable surface (i.e. a 0.136-in. stainless steel plate) are compared in Figure 6 (normal impacts) and Figure 7 (25° oblique impacts). The respective rigid and deformable curves have the same general shape in both figures; however, the force levels are lower on the deformable plates. This is because the plate displaces in the direction of the sphere's velocity, thereby reducing the effective impact velocity and the subsequent pressure and force.

The momentum, or impulse, imparted to the surface is the integrated area under the normal force-time profiles. (Friction between the water sphere and the impacted surface is assumed to be negligible, so impulse is imparted only perpendicular to the surface.) Figure 8 shows the time-histories of the impulses delivered to the targets for Cases A, B, C, and D. (Impulse is normalized by dividing by the initial perpendicular component of momentum of the sphere, $MV_0 \sin\theta$.) All the time histories are fairly similar on this normalized plot, with the deformable plate impacts (Cases C and D) falling somewhat below the rigid target impacts (A and B).

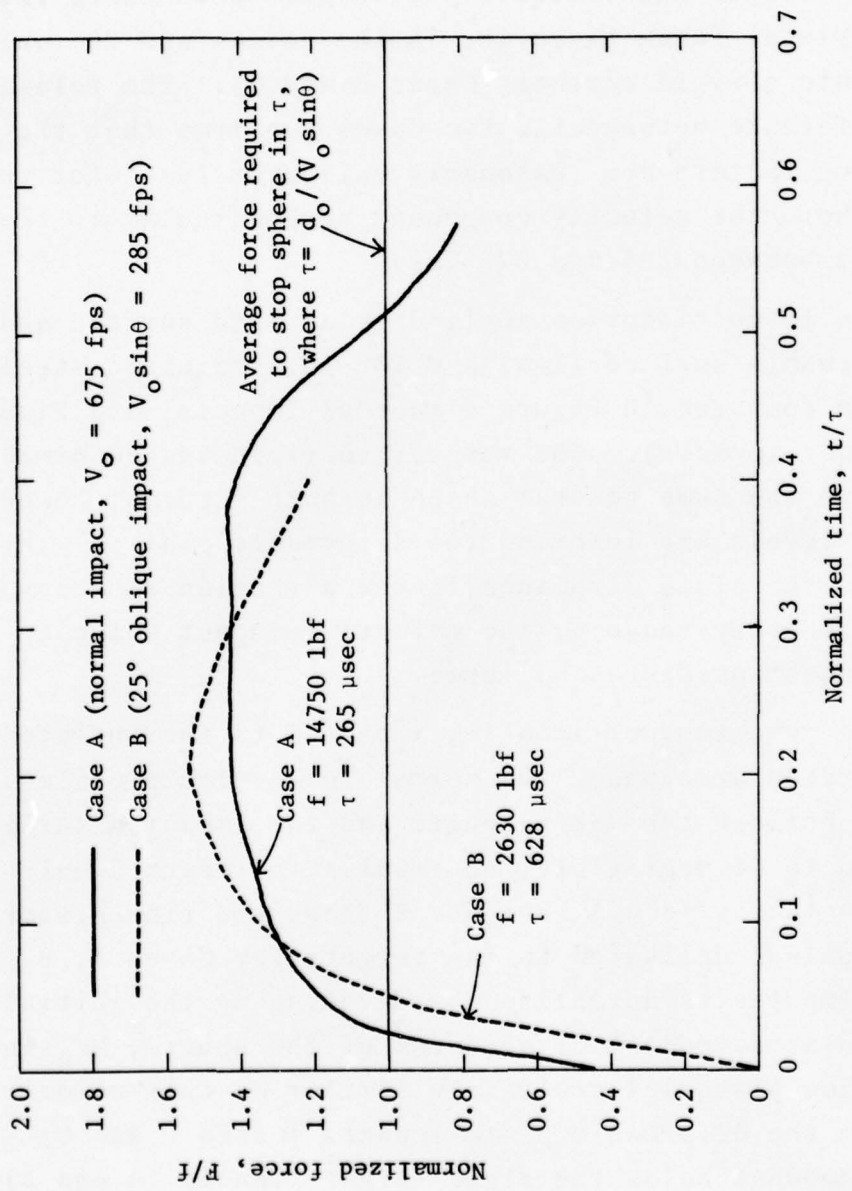


Figure 5. Comparison of Force Histories in Normal and 25° Oblique Impacts of 85 gm Water Spheres Onto Rigid Surface at 675 fps (Cases A and B)

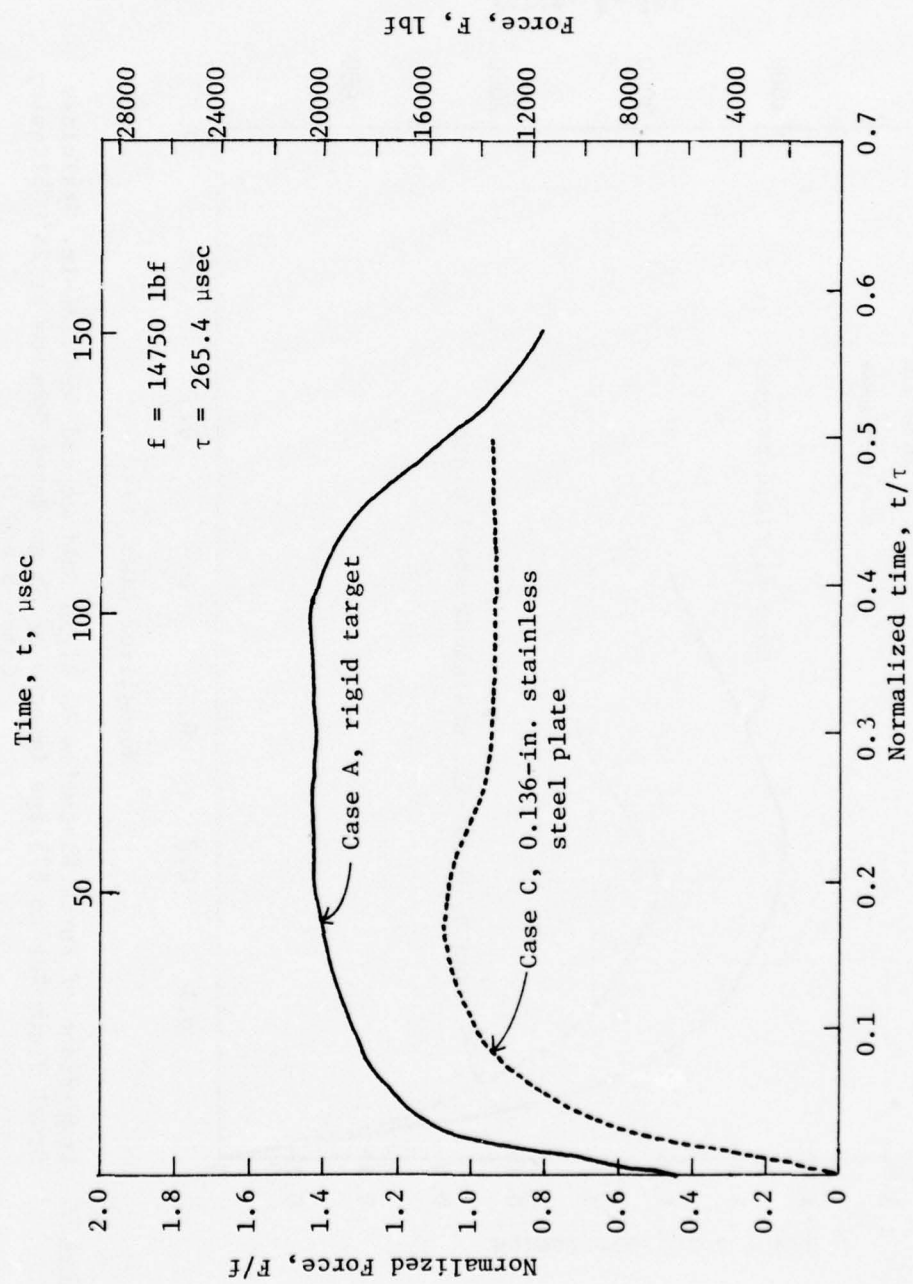


Figure 6. Comparison of Force Histories on Rigid Surface and on 0.136-in. Stainless Steel Plate Due to 675 fps Impacts of 85 gm Water Spheres at Normal Incidence (Cases A and C)

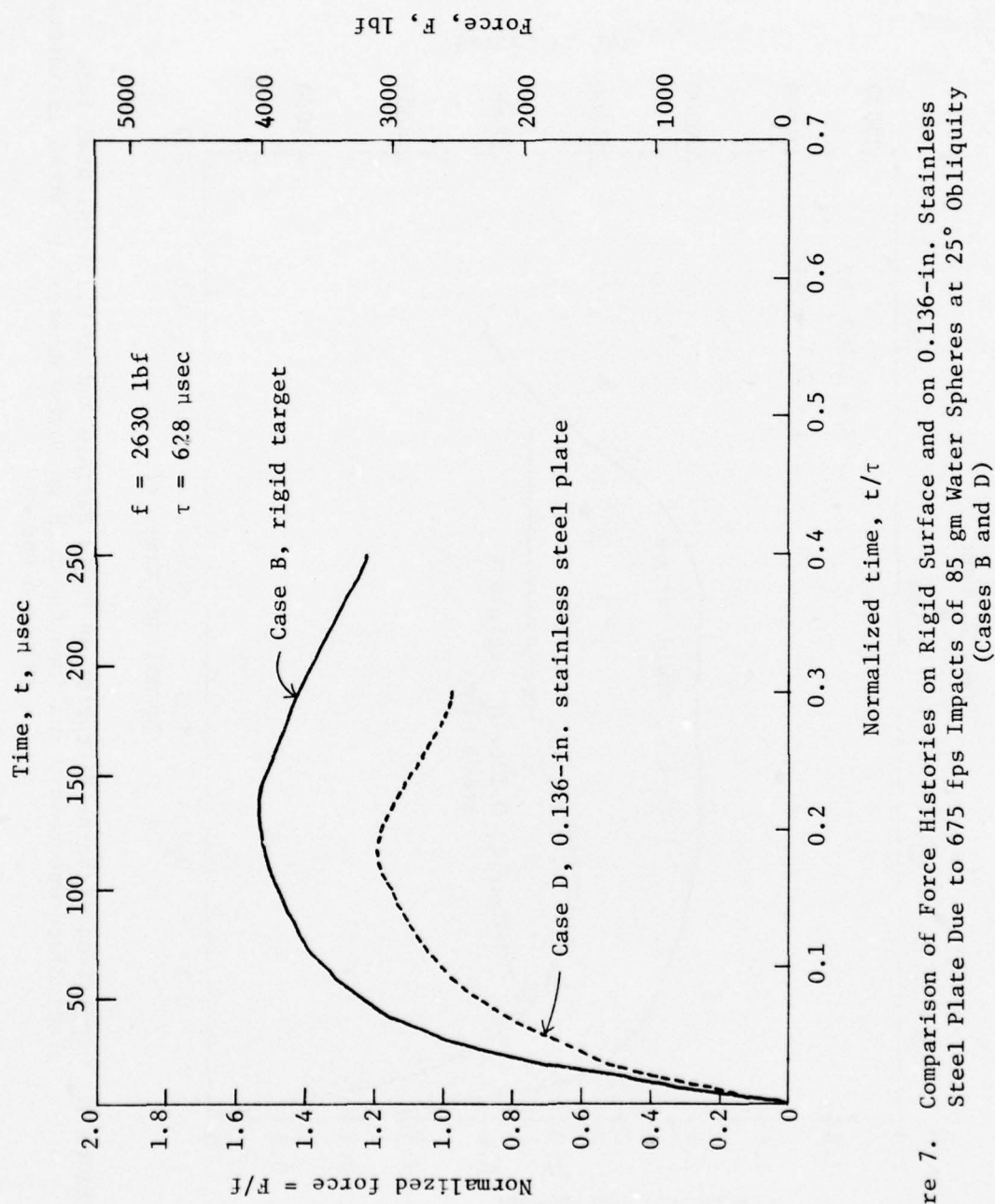


Figure 7. Comparison of Force Histories on Rigid Surface and on 0.136-in. Stainless Steel Plate Due to 675 fps Impacts of 85 gm Water Spheres at 25° Obliquity (Cases B and D)

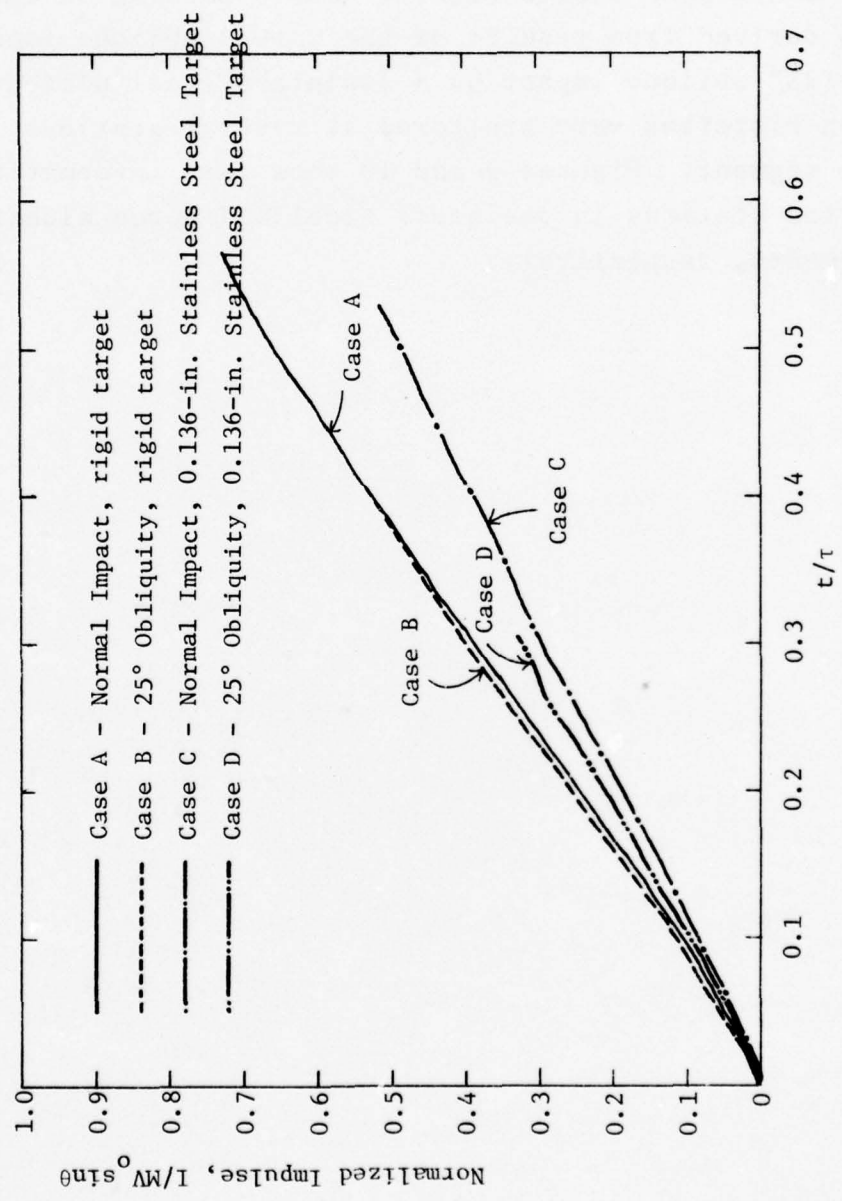


Figure 8. Perpendicular Component of Normalized Impulse Delivered to Target versus Time for 675 fps Impacts of 85 gm Water Sphere

For the cases where impacts on the leading edge of blades were considered (E and F), a blade segment corresponding to the profile of the J79 Stage 1 blade at 70% span was modeled using the 3-d NONSAP finite element code. Loading on the blade was derived from results of the Case B oblique impact solution (25° oblique impact on a stainless steel plate). Deflection histories were monitored at several stations in the blade segment. Figures 9 and 10 show this information for selected stations in stainless steel and boron aluminum blade segments, respectively.

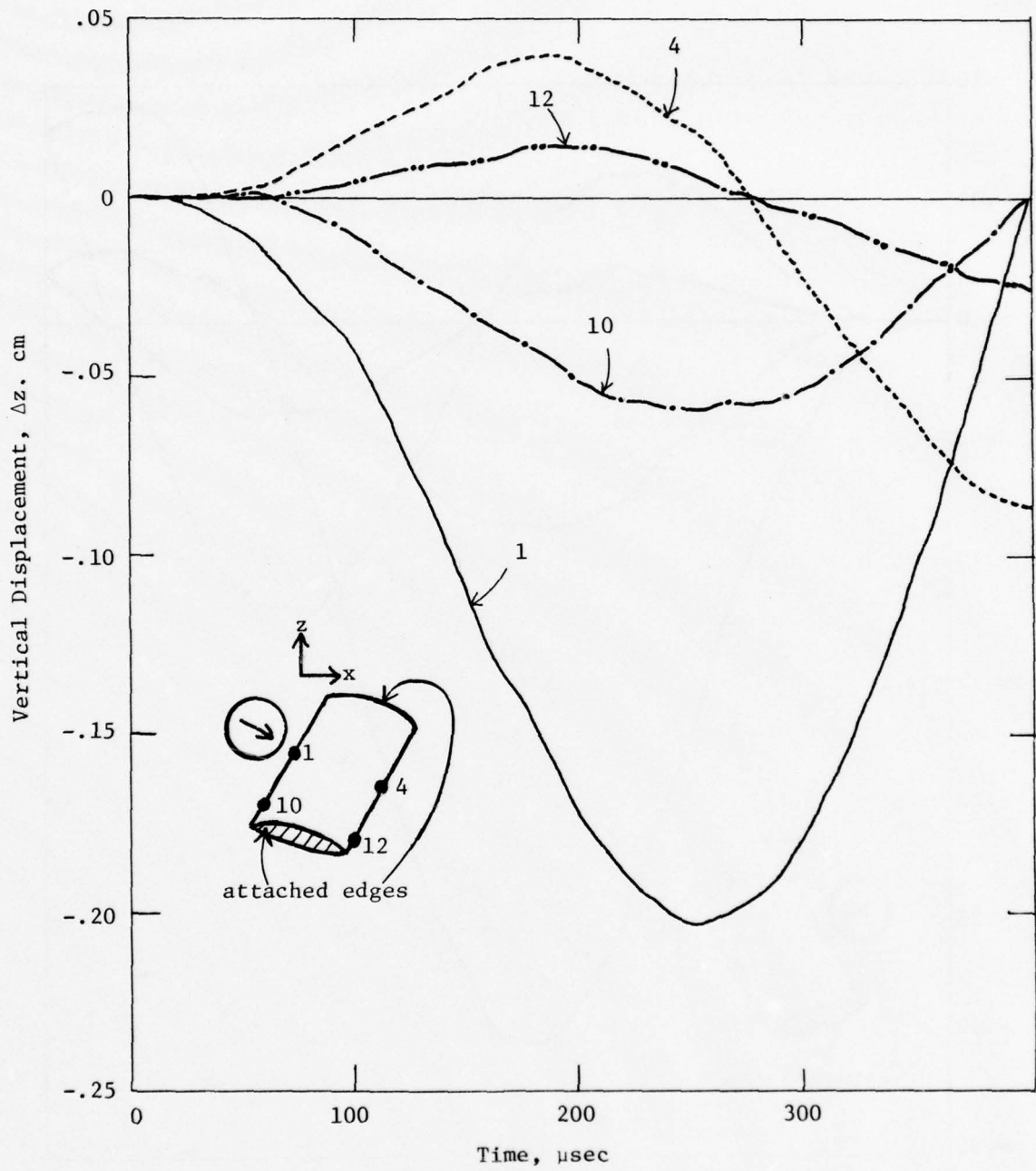


Figure 9. Vertical Displacement Histories of Selected Points on Stainless Steel (SS403) Turbine Blade Following 675 fps Impact of 85 gm Water Sphere at 25° on Leading Edge (Case E)

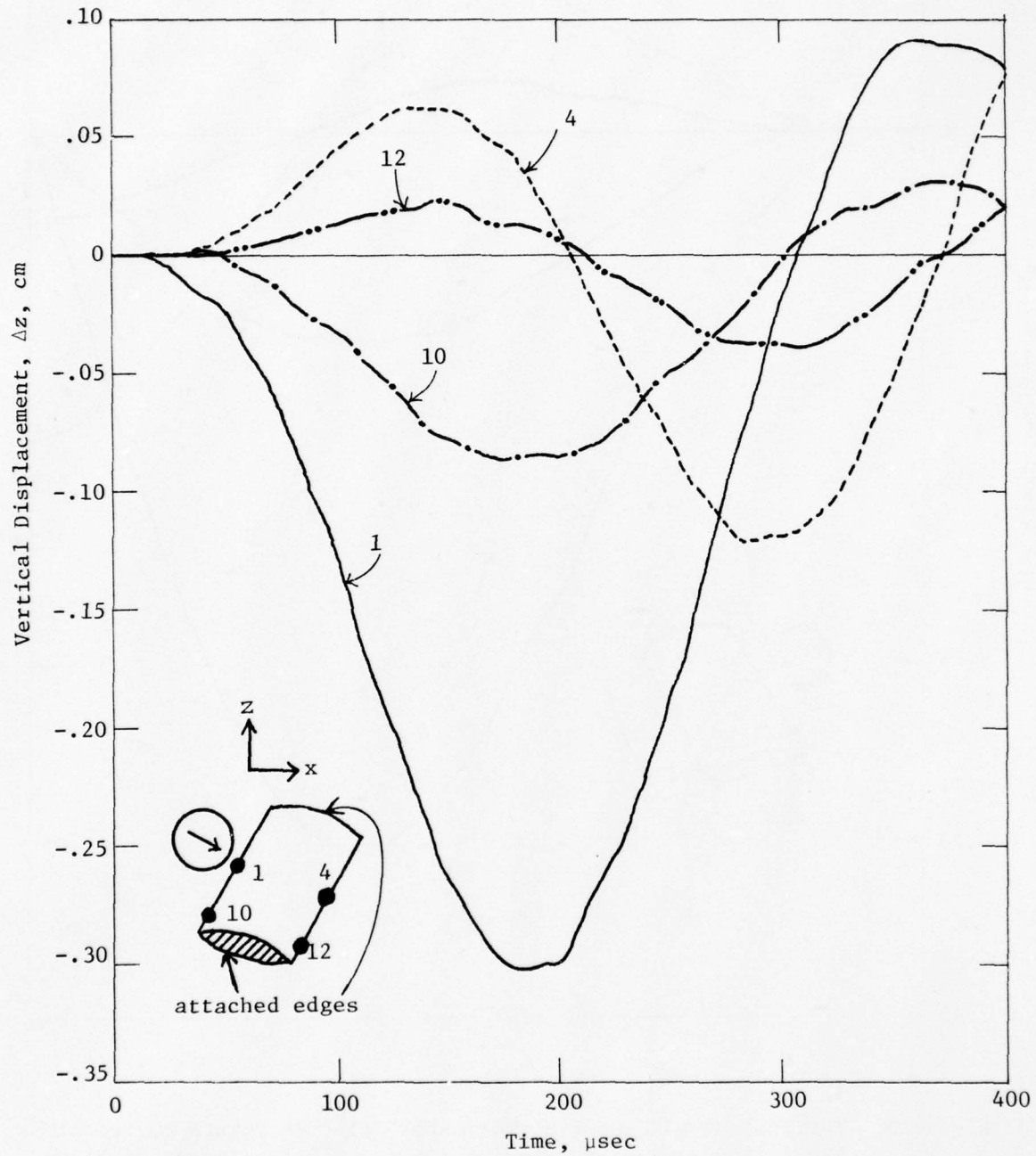


Figure 10. Vertical Displacement Histories of Selected Points on Bo-Al Turbine Blade Following 675 fps Impact of 85 gm Water Sphere at 25° on Leading Edge (Case F)

SECTION II

THE NUMERICAL SOLUTIONS

In this section, the numerical solutions defined by Figure 1 in Section 1.2 are described and illustrated by velocity fields, computational grids, pressure contours, and curves showing the spatial and temporal distribution of forces on the target. The properties used to model the various materials in these solutions are described in Appendix A.

2.1 IMPACTS ON A RIGID SURFACE

The physical phenomena taking place during the impact of a spherical water drop on a rigid target have been examined both theoretically and experimentally (for example, References 4 and 5). Although there is not a sharp delineation in the physical processes, the impact phenomena have generally been considered to occur in two phases. During Phase I of the impact event, the *compressibility* of the liquid drop is the dominant characteristic. High pressures occur near the impact point and there is little radial flow. Phase II is dominated by the *radial flow* diversion of the liquid along the rigid boundary at velocities which can be over twice the initial impact velocity.

For normal incidence impacts, the nominal peak pressure which occurs during Phase I is roughly the "water hammer pressure:", i.e.,

$$P_M = \rho_0 c V_n$$

where ρ_0 = density of the liquid drop

c = sound speed in the drop

V_n = normal component of the impact velocity

For the normal incidence, 675 fps impacts in the current study, $P_M = 2.8$ kb.

Rarefaction waves from the droplet free surface provide relief from the water hammer pressure. Because the impact velocity in the current study is low compared to the speed of sound in water (4500 fps), the pressures during Phase I drop very rapidly (i.e. within a few μ sec) from the water hammer level.

2.1.1 Case A - Normal Impact on Rigid Plane

Case A treats the normal impact of a water sphere on a rigid surface at 675 fps. The initial grid configuration for this numerical solution is shown in Figure 11. There are 20 computational cells across the sphere radius.

Figures 12 and 13 are velocity and pressure field plots at 7 and 14 μ sec. Figure 13 is just beginning to show significant radial deformation. While still relatively high (1-1.5 kb), pressures at 7 and 14 μ sec have already dropped well below the water hammer pressure. It is interesting to note that the peak pressures ($P_{max} > 1$ kb) within the drop at this point do not occur at the rigid contact surface, but rather in a region slightly above that surface.

Figures 14 through 18 show the development of high radial velocity flow characteristics (i.e. Phase II) along the rigid surface. The peak radial velocity is about twice the impact velocity. The location of the maximum pressure in the drop moves down to the rigid plane. During this period, the dynamics are essentially governed by incompressible flow.

Figure 3 (in Section 1) shows pressure profiles along the rigid surface at several times. The water hammer pressure (about 2.8 kb) lasts for only about 1 μ sec for the sphere size and impact velocity involved in Case A, and is thus not seen in Figure 3. By 14 μ sec, the highest pressure

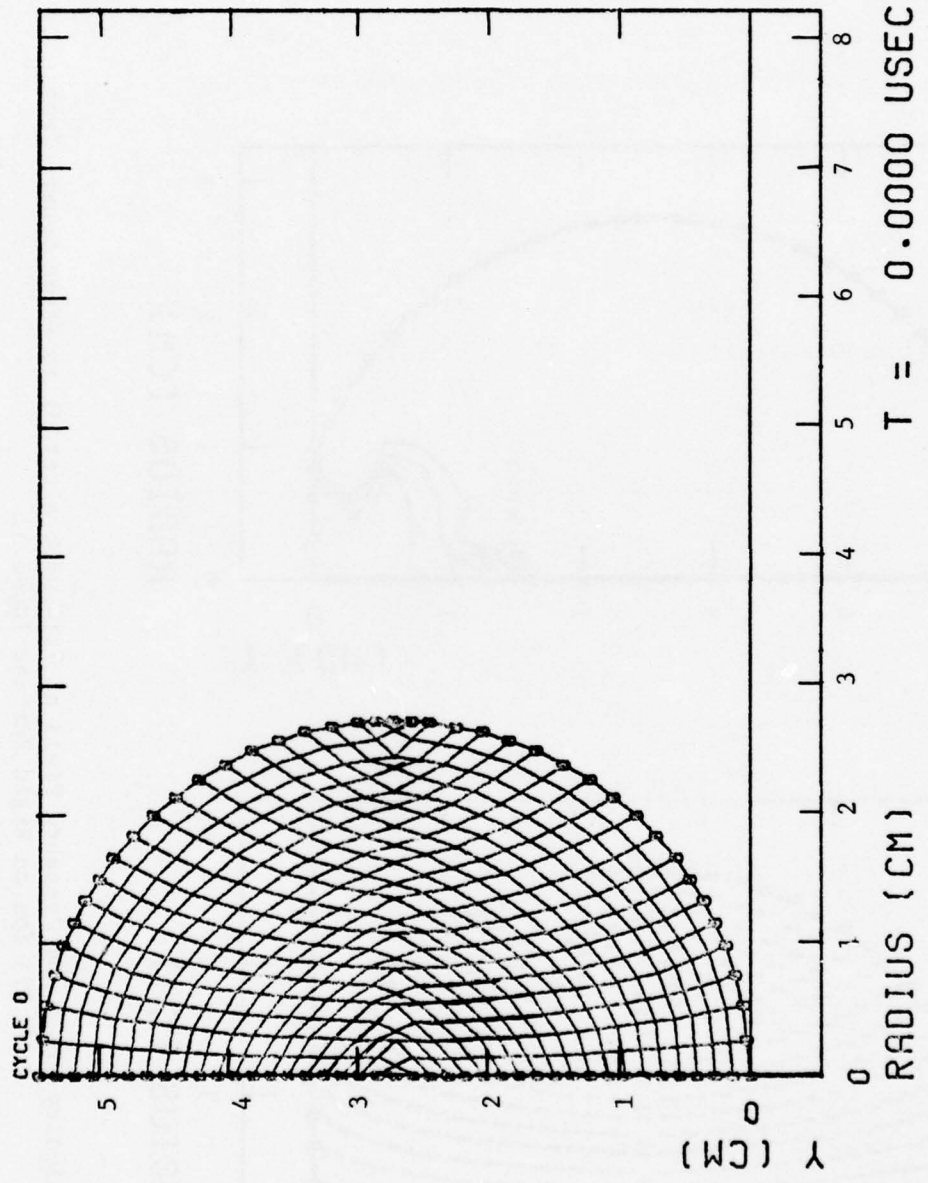


Figure 11. Initial Computational Grid for 85 gm Water Sphere Impact at 675 fps
on Rigid Surface (Case A)

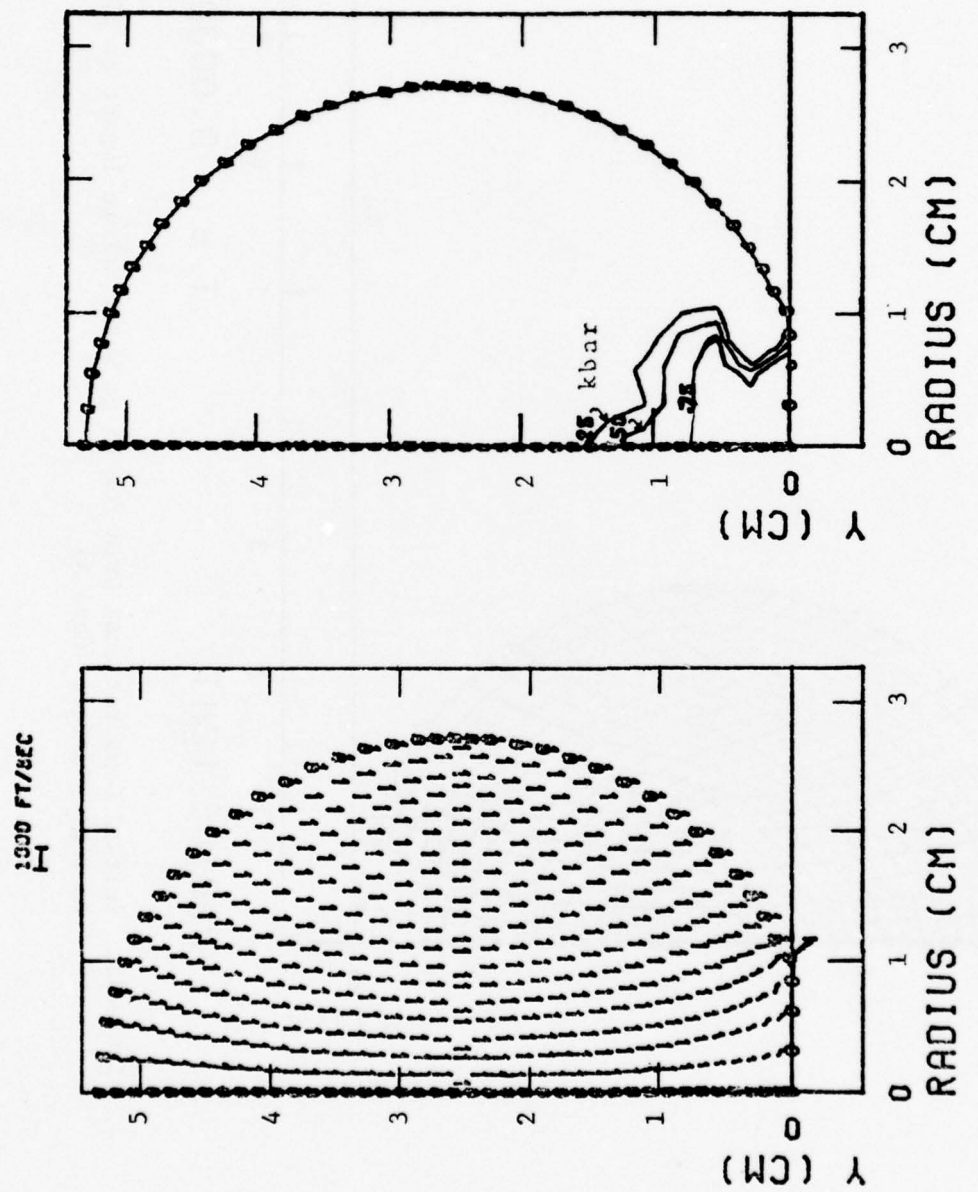


Figure 12. Velocity Field and Pressure Field at 7.14 μ sec After 85 gm Water Sphere Impact
at 675 fps on Rigid Surface (Case A)

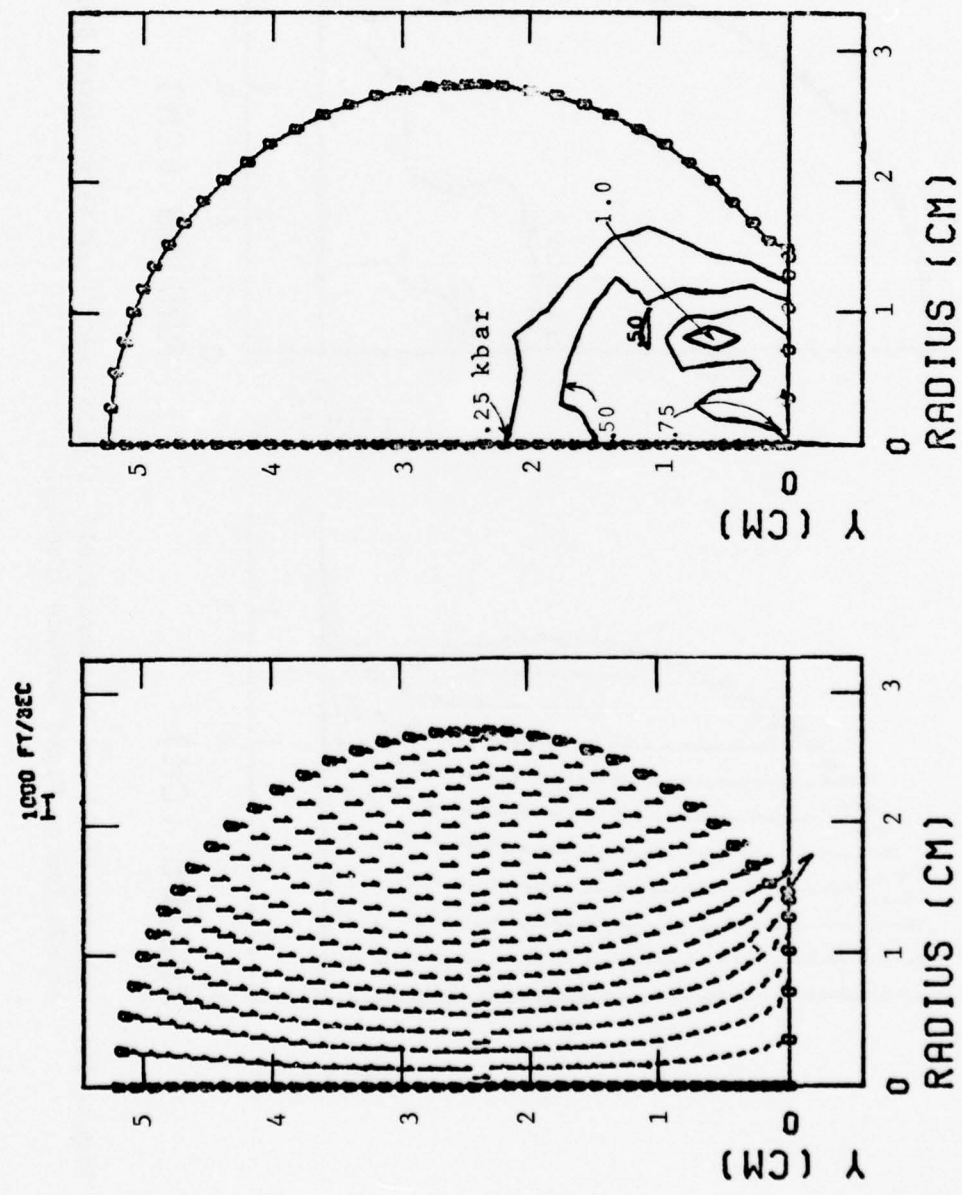


Figure 13. Velocity Field and Pressure Field at $14.2 \mu\text{sec}$ After 85 gm Water Sphere Impact at 675 fps on a Rigid Surface (Case A)

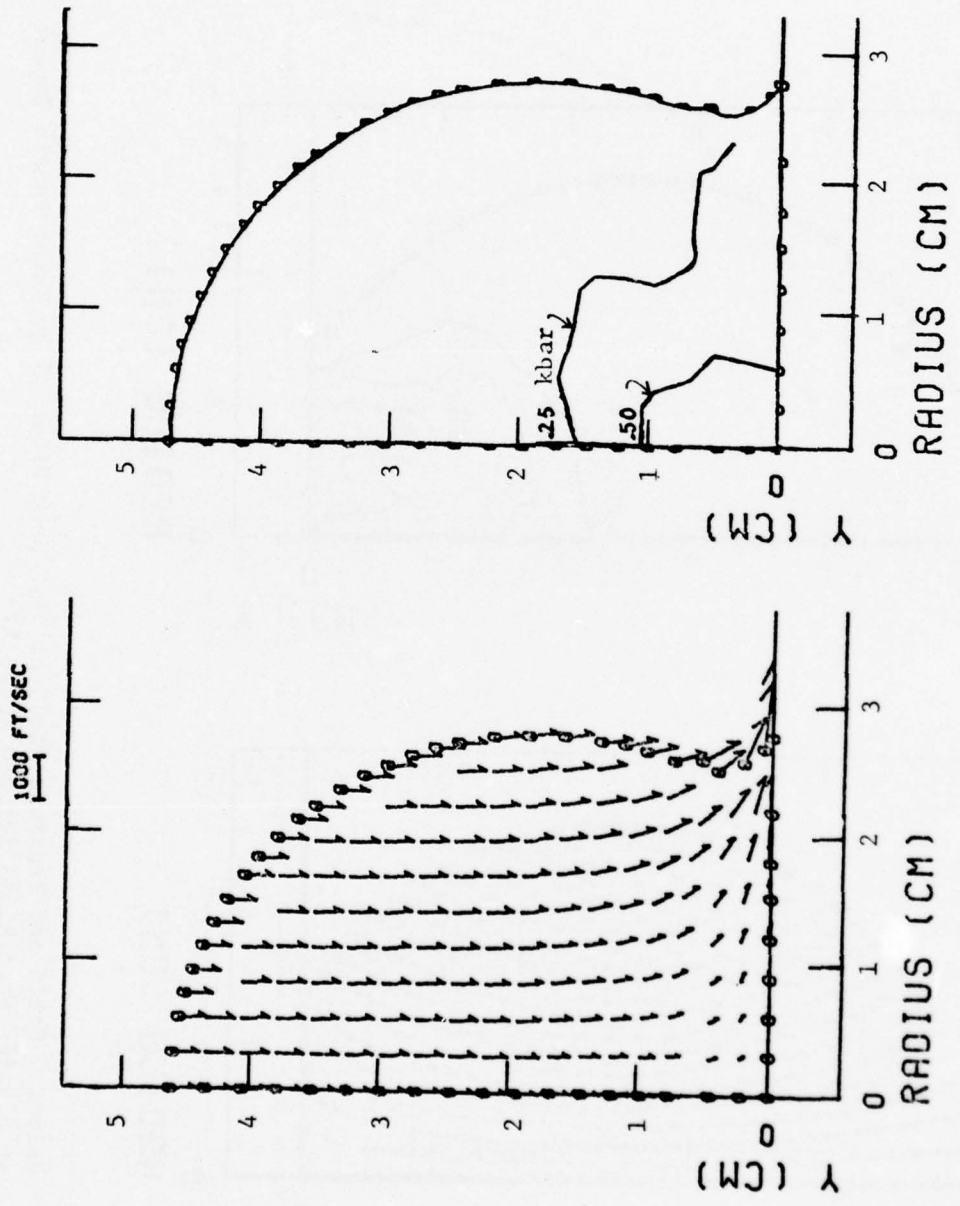


Figure 14. Velocity Field and Pressure Field at 41.5 μ sec After 85 gm Water Sphere Impact
at 75 fps on Rigid Surface (Case A)

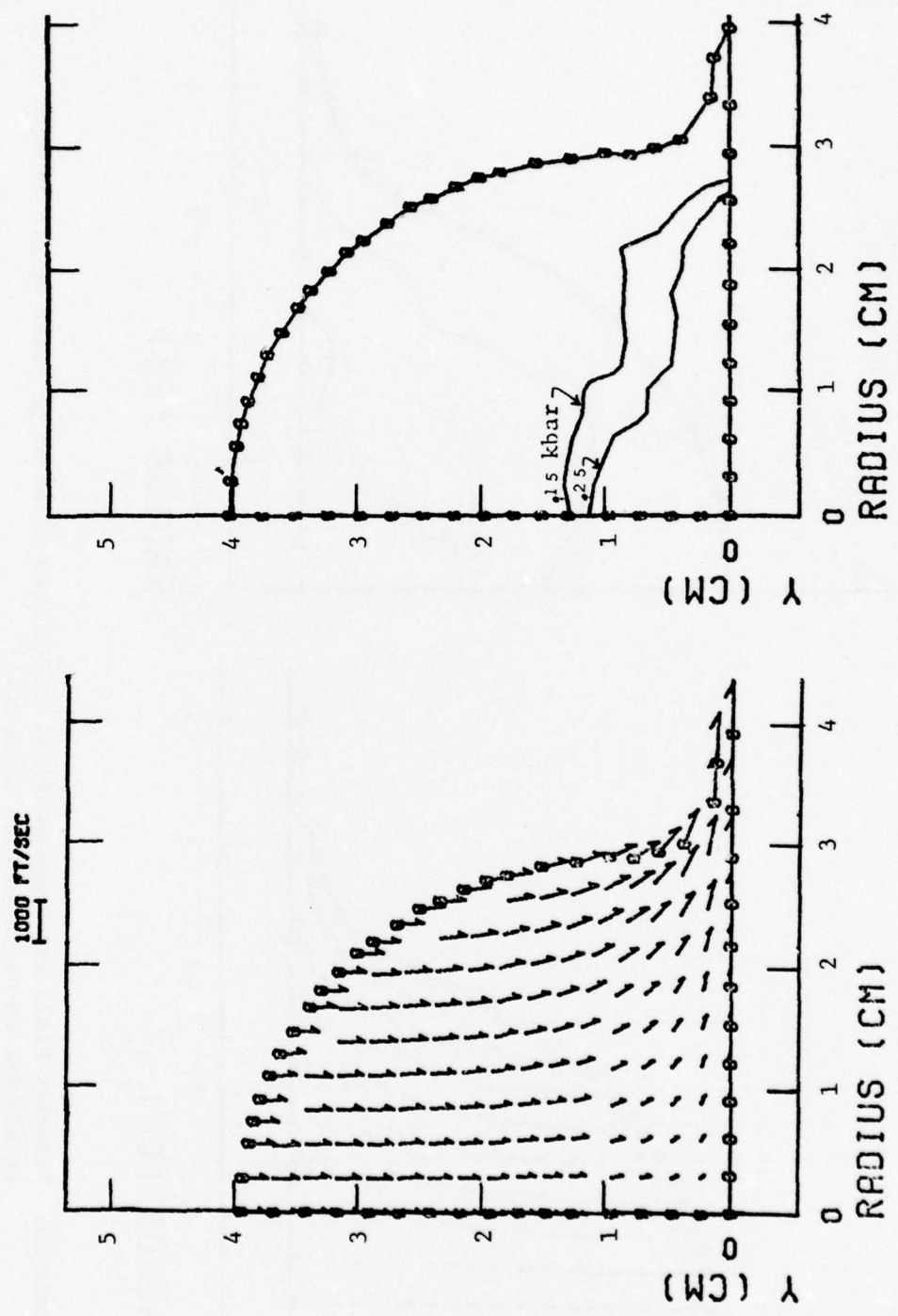


Figure 15. Velocity Field and Pressure Field at 71.8 μ sec After 85 gm Water Sphere Impact
at 675 fps on Rigid Surface (Case A)

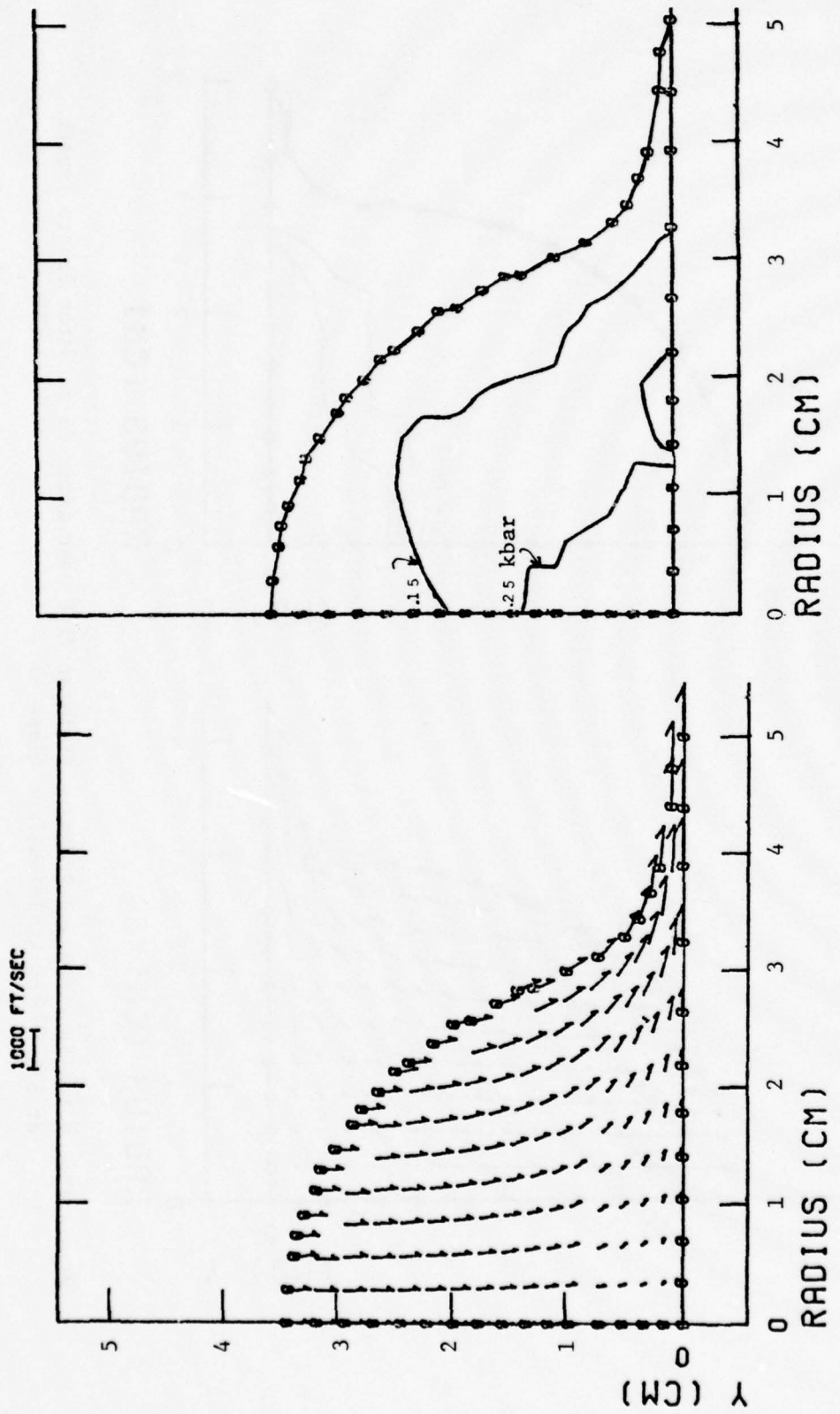


Figure 16. Velocity Field and Pressure Field at 102 μ sec After 85 gm Water Sphere Impact
at 675 fps on Rigid Surface (Case A)

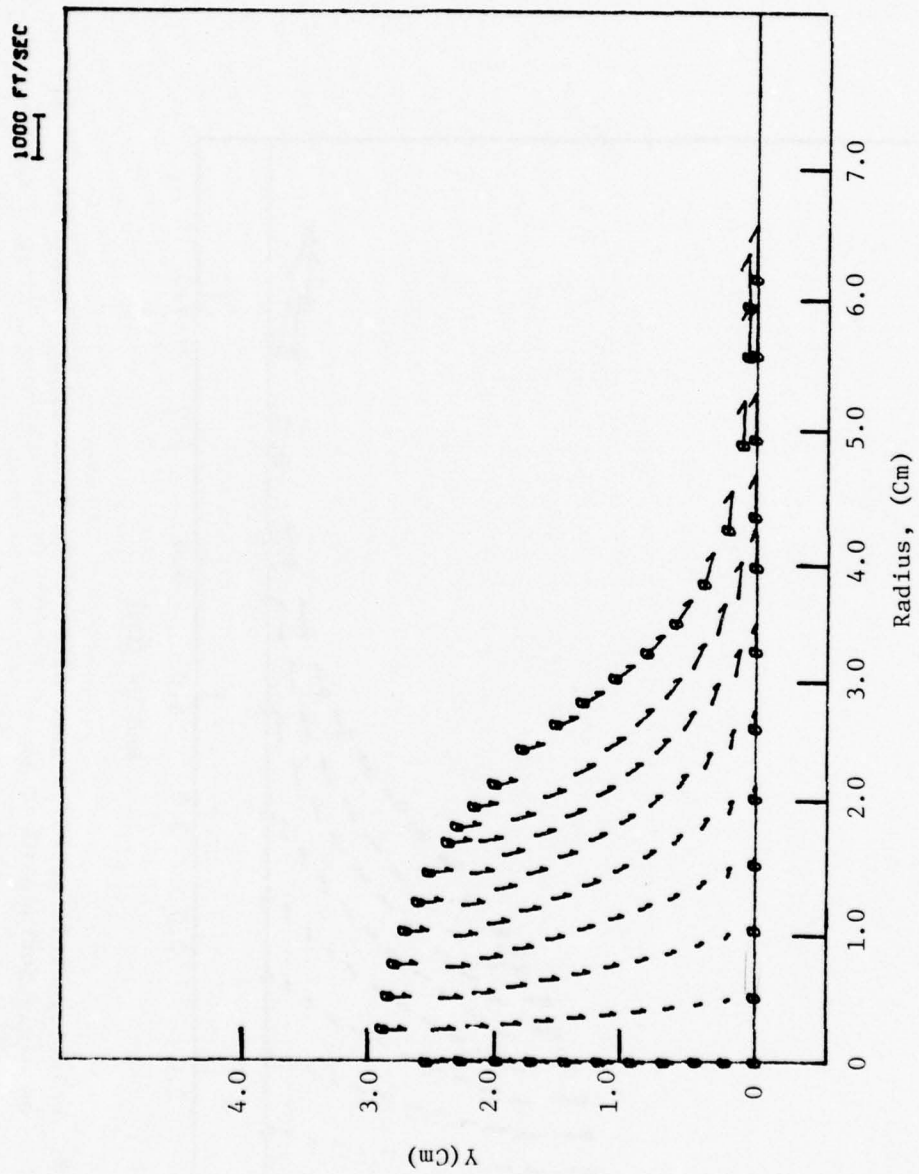


Figure 17. Velocity Field at 129.5 μ sec After 85 gm Water Sphere Impact
at 675 fps on Rigid Surface (Case A)

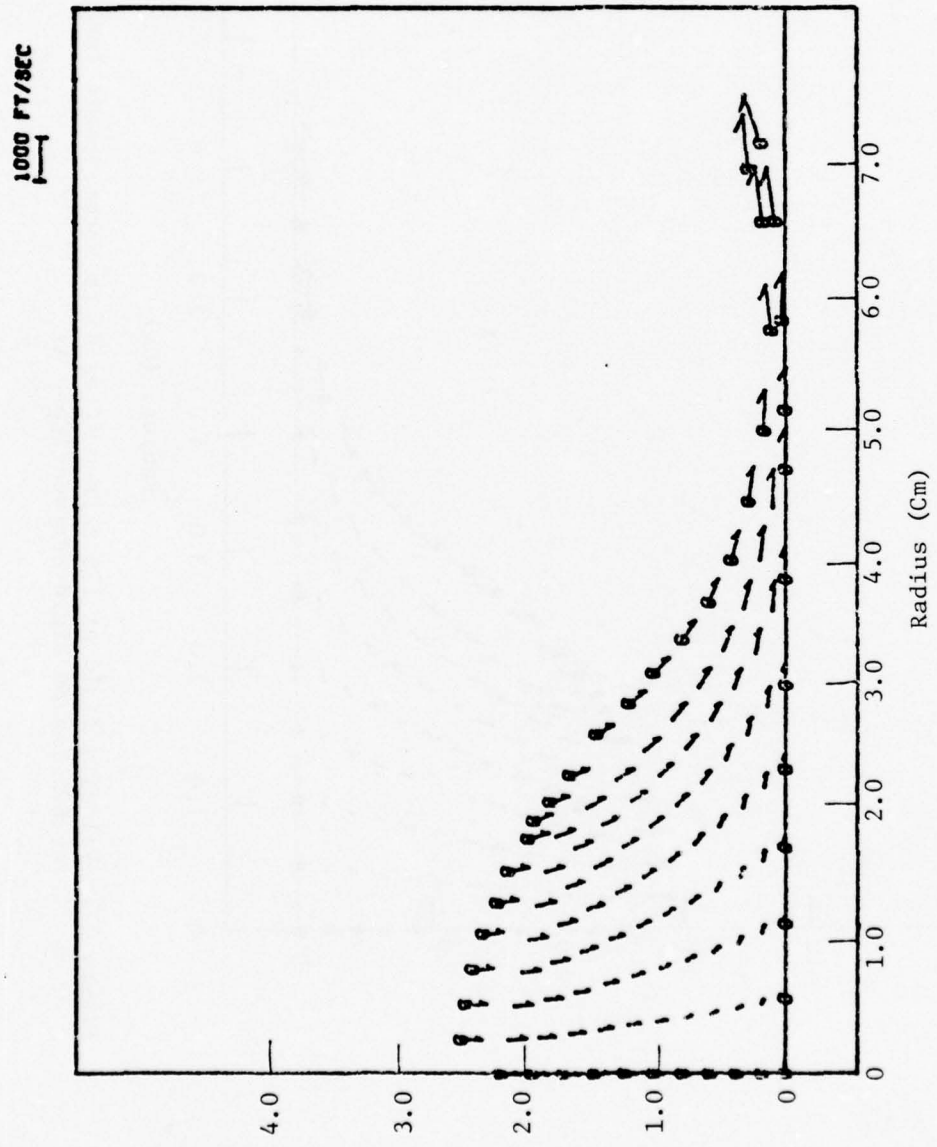


Figure 18. Velocity Field at 157.0 μ sec After 85 gm Water Sphere Impact at 675 fps
on Rigid Surface (Case A)

is about 1 kb. At both 7 and 14 μ sec, the peak pressure occurs near the periphery of the contact surface between the droplet and the rigid surface. By 41 μ sec, the highest pressures are on the axis, but a local maximum occurs closer to the periphery of the contact surface. By 72 μ sec (which corresponds to the flow field in Figure 15), the pressure distribution on the rigid plane has reached a nearly uniform distribution out to about 2.5-cm radius. Beyond 2.5-cm, pressure decays rapidly out the the edge of the contact area.

Figure 19 shows the force history applied to the rigid plate and the impulse history delivered to the surface for the normal incidence impact. (The non-dimensional time and force parameters defined in Section 1.3 are used in Figure 19 and in subsequent force and impulse histories in this report.)

2.1.2 Case B - 25° Oblique Impact on Rigid Plane

Case B treats a water sphere impacting a rigid surface at 25° obliquity, as shown in Figure 20. This is a 3-D problem. However, the oblique configuration in Figure 20 is *dynamically equivalent* to the configuration in Figure 21. If there is no friction between the water and the surface (a reasonable assumption), the problem in Figure 21 can be considered as axisymmetric insofar as the impacting sphere is concerned. The sphere will apply only normal forces to the rigid surface. Thus a solution to the impact problem of Figure 21 can be easily manipulated to obtain a solution for the configuration in Figure 20. A Galilean transformation to a moving coordinate system connects the two configurations. This is discussed in Appendix B.

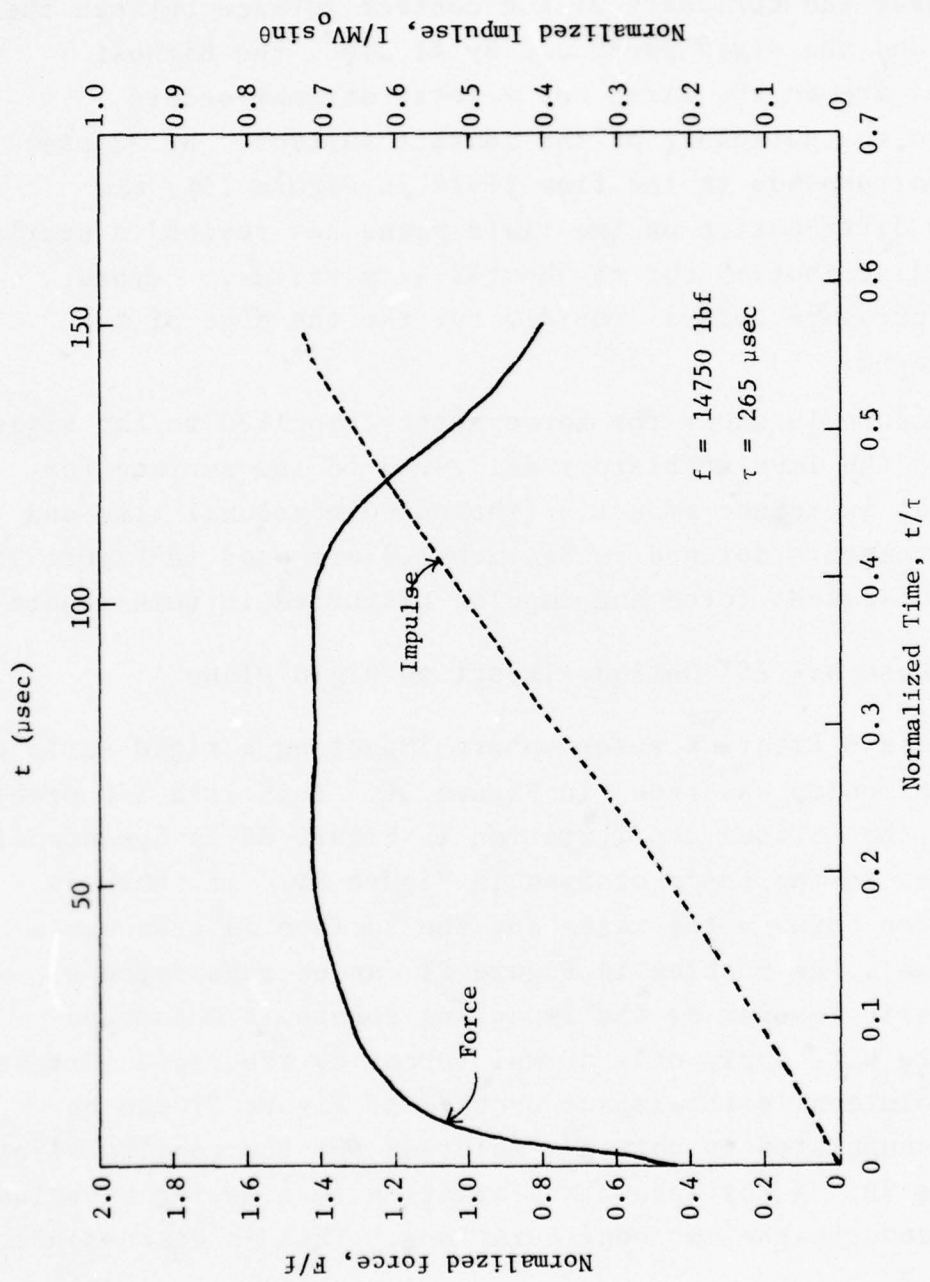


Figure 19. Normalized Force and Impulse Histories on Rigid Surface from 85 gm Water Sphere Impact at 675 fps (Case A)

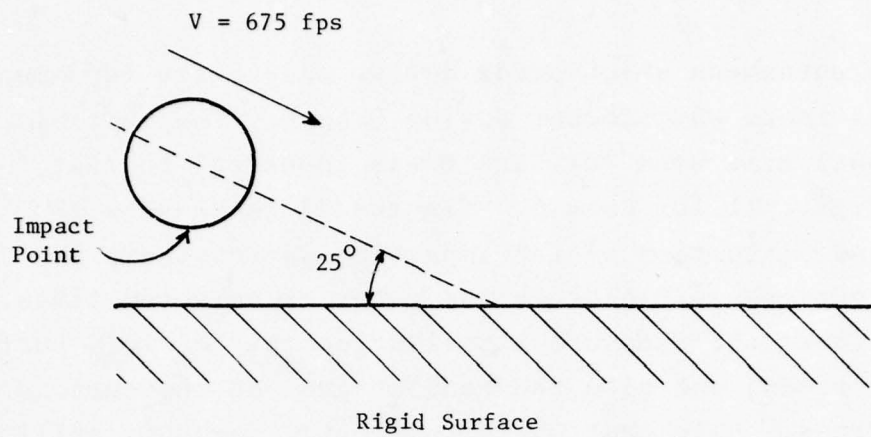


Figure 20. Geometry of 675 fps Impact of Water Sphere at 25° Obliquity on Stationary Rigid Surface (Case B)

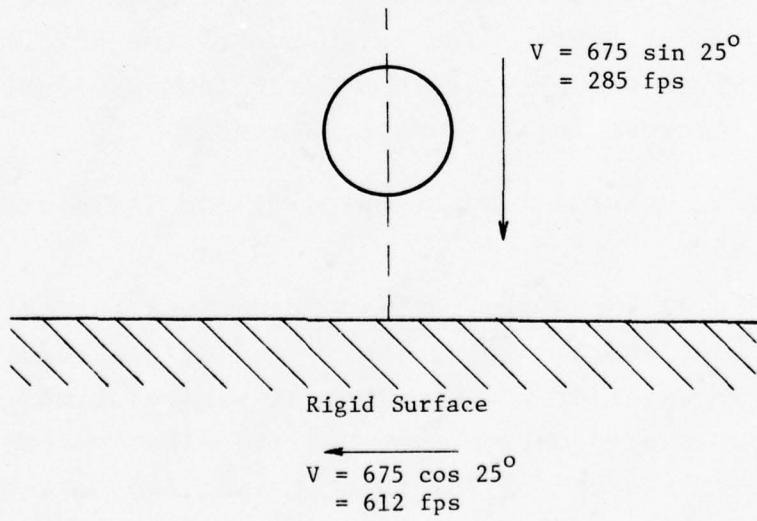


Figure 21. Dynamically Equivalent Configuration of Normal-Incidence Impact of Water Sphere on Moving Rigid Surface (Case B)

The phenomena which occur during Case B are fundamentally the same as those which occur during Case A. The initial computational grid used for Case B was identical to that shown in Figure 11 for Case A. Figures 22 to 25 show the location and distortion of the impacting water sphere as well as the pressure fields in the water at selected times. Figure 26 shows the pressure distribution on the rigid surface at several times, and also the contact area on the surface at these times. Note that while the contact area is still circular in this oblique impact case, the *center* of the contact area moves along the plate with a velocity of $675 \cos 25^\circ = 612$ fps.

Figure 27 shows the force and impulse histories for Case B.

2.2 IMPACTS ON A DEFORMABLE PLATE

The conditions used for the impacts on a rigid surface in Cases A and B were repeated using a 0.136-in thick stainless steel target plate. The influence of the deformation of the target on the pressure and force loading functions was of primary interest in these calculations.

2.2.1 Case C - Normal Impact on 0.136-in. Stainless Steel Plate

Figure 28 shows the initial conditions for this solution. Figures 29, 30, and 31 show velocity and grid deformation fields in the water drop and target at various times. The largest plastic deformation (generalized plastic strain) experienced by the end of the solution was 4.3 percent, which occurred on the rear surface of the plate under the impact point (i.e. at the crown of the bulge). The plate will remain deformed after the droplet interaction ceases.

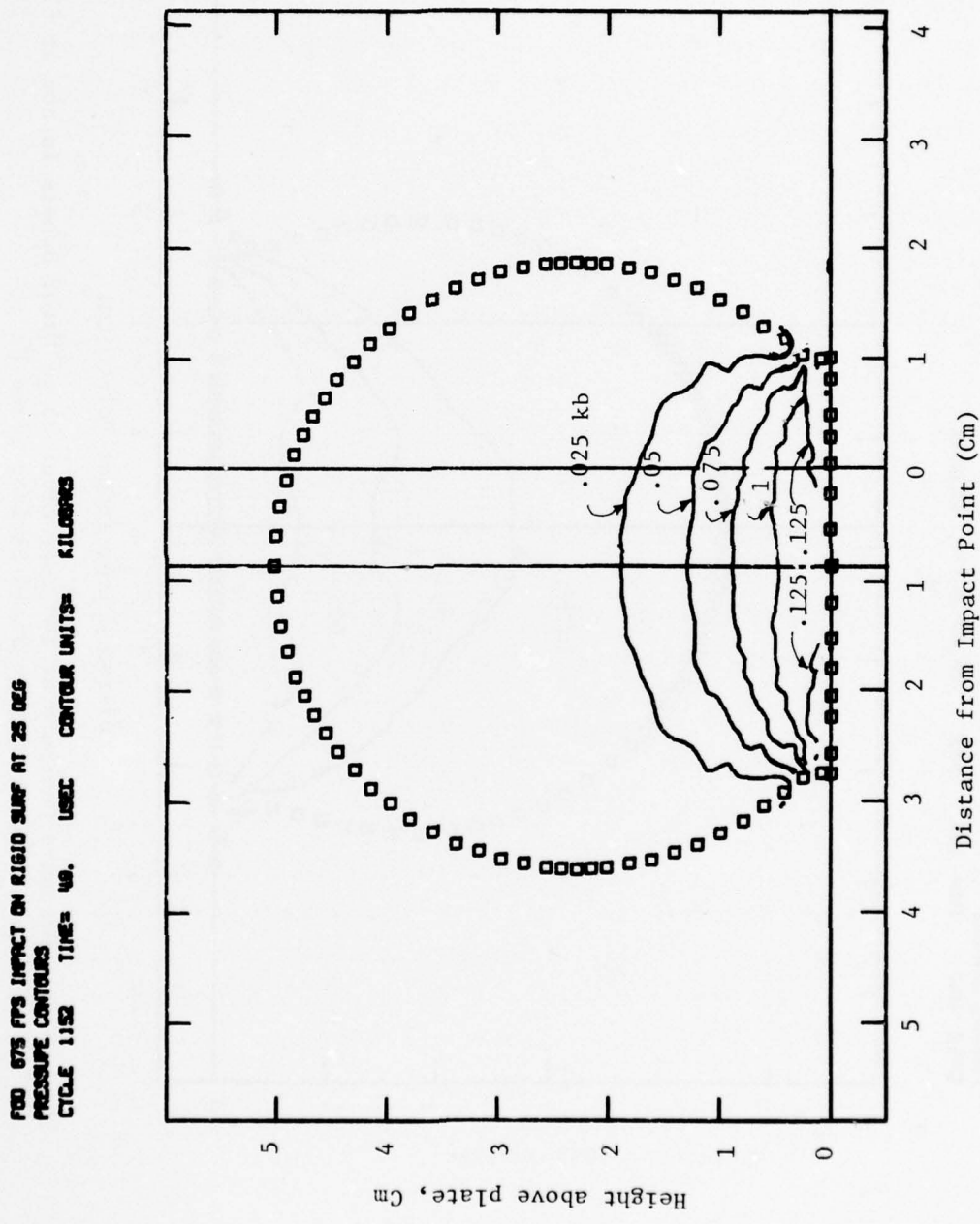


Figure 22. Pressure Contours at 49 μ sec After 85 gm Water Sphere Impact at 675 fps and 25° Obliquity on Rigid Surface (Case B)

FID 675 FPS IMPACT ON RIGID SURF AT 25 DEG
PRESSURE CONTOURS
CYCLE 1007 TIME= 100. USEC CONTOUR UNITS= KILOBARS

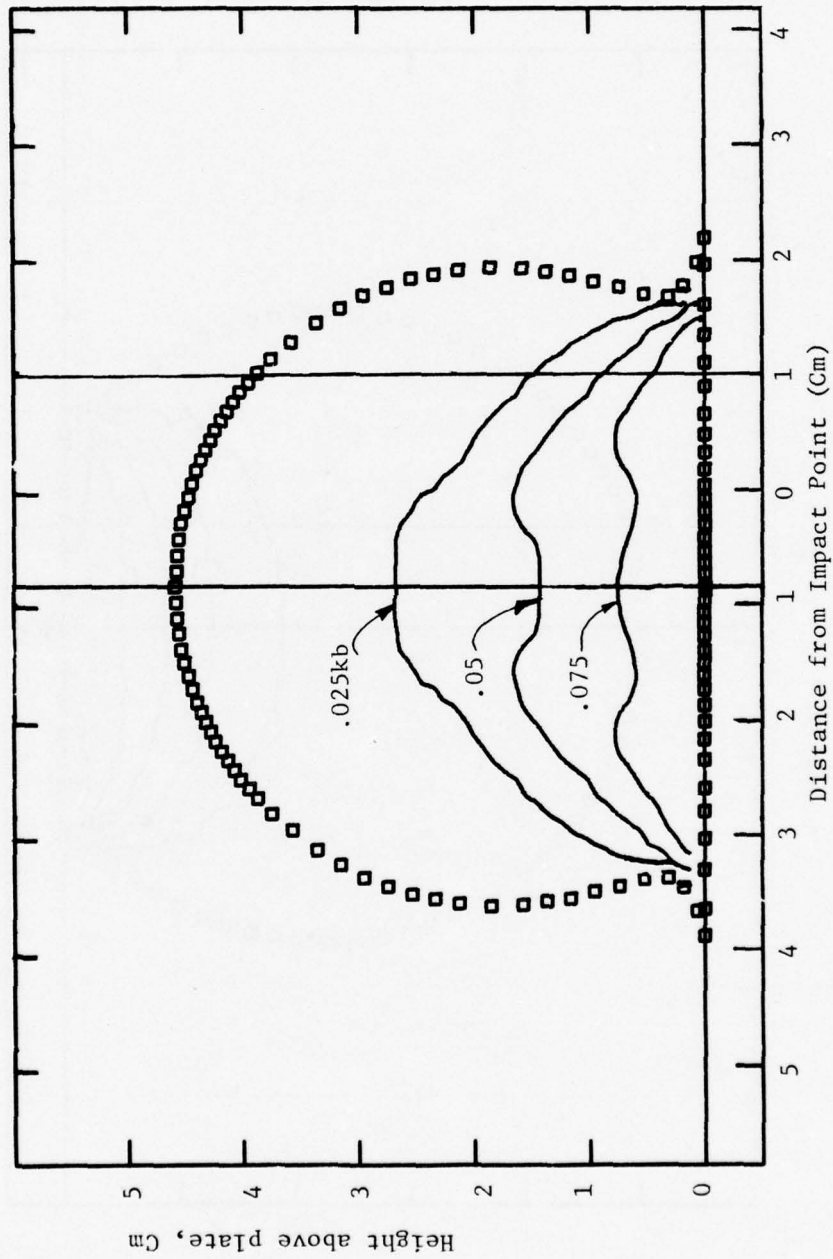


Figure 23. Pressure Contours at 100 μ sec After 85 gm Water Sphere Impact at 675 fps and 25° Obliquity on Rigid Surface (Case B)

FID 675 FPS IMPACT ON RIGID SURF AT 25 USEC
PRESSURE CONTOURS
CYCLE 2004 TIME= 146. USEC CONTOUR UNITS KILOPAS

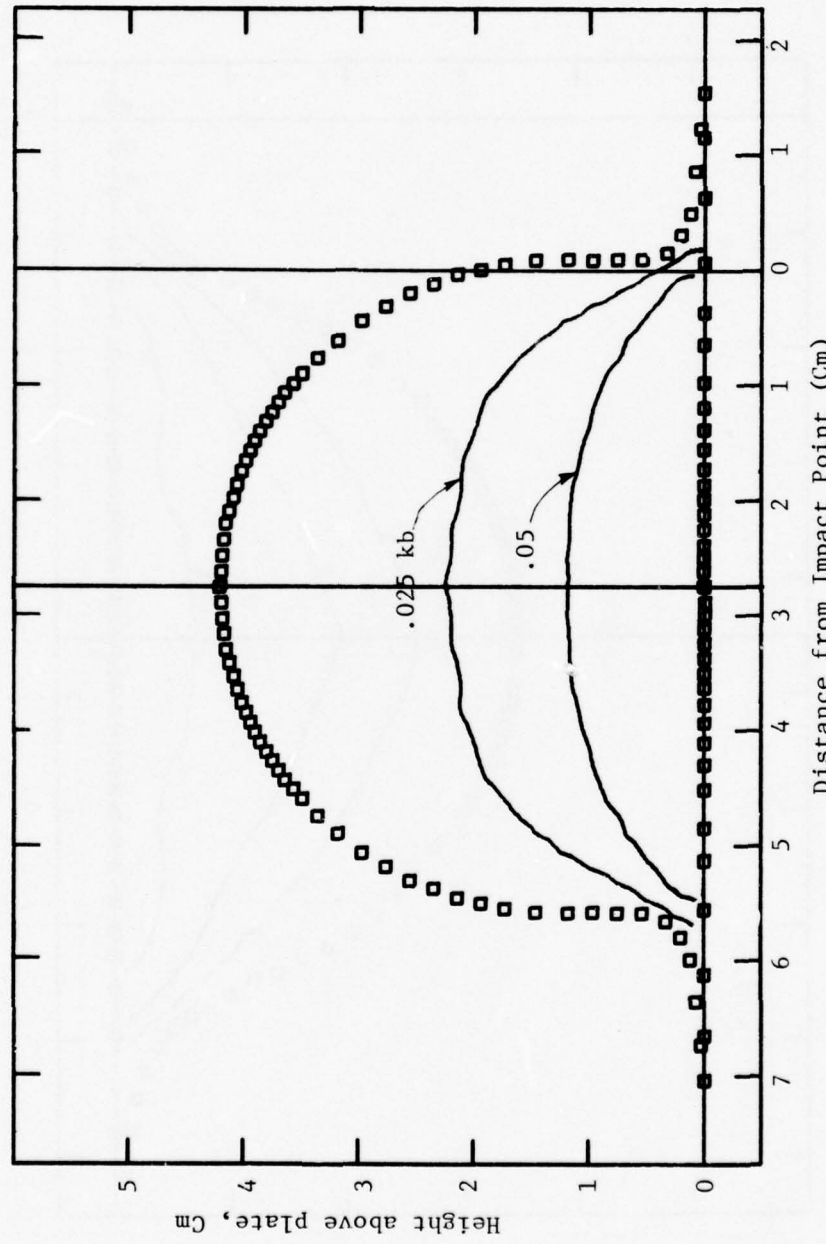


Figure 24. Pressure Contours at 146 μ sec After 85 gm Water Sphere Impact at 675 fps and 25° Obliquity on Rigid Surface (Case B)

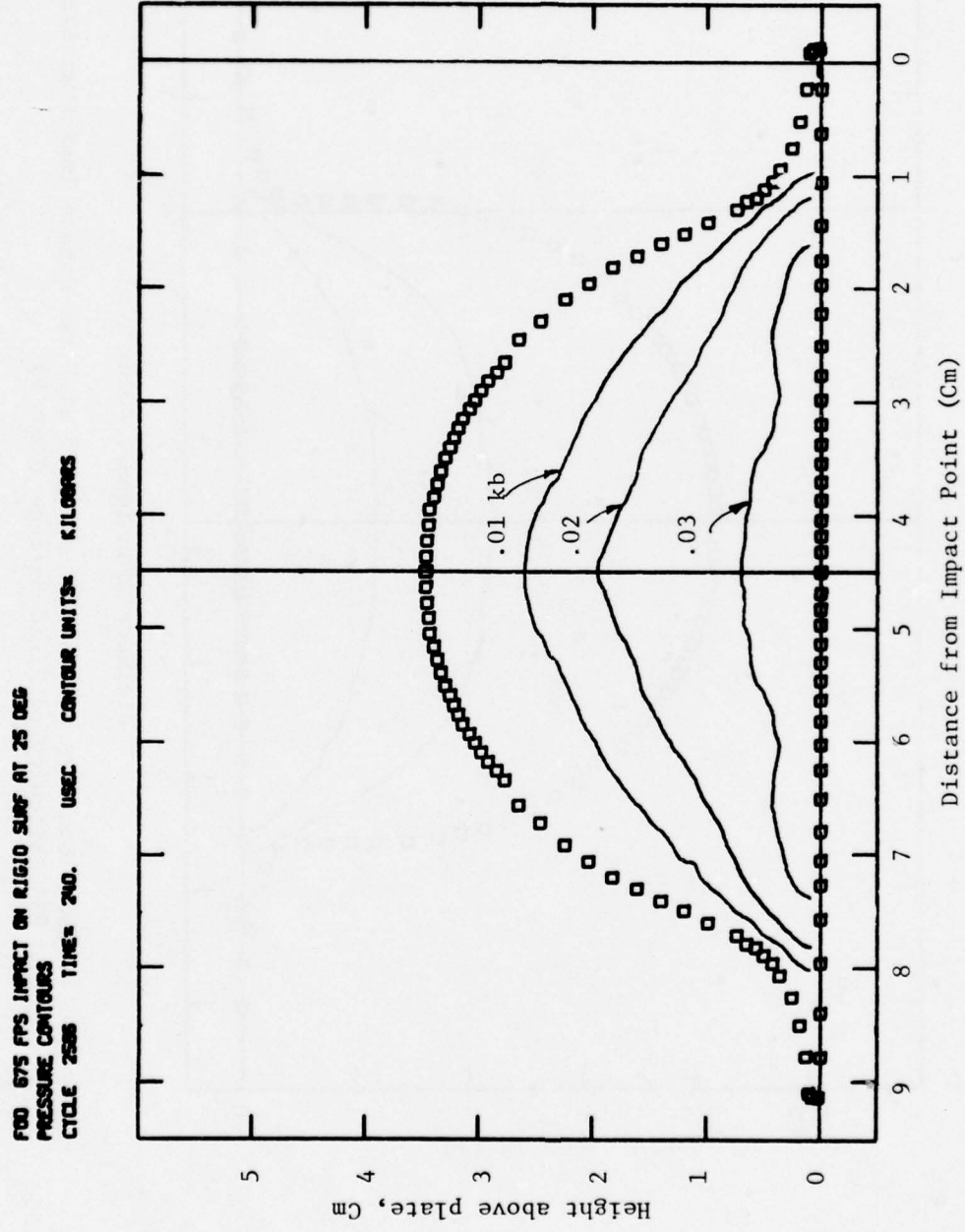
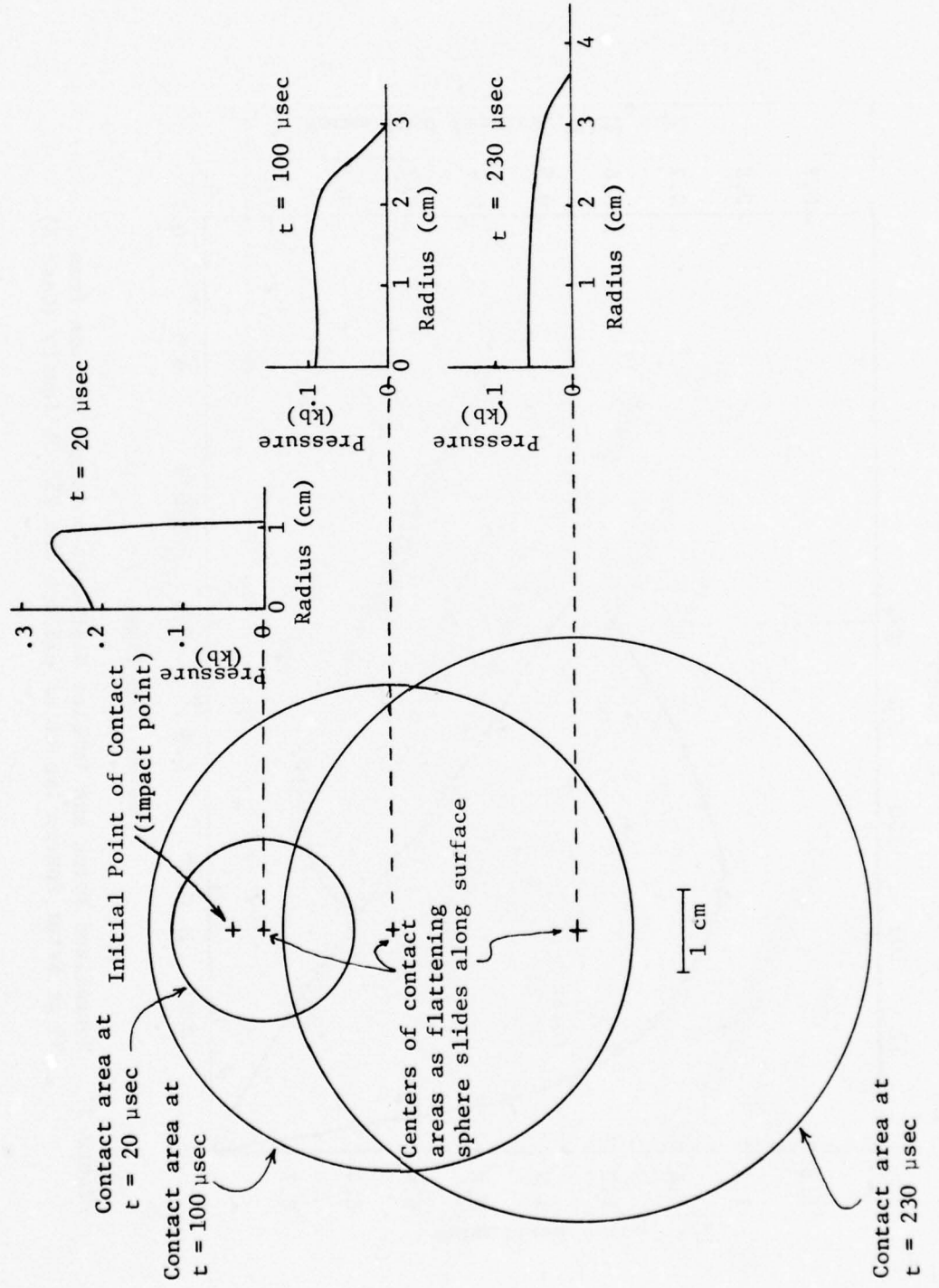


Figure 25. Pressure Contours at 240 μ sec After 85 gm Water Sphere Impact at 675 fps and 25° Obliquity of Rigid Surface (Case B)



Contact area at

$t = 230 \mu\text{sec}$

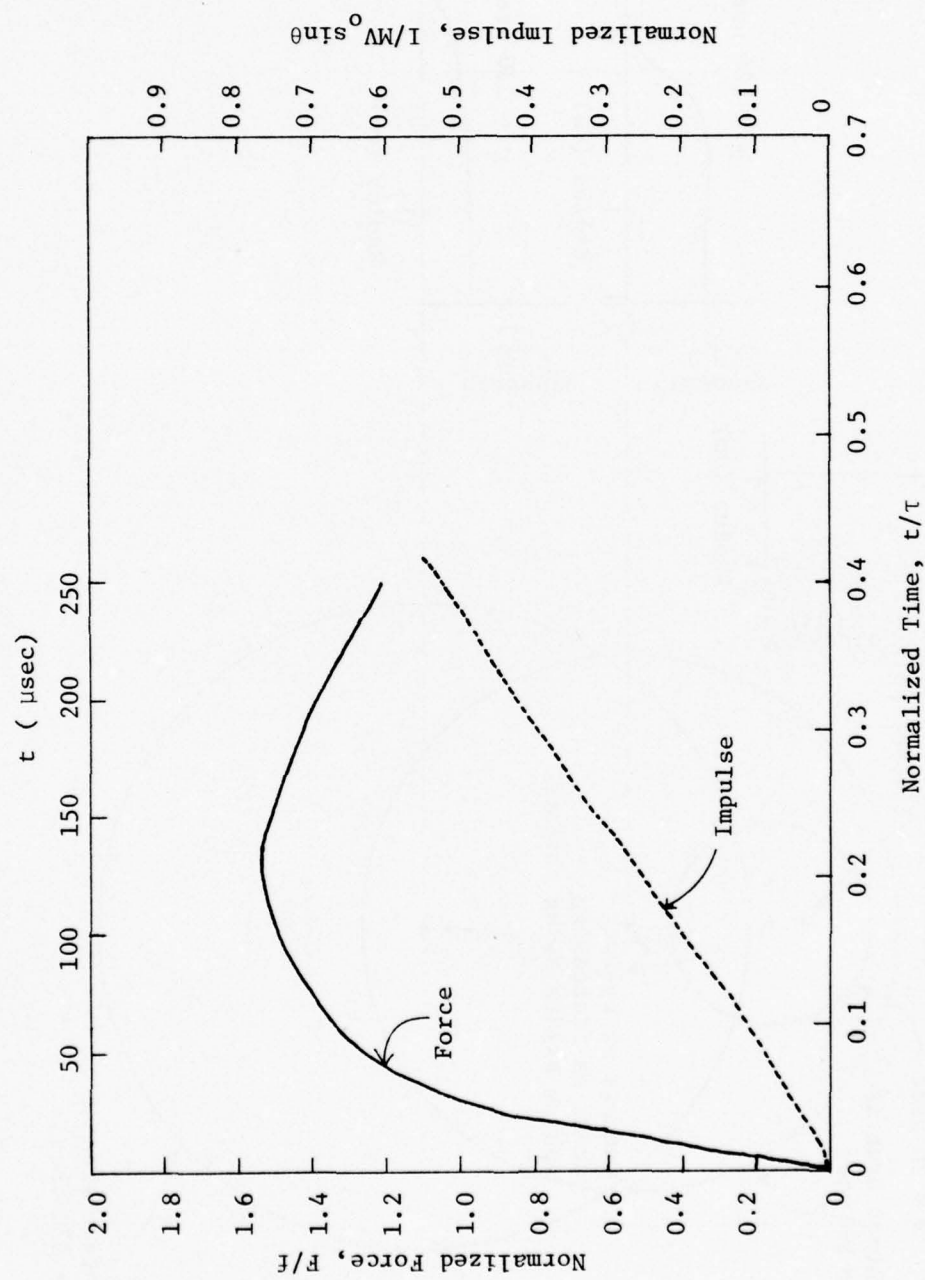


Figure 27. Normalized Force and Impulse Histories on Rigid Surface from 85 gm Water Sphere Impact at 675 fps and 25° Obliquity (Case B)

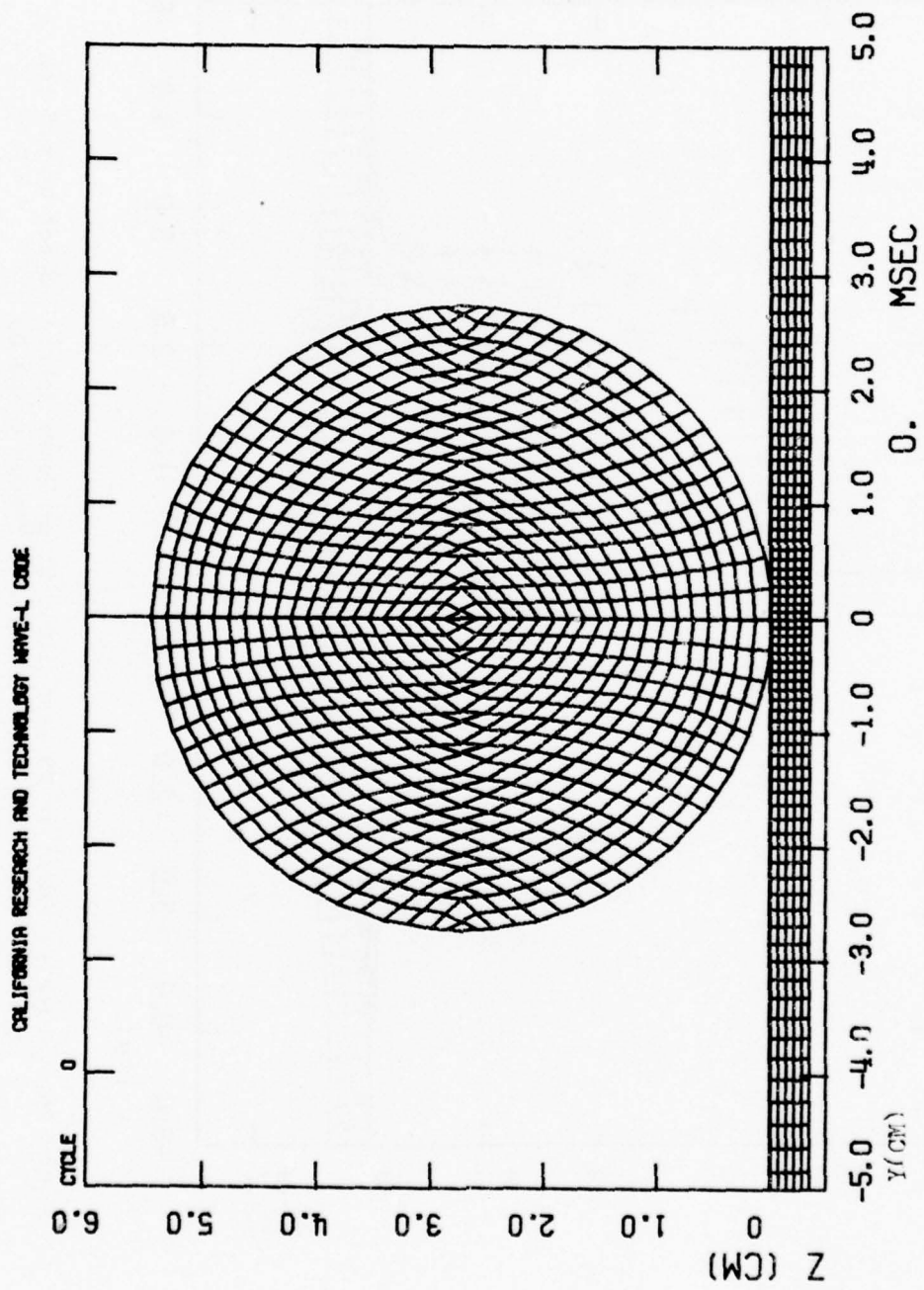


Figure 28. Initial Computational Grid for 85 gm Water Sphere Impact at 675 fps on 0.136-in. Stainless Steel Plate (Cases C and D)

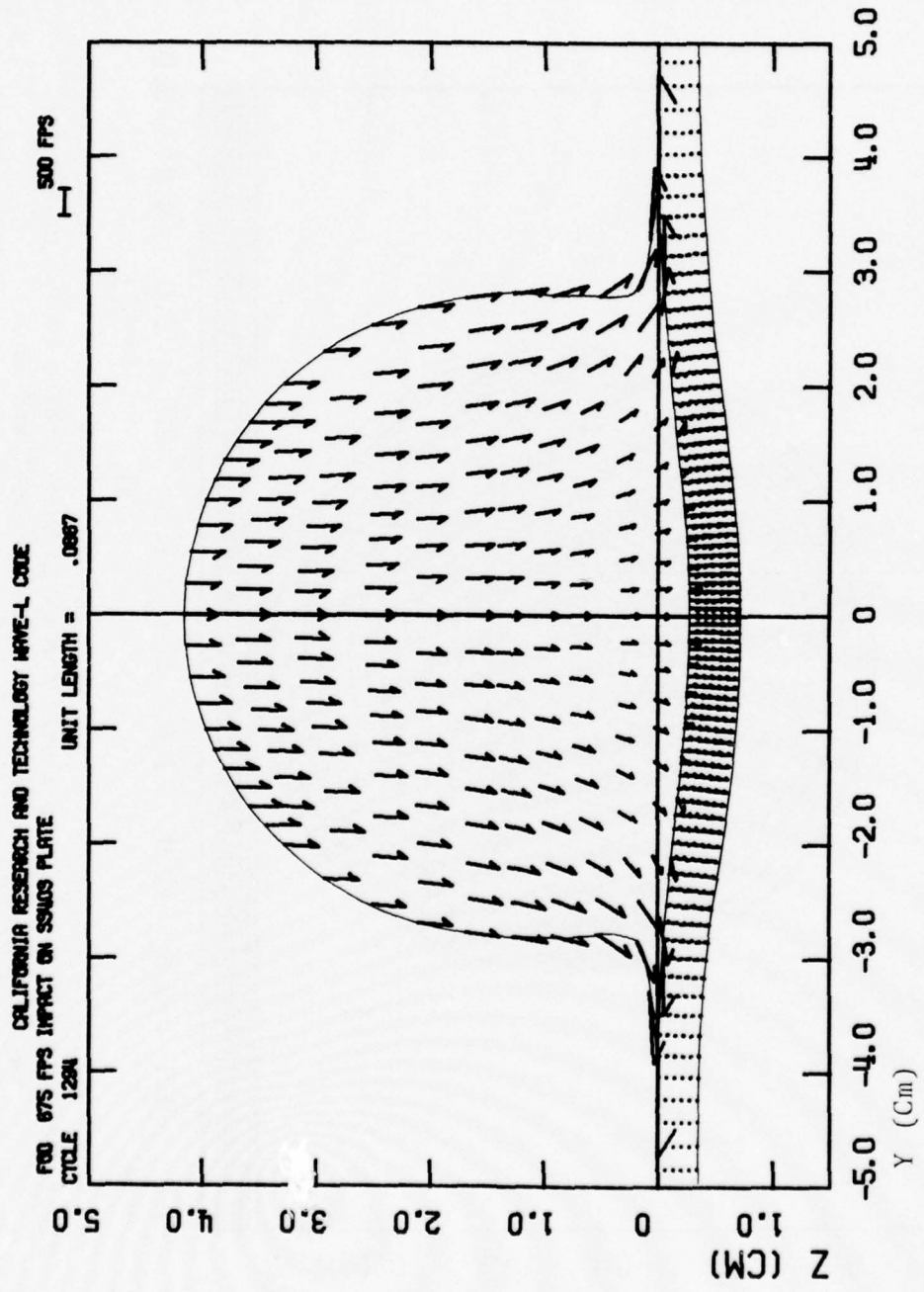


Figure 29. Velocity Field at 65 μ sec After 85 gm Water Sphere Impact at 675 fps on 0.136-in. Stainless Steel Plate (Cases C and D)

CALIFORNIA RESEARCH AND TECHNOLOGY WAVE-L CODE
FNU 675 FPS IMPACT ON SS305 PLATE
CITLE 2077

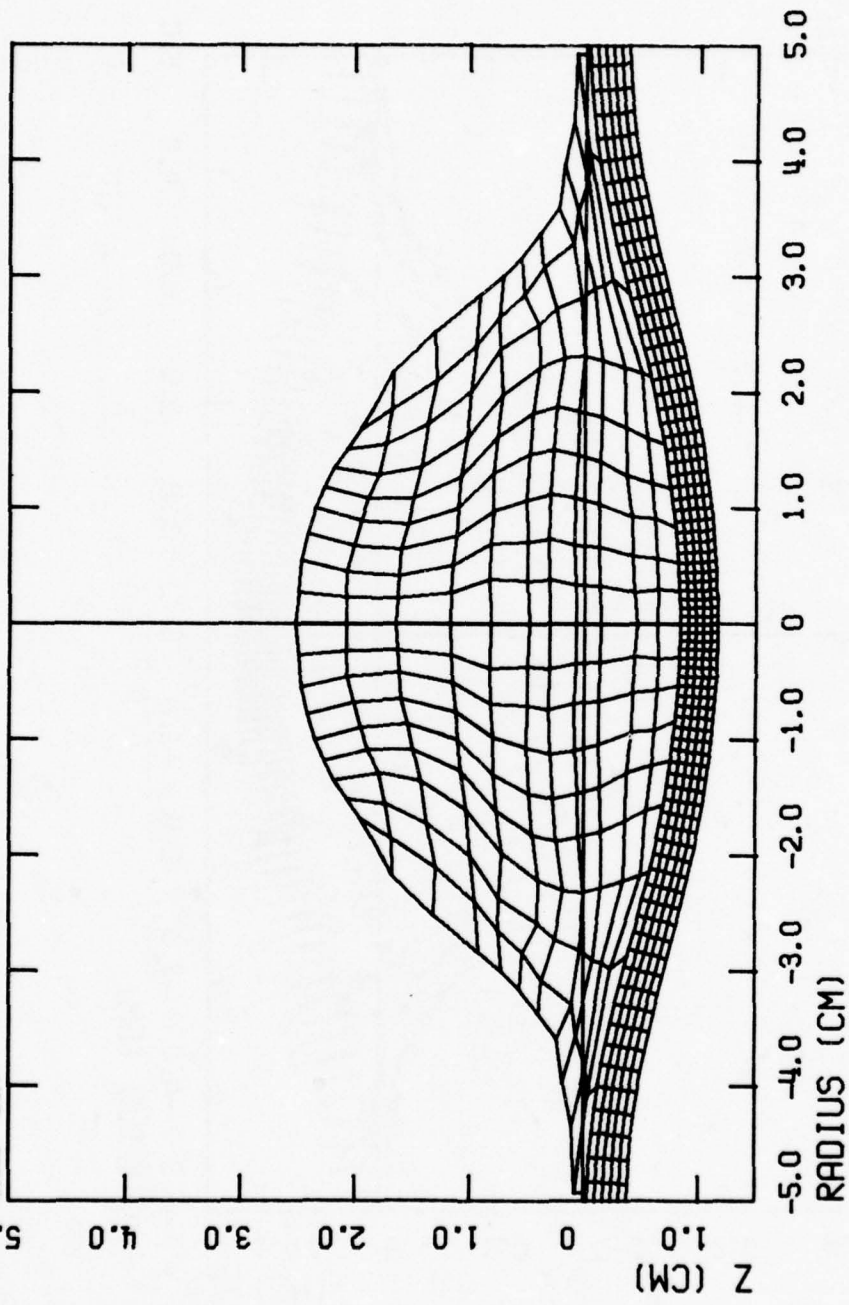


Figure 30. Computational Grid at 152 μ sec After 85 gm Water Sphere Impact at 675 fps on 0.136-in. Stainless Steel Plate (Cases C and D)

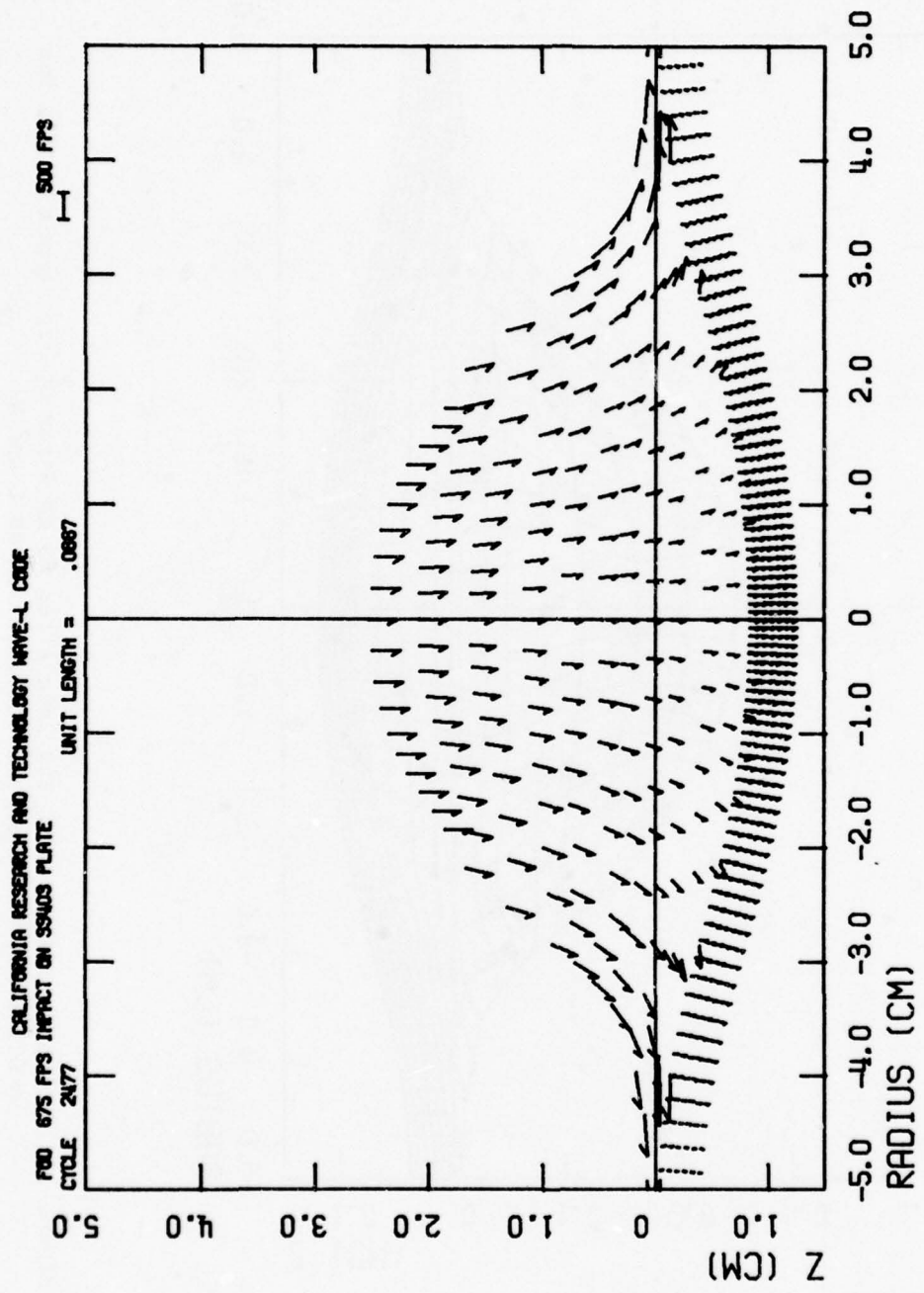


Figure 31. Velocity Field at 152 μ sec After 85 gm Water Sphere Impact at 675 fps on 0.136-in. Stainless Steel Plate (Cases C and D)

Figure 32 shows stress contours in the drop and in the target at 64 μ sec. Tensile stresses in excess of 2 kbar (~29,000 psi) have developed on the rear surface of the target.

Figure 33 compares the impulse delivered and forces applied to the target versus time in Cases A (rigid surface) and C (0.136-in. stainless steel plate). It is seen that the deflection of the plate affects the magnitude and timing of the applied forces, with the forces being lower in the deformable case.

2.2.2 Case D - 25° Oblique Impact on 0.136-in. Stainless Steel Plate

The Case B calculation described in Section 2.1.2 treated a 25° oblique impact on a rigid plate. By comparing Figures 26 and 3, it is seen that pressure profiles in the 25° oblique impact on a rigid surface are very low as compared to profiles in the normal impact (i.e. Case B vs Case A). This is because the normal component of the velocity for the 25° obliquity impact is only 285 fps. Thus it was expected that the plate deflection in a 25° impact onto a 0.136-in. stainless steel (*deformable*) plate would be much smaller than seen in the previous section for the normal impact onto the same plate (Case C). We therefore used the same approach in Case D to analyze the 25° impact on a deformable plate as had been used in the rigid plate oblique impact, (Case B) i.e., a Galilean transformation was made to the coordinate system in Figure 21, in which the sphere strikes the plate normally at $675 \sin 25^\circ = 285$ fps, and the plate moves laterally at $675 \cos 25^\circ = 612$ fps. The motion of the plate is ignored during the integration because, 1) shear stresses (friction) across the interface are assumed to be negligible, and 2) the deflection of the plate is assumed to be small.

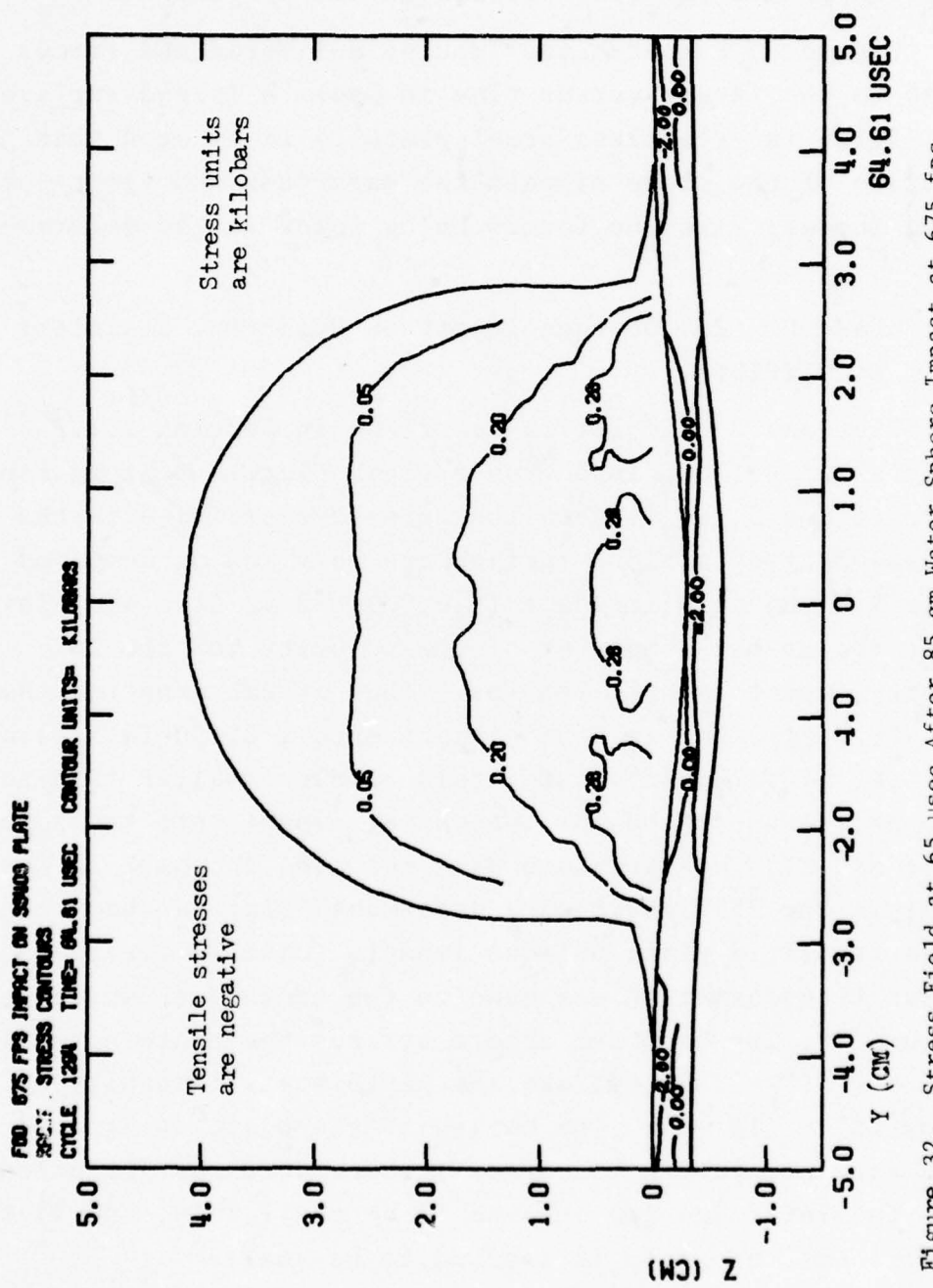


Figure 32. Stress Field at 65 μ sec After 85 gm Water Sphere Impact at 675 fps on 0.136-in. Stainless Steel Plate (Cases C and D)

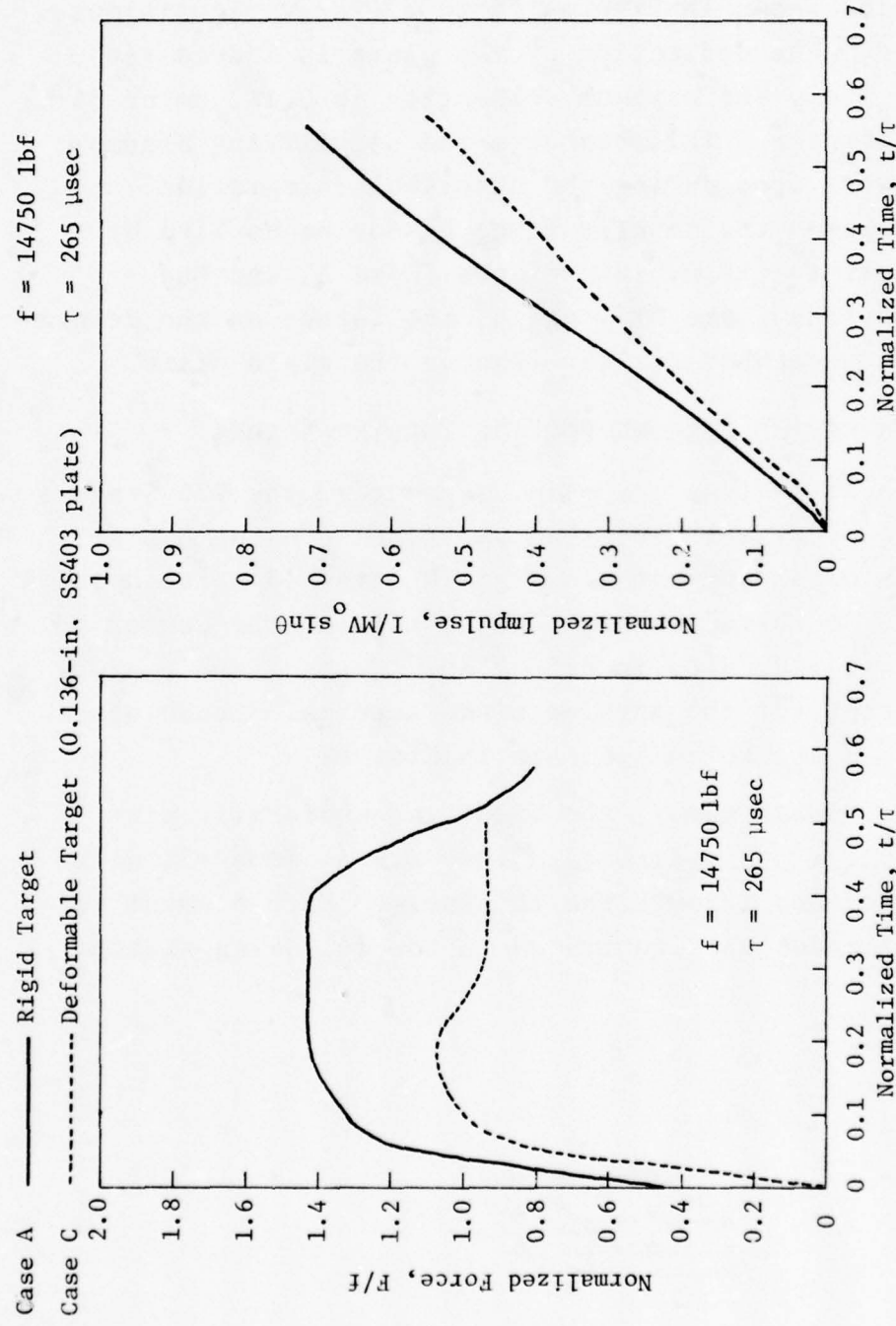


Figure 33. Comparison of Normalized Force and Impulse Histories on Rigid and Deformable Targets Due to 675 fps Impacts of 85 gm Water Spheres (Cases A and C)

Using these assumptions, the velocity, grid, and pressure fields shown in Figures 34 to 37 for various times were obtained. The deflection of the plate is indeed seen to be small, i.e., the maximum deflection is 0.162 cm or 3% of the droplet diameter. This supports the simplifying assumptions which were used during the numerical integration. Figure 38 compares the impulse force histories applied by oblique impacts to the rigid surfaces (Case B) and the deformable surface (Case D). Again, the forces on the deformable plate are somewhat smaller than on the rigid plate.

2.3 IMPACTS ON THE LEADING EDGE OF TURBINE BLADES

For these analyses, a 6-in. segment of the J79 Stage 1 Turbine blade profile at 70% span was modeled using 3-D NONSAP². The blade segment was rigidly attached at both ends, and the impact occurred on the leading edge at the center of the segment, as indicated in Figure 39. Cases E and F are identical except for the turbine blade material (Stainless Steel in Case E and Boron Aluminum in Case F).

In the NONSAP model, the blade was uniformly partitioned in the x and y-direction into 6 x 6 elements, with one element defined through the thickness. Each element is defined by 12 nodes as illustrated in the following sketch:



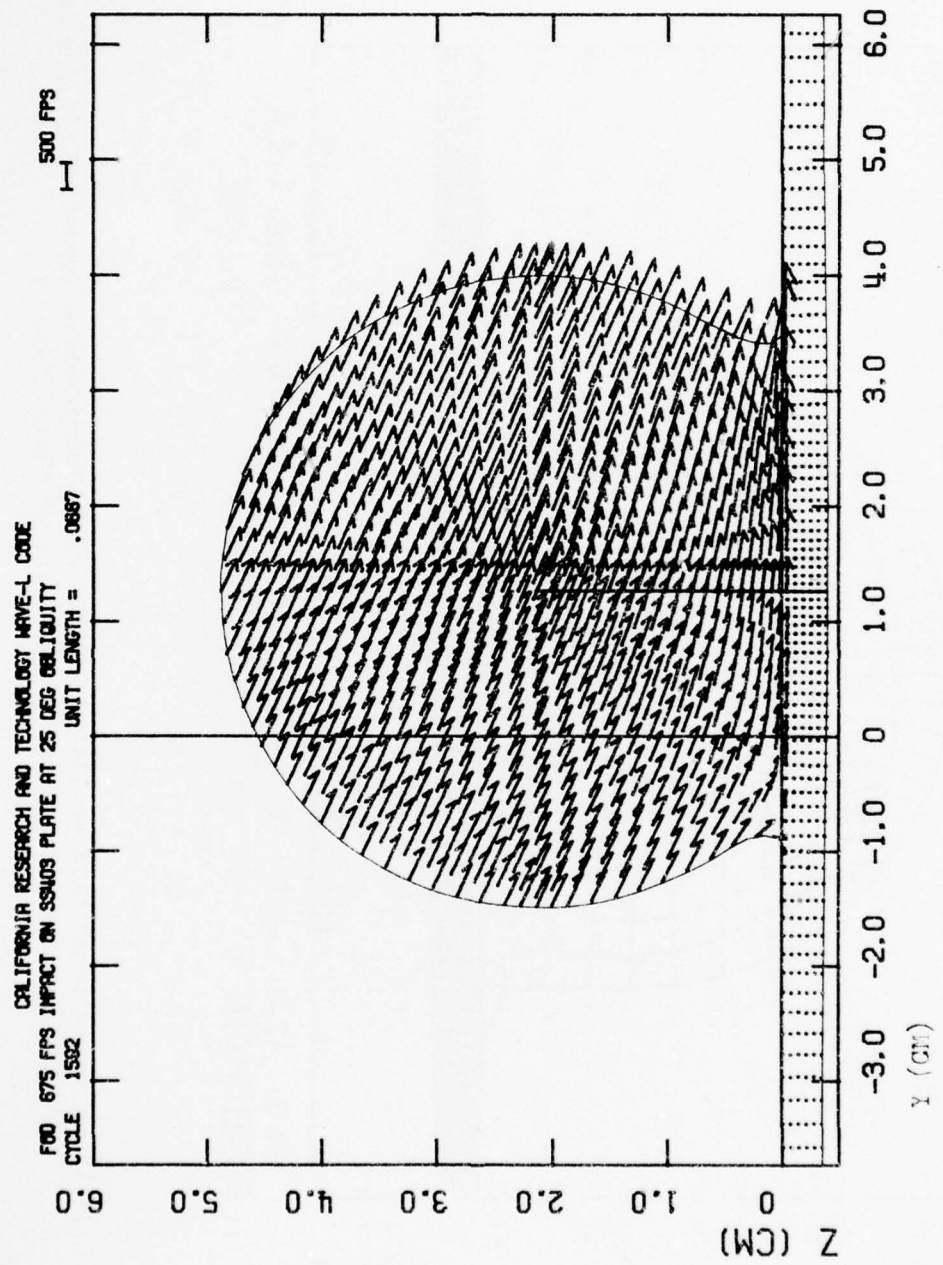


Figure 34. Velocity Field at 68 μ sec After 85 gm Water Sphere Impact at 675 fps and 25° Obliquity on 0.136-in. Stainless Steel Plate (Case D)

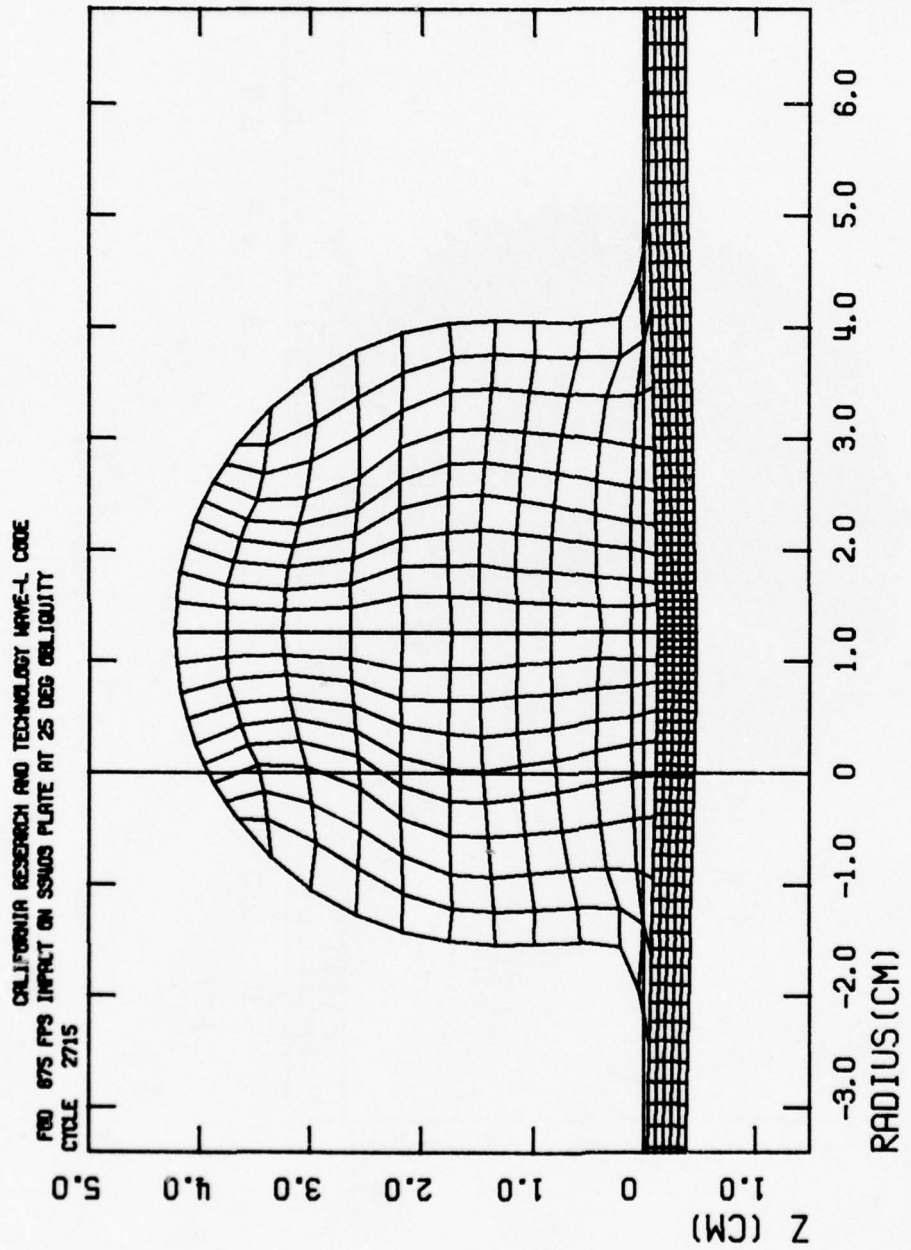


Figure 35. Computational Grid at 144 μ sec After 85 gm Water Sphere Impact at 675 fps and 25° Obliquity on 0.136-in. Stainless Steel Plate (Case D)

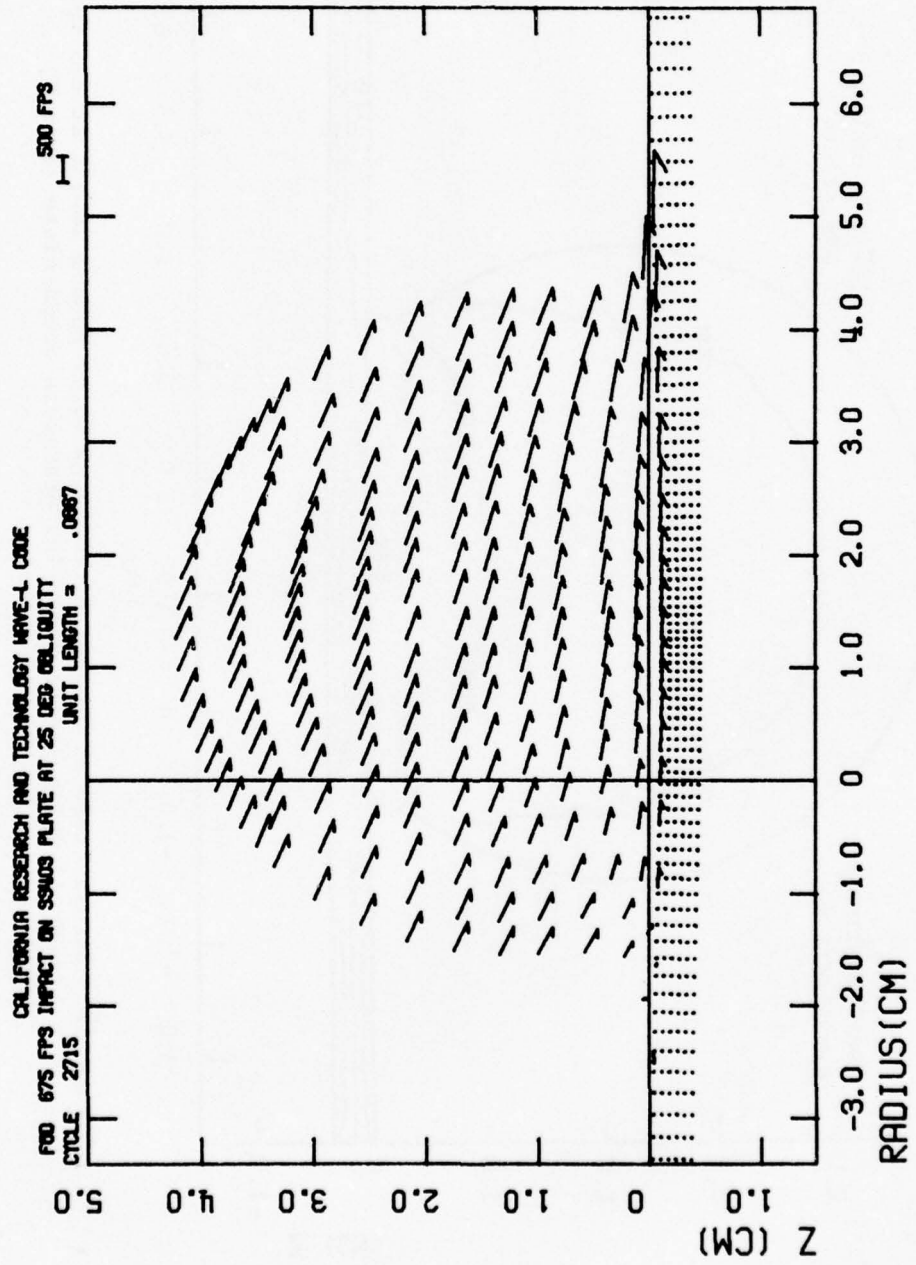


Figure 36. Velocity Field at 144 μ sec After 85 gm Water Sphere Impact at 675 fps and 25° Obliquity on 0.136-in. Stainless Steel Plate (Case D)

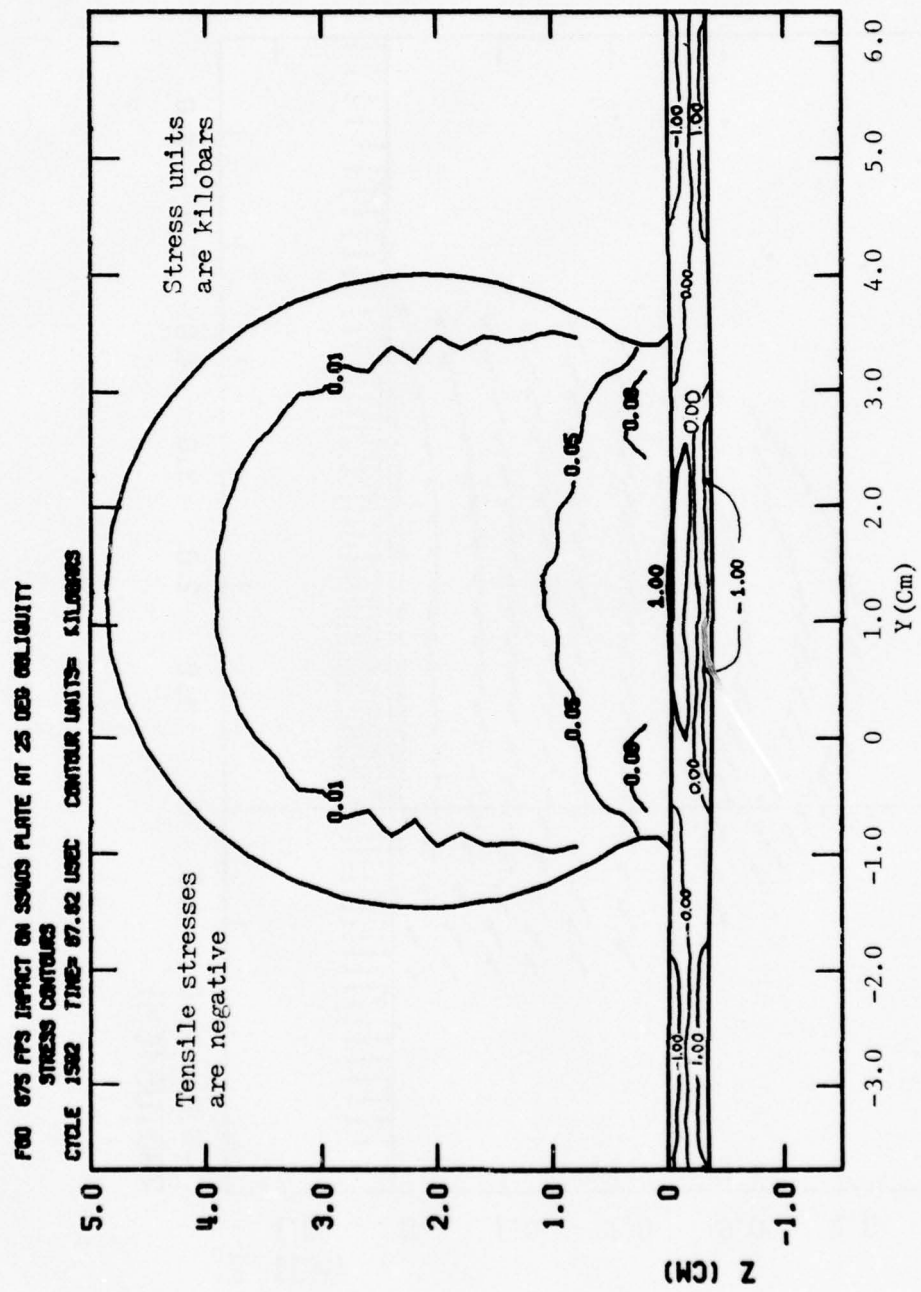


Figure 37. Stress Field at 68 usec After 85 gm Water Sphere Impact at 675 fps
 and 25° Obliquity on 0.136-in. Stainless Steel Plate (Case D)

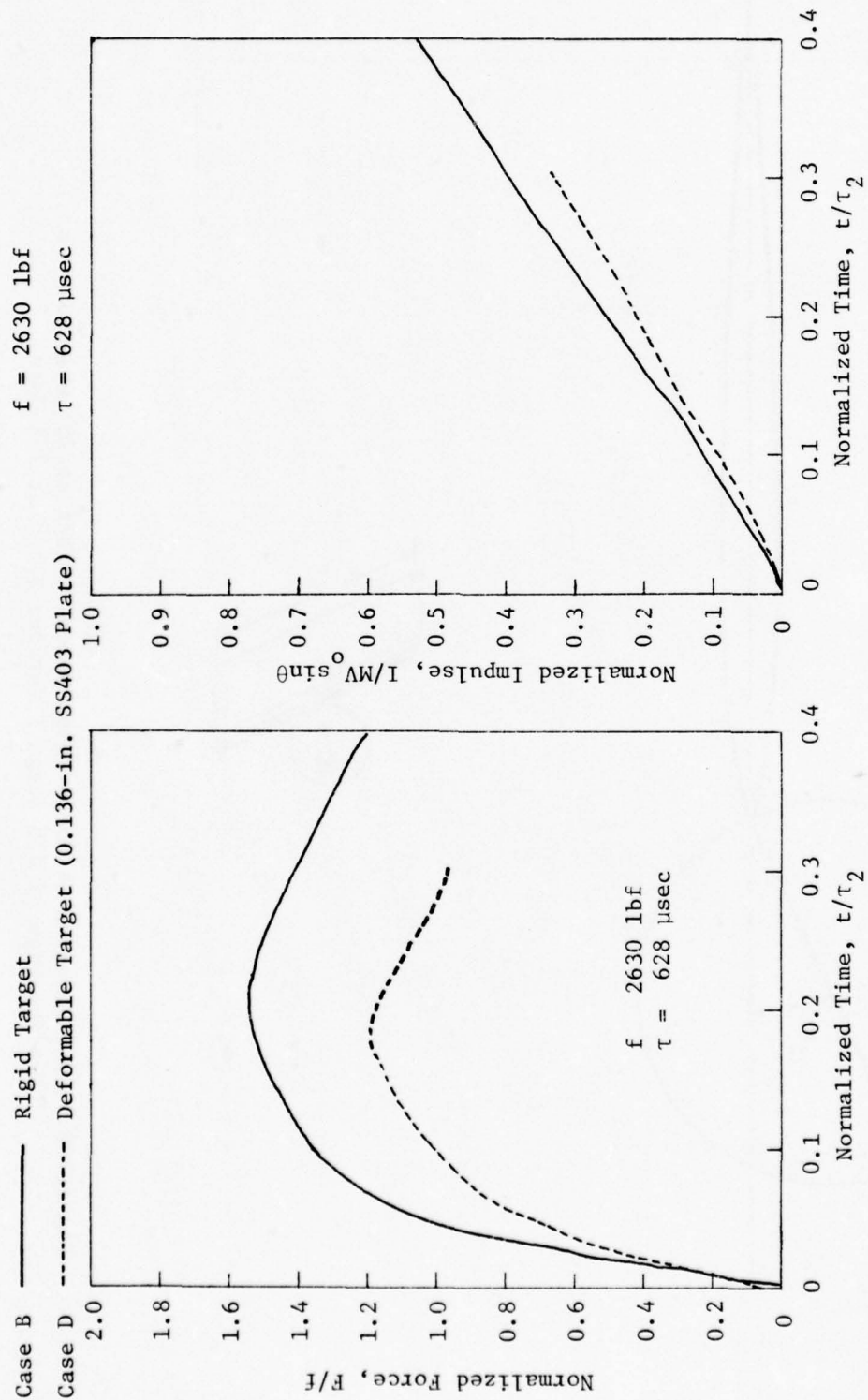


Figure 38. Comparison of Normalized Force and Impulse Histories on Rigid and Deformable Targets Due to 675 fps Impacts at 25° Obliquity of 85 gm Water Spheres (Cases B and D)

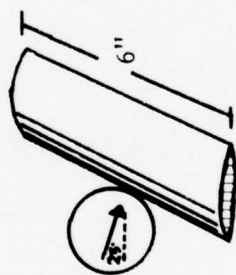
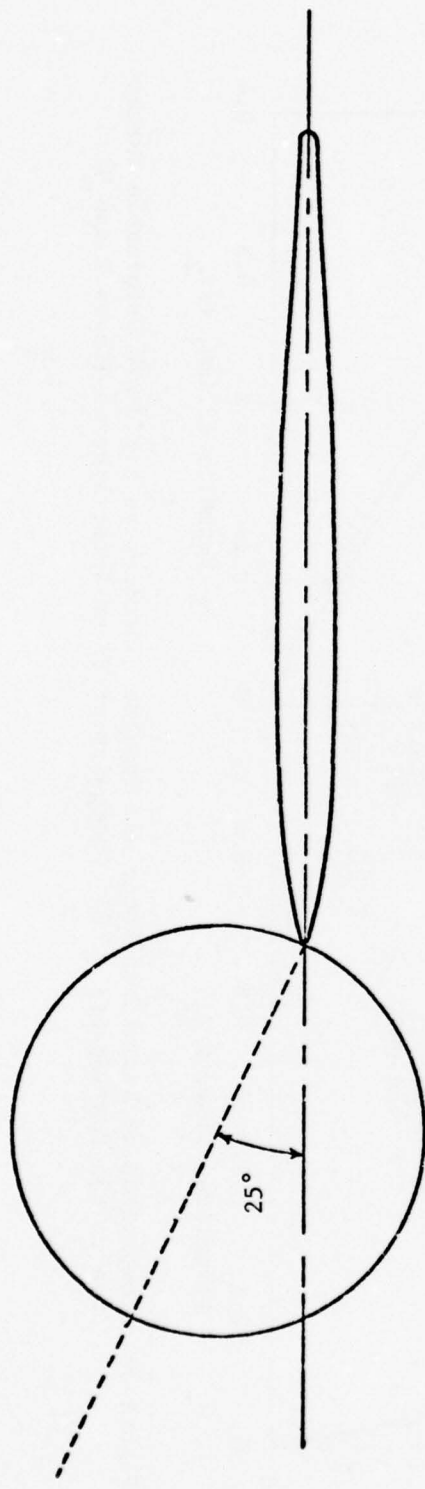


Figure 39. Configuration of 85-gm Water Sphere Impact at 25° Obliquity on Leading Edge of J79 Stage 1 Turbine Blade at 70% Span

For these solutions, the loading from the bird impact was represented by a pressure function derived from the 2-D finite-difference solution described in Section 2.1.2 of a water sphere impacting at 675 fps on a rigid surface at 25° obliquity (Case B). Essentially, it was assumed that the leading edge neatly cuts the sphere in half along the diametral plane which is shown as a dashed line in Figure 39. The blade is impacted only by the *upper* hemisphere. The impact load from this hemisphere is determined from the pressure-radius-time curves from Case B (e.g. in Figure 26), taken around a 180° arc. The contact surface, and hence the impact load, sweeps across the top surface of the blade at $V_0 \cos\theta = 675 \cos 25^\circ = 612$ fps

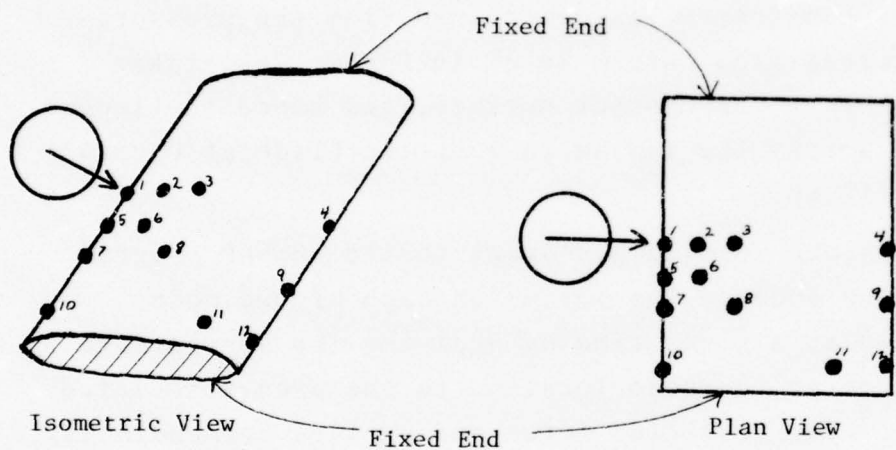
The pressure loading was input to the NONSAP program as forces on the nodes. The forces on each of the nodes were calculated at a given time by applying the appropriate loading pressure at the node location to the area associated with the node. The resulting force was applied perpendicular to the blade surface at the location of the node. Thus, the forces from the Case B solution were rotated to account, at least to first order, for the fact that the blade is not flat.

The blade materials in Cases E and F were characterized as linear elastic solids. The values defining the material properties are listed below:

<u>Case No.</u>	<u>Material</u>	<u>Density</u>	<u>Young's Modulus</u>	<u>Poisson's Modulus</u>
E	SS 403	7.86 gm/cm ³	1.965 Mb	0.285
F	Boron-Alum.	2.40 gm/cm ³	1.379 Mb	0.31

2.3.1 Stainless Steel (SS 403) Blade

Figures 40 to 43 show vertical (z -direction) displacement as a function of time at various stations on the stainless steel blade. Negative deflections indicate that the station is depressed, positive deflections mean that the station has risen. The following sketch shows the locations of output stations.



The maximum deflection for the SS403 blade was about 0.2 cm, which occurs at the impact point at about 250 μ sec. Figure 40 shows 4 stations along the center of the blade. Stations 1, 2, and 3, which are near the impact point, have initial downward displacements. Station 4, on the trailing edge of the blade, first displaces upward, reaching an upward maximum displacement at roughly 200 μ sec.

Figure 41 shows displacement histories of various stations along the leading edge. Initial displacement is always downward, and the time to peak deflection is consistently

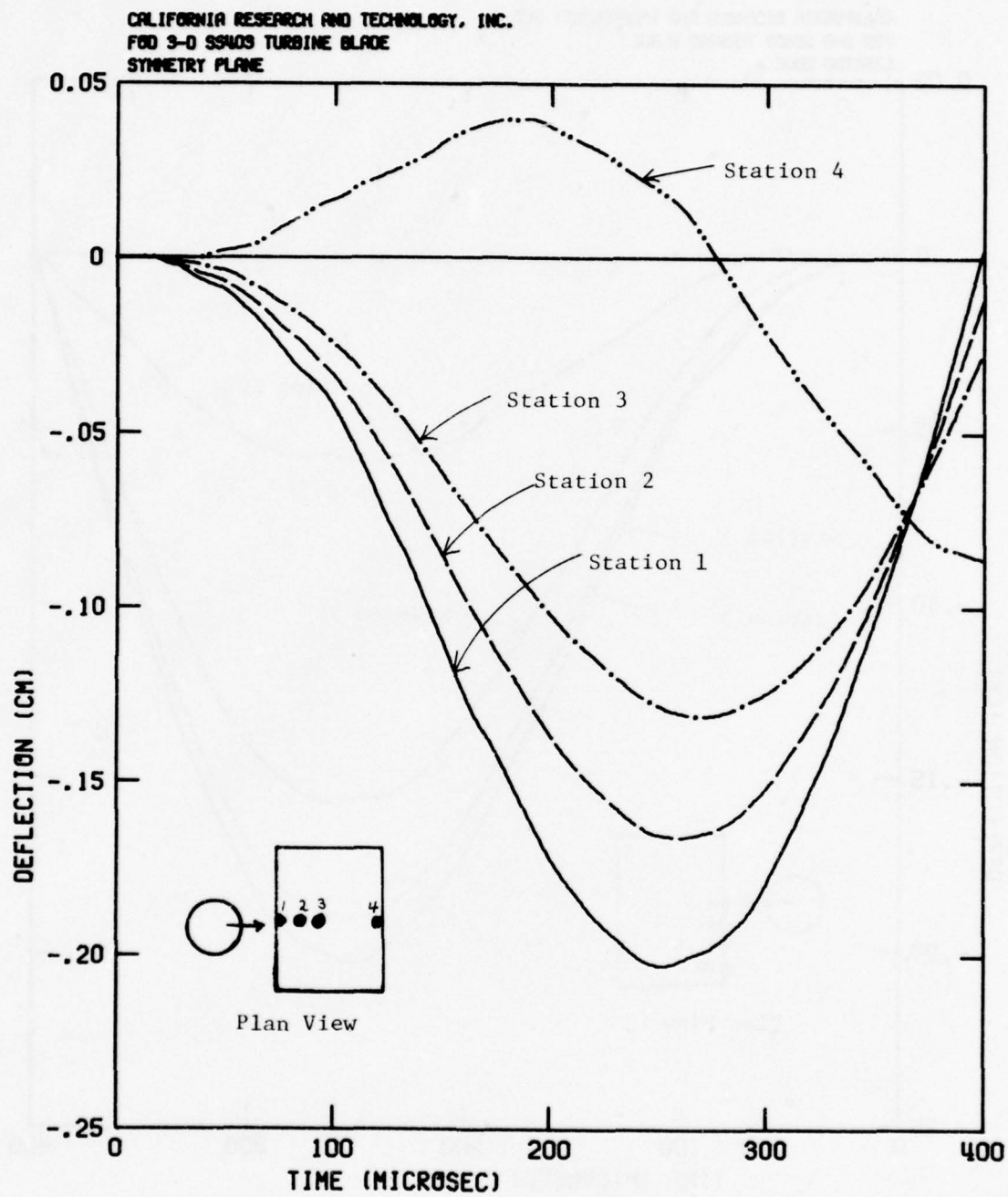


Figure 40. Vertical Displacement Histories at Selected Points Downstream of Impact of 85-gm Water Sphere at 25° Obliquity on Leading Edge of Stainless Steel (SS403) Blade (Case E)

CALIFORNIA RESEARCH AND TECHNOLOGY, INC.
FOD 3-D SS403 TURBINE BLADE
LEADING EDGE

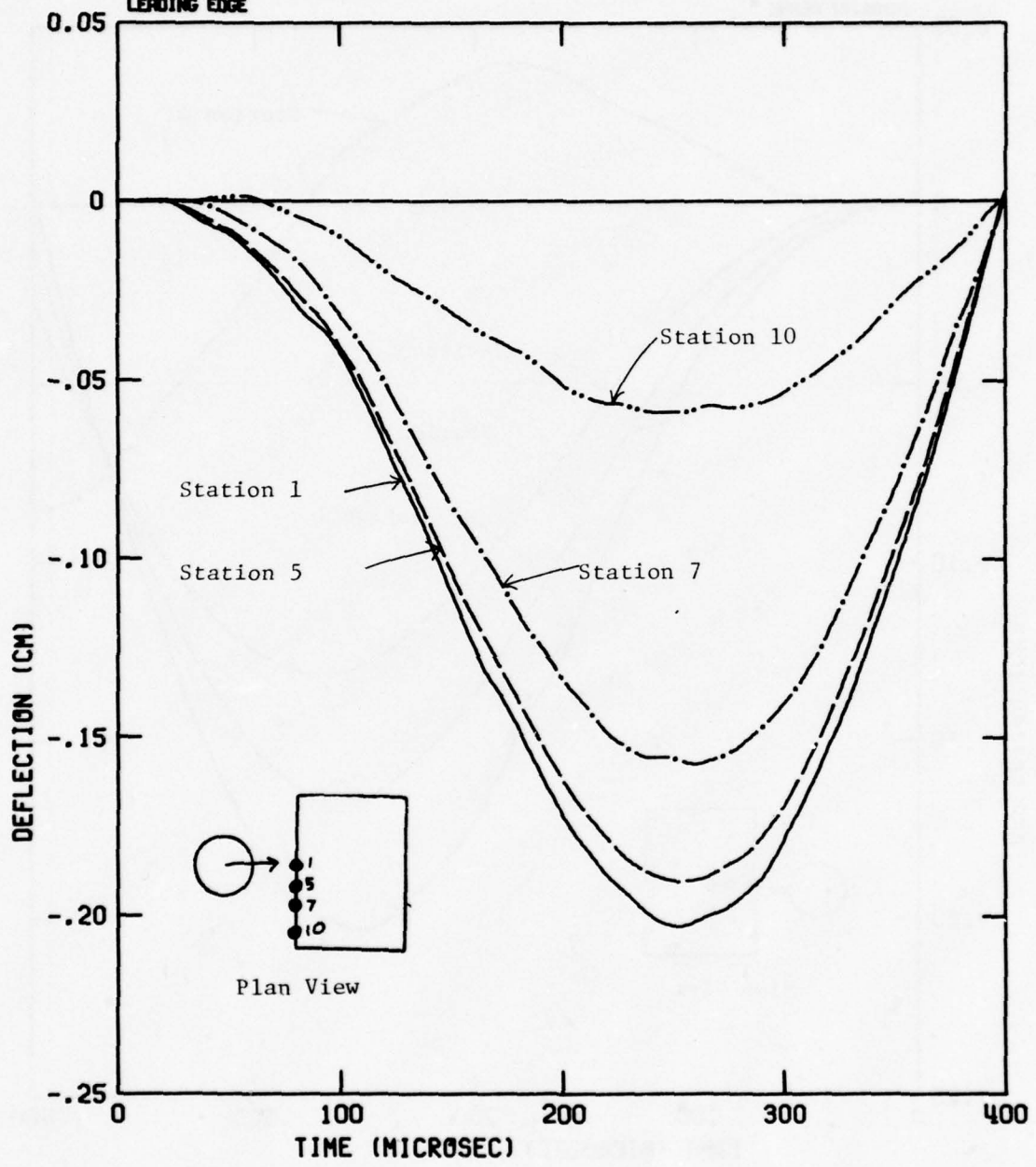


Figure 41. Vertical Displacement Histories at Selected Points Along Leading Edge of Stainless Steel (SS403) Blade Impacted by 85-gm Water Sphere at 25° Obliquity (Case E)

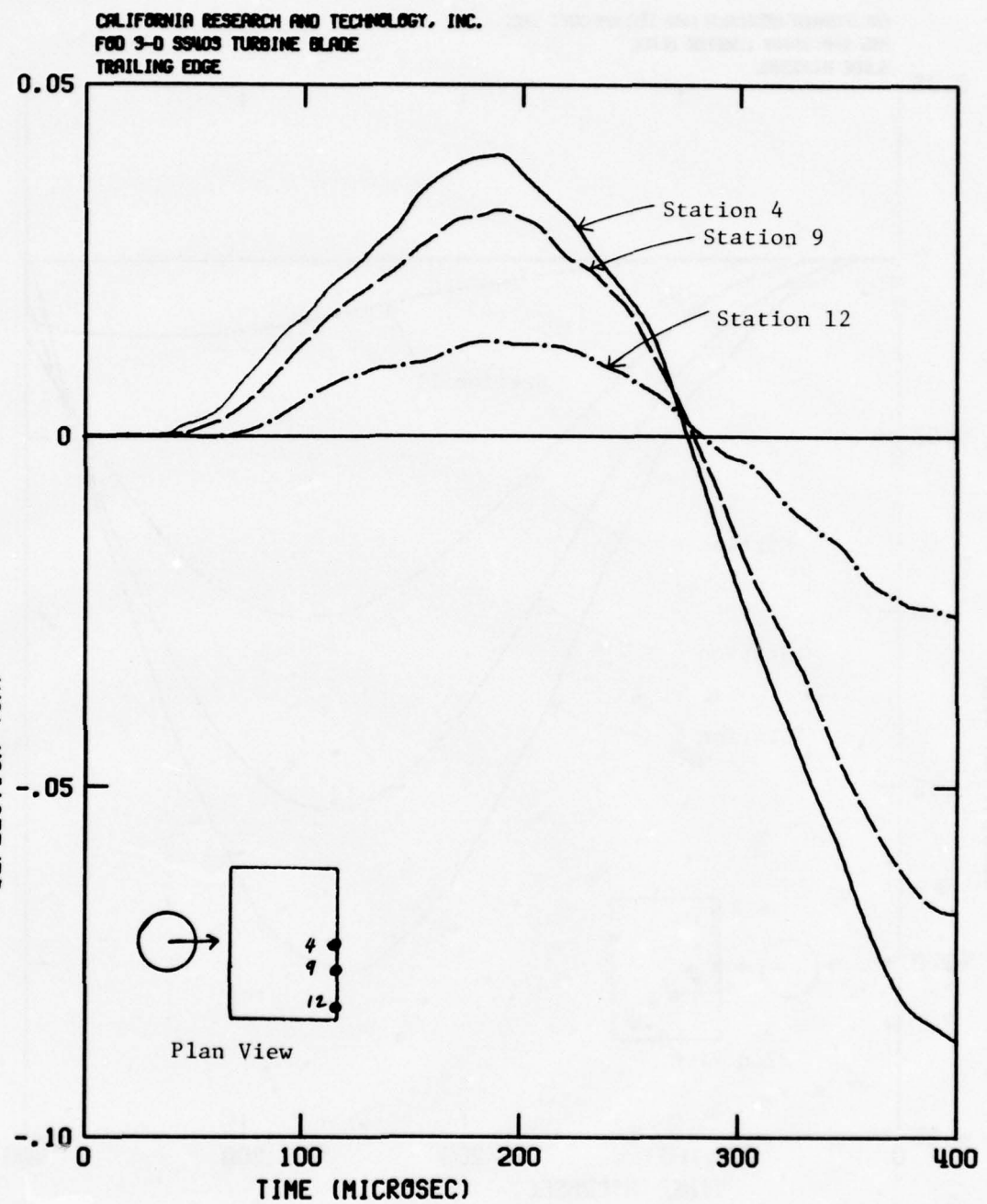


Figure 42. Vertical Displacement Histories at Selected Points Along Trailing Edge of Stainless Steel (SS403) Blade Impacted by 85-gm Water Sphere at 25° Obliquity (Case E)

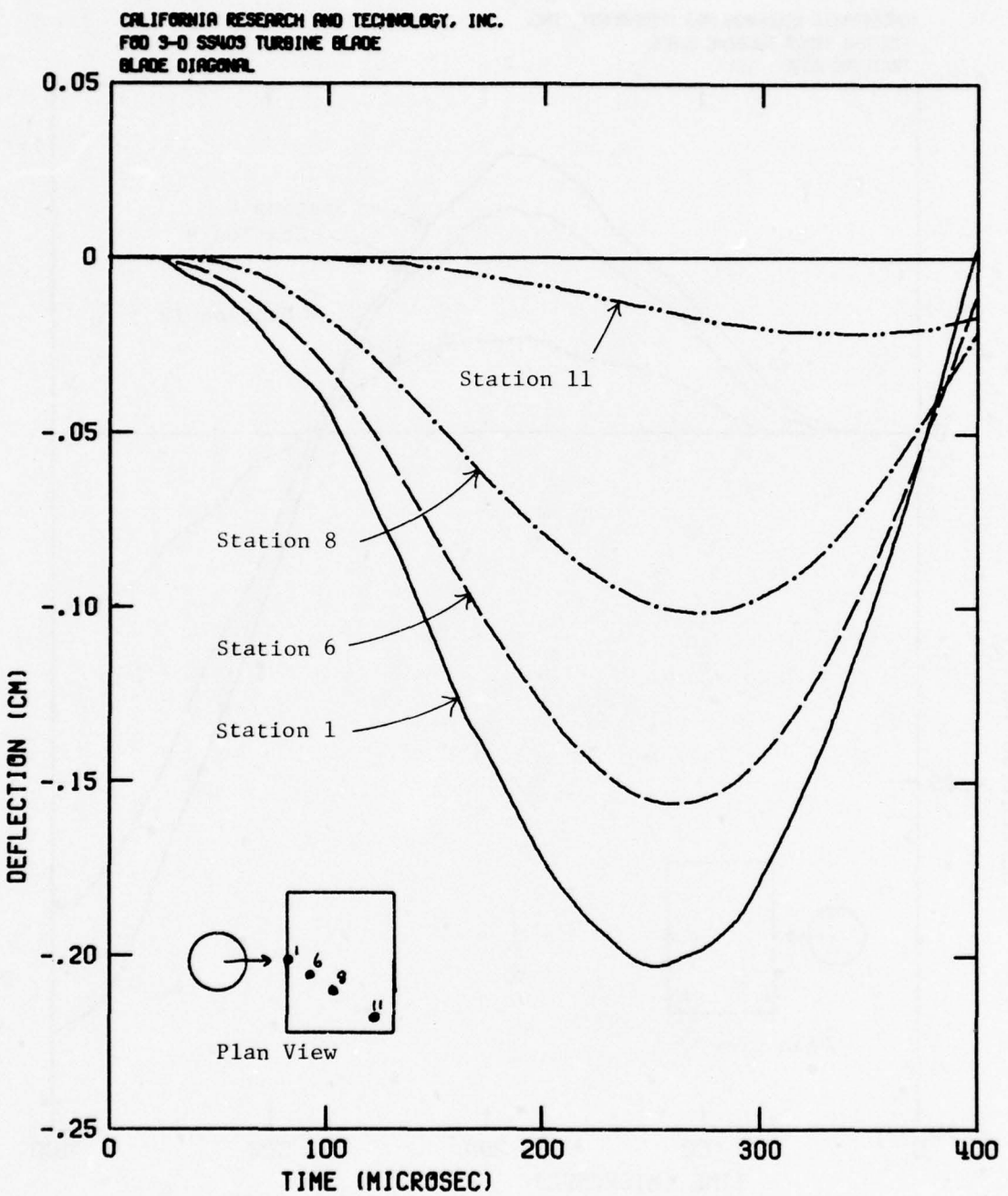


Figure 43. Vertical Displacement Histories at Selected Points on Surface of Stainless Steel (SS403) Blade After Impact of 85-gm Water Sphere at 25° Obliquity on Leading Edge (Case E)

250 μ sec for these stations. Figure 42 shows stations on the rear edge. The initial displacements are upward, with a maximum upward deflection of about 0.04 cm, occurring in less than 200 μ sec. This upward motion along the trailing edge is smaller than the subsequent peak downward motions. Figure 43 shows several interior stations. The stations further from the impact point have smaller peak deflections. Also note that the period seems to increase at points further from the impact.

2.3.2 Boron-Aluminum Blade

Figures 44 to 47 show displacement-time histories in the Boron-Aluminum blade segment. Quantitatively, the results are similar to the stainless steel blade; however, the peak deflections are somewhat larger. At the impact point, the Bo-Al peak deflection is 0.3 cm as compared to 0.2 cm for stainless steel. Also, the timing is somewhat different. The times to first maximum deflection are smaller by roughly 50 μ sec on both the leading and trailing edges of the Bo-Al blade.

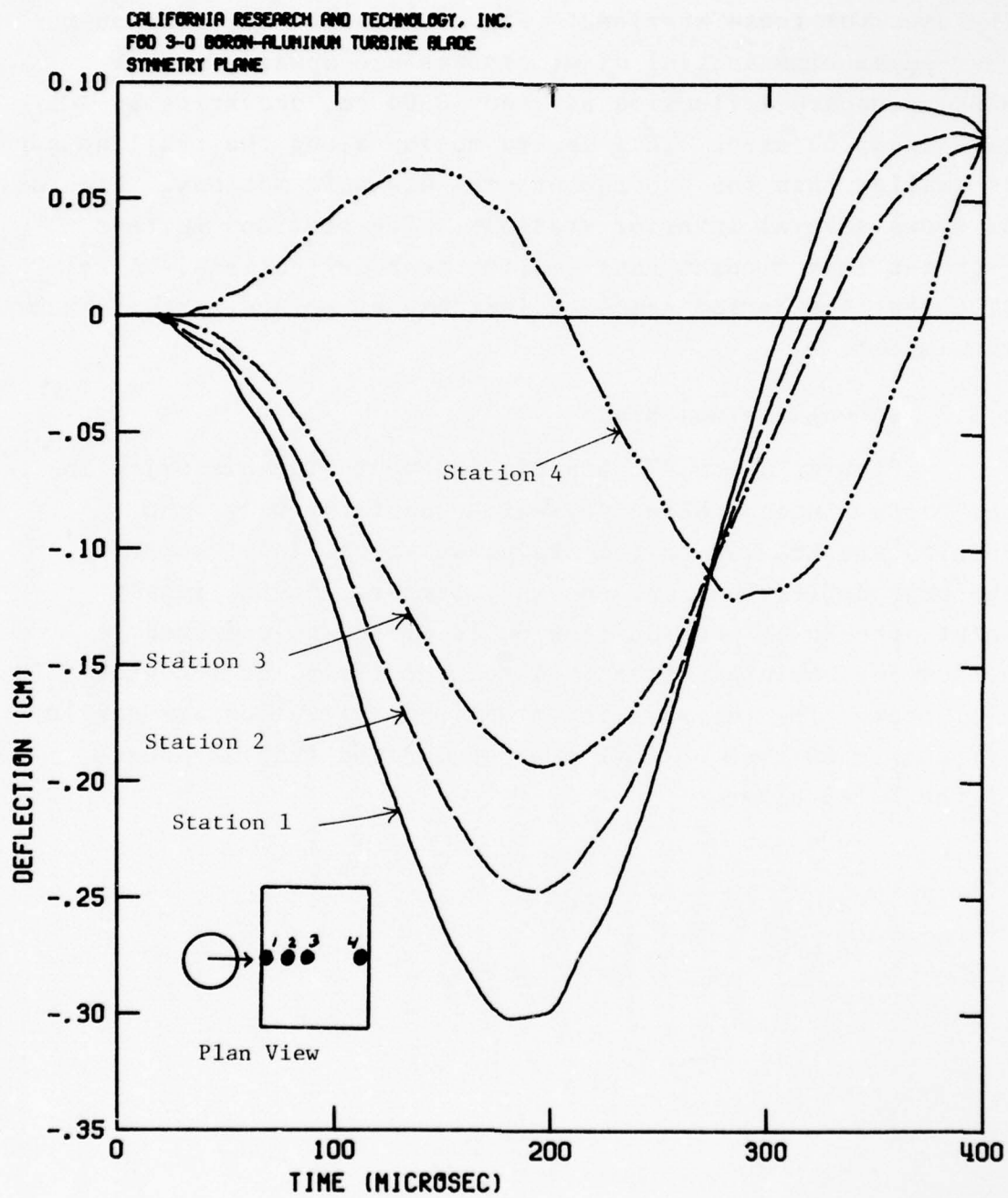


Figure 44. Vertical Displacement Histories at Selected Points
Downstream of Impact of 85-gm Water Sphere at 25°
Obliquity on Leading Edge of Bo-Al Blade (Case F)

CALIFORNIA RESEARCH AND TECHNOLOGY, INC.
FOD 3-0 BORON-ALUMINUM TURBINE BLADE
LEADING EDGE

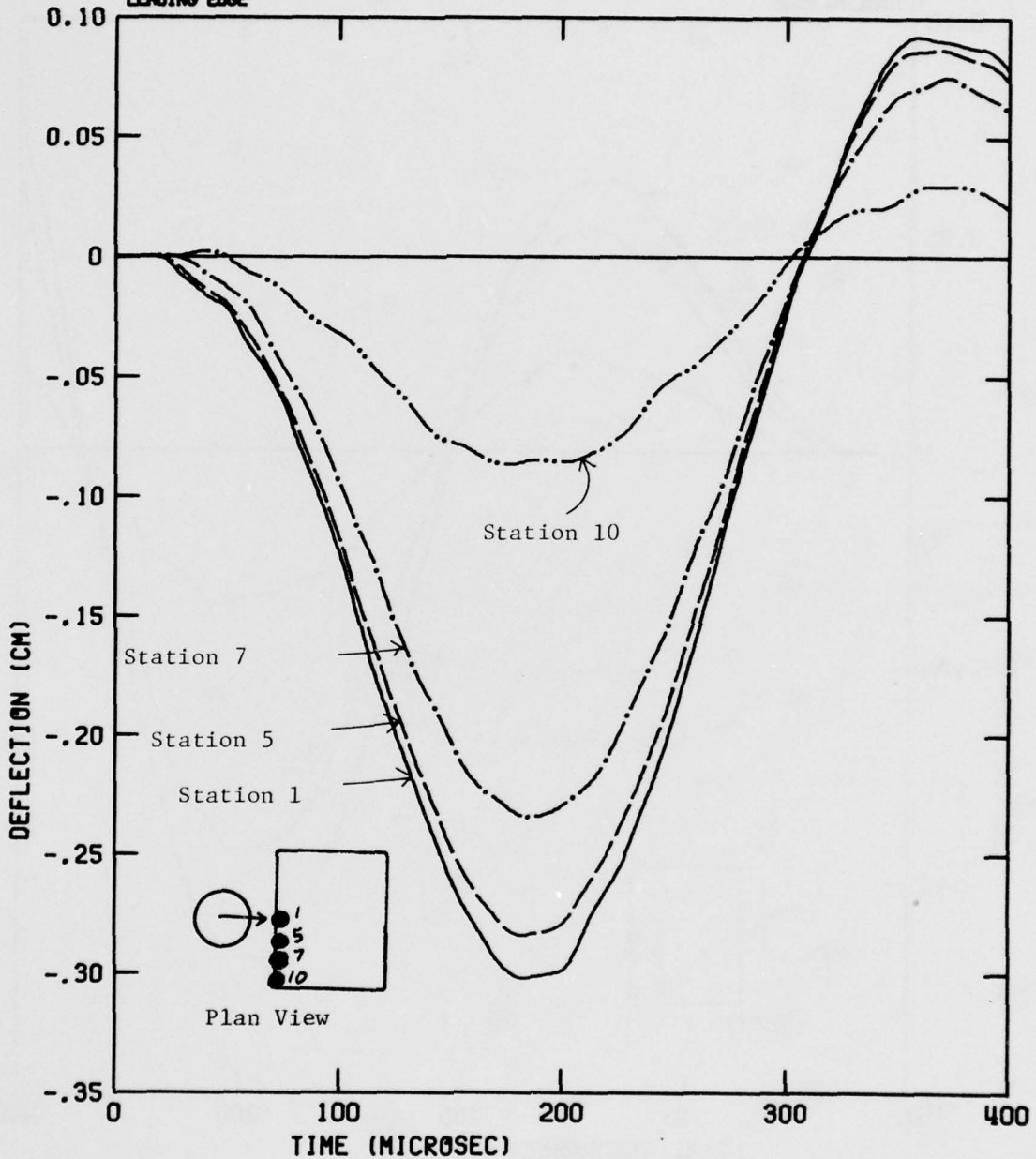


Figure 45. Vertical Displacement Histories at Selected Points Along Leading Edge of Bo-Al Turbine Blade Impacted on Leading Edge by 85-gm Water Sphere at 25° Obliquity (Case F)

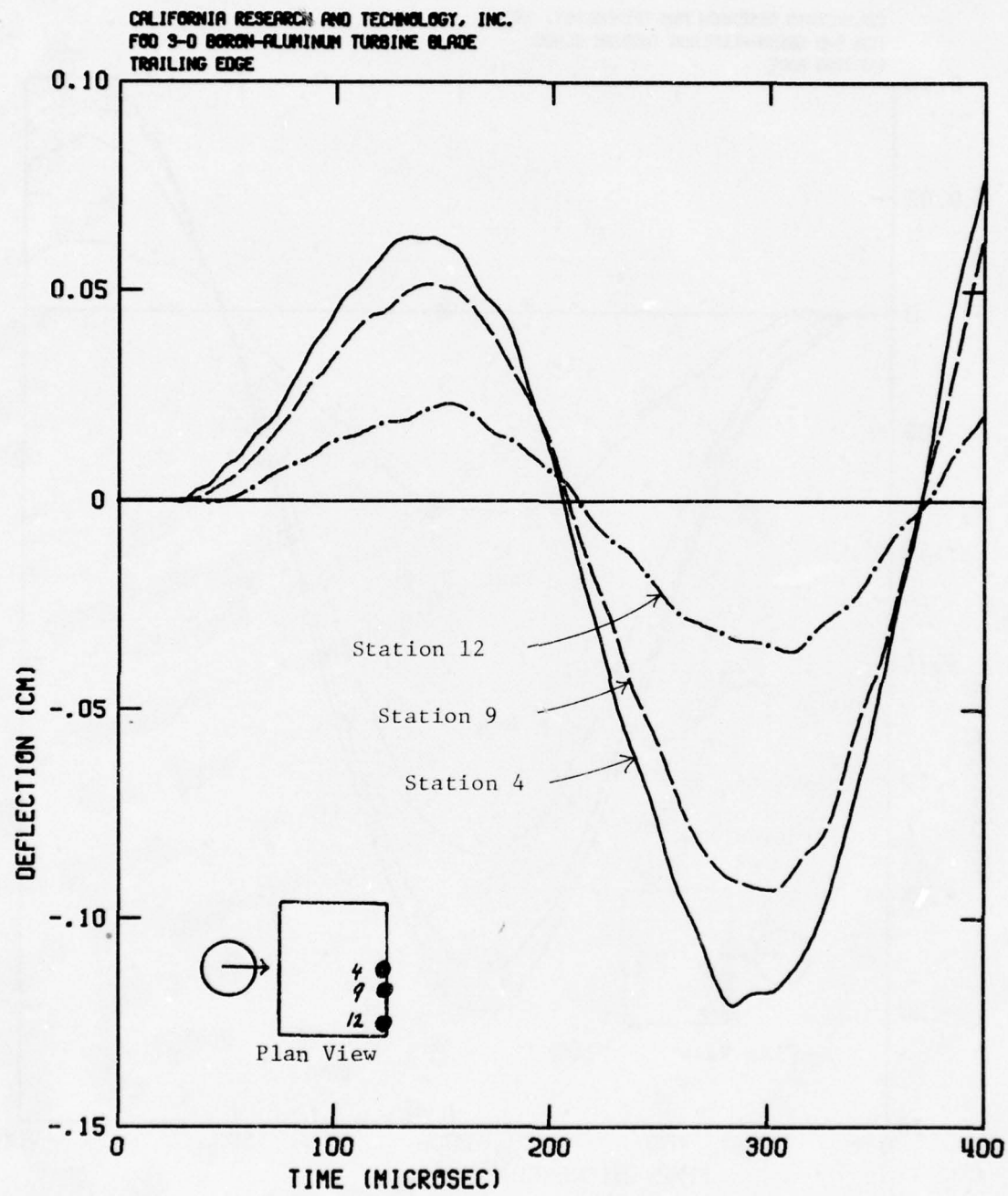


Figure 46. Vertical Displacement Histories at Selected Points Along Trailing Edge of Bo-Al Turbine Blade Impacted on Leading Edge by 85-gm Water Sphere at 25° Obliquity (Case F)

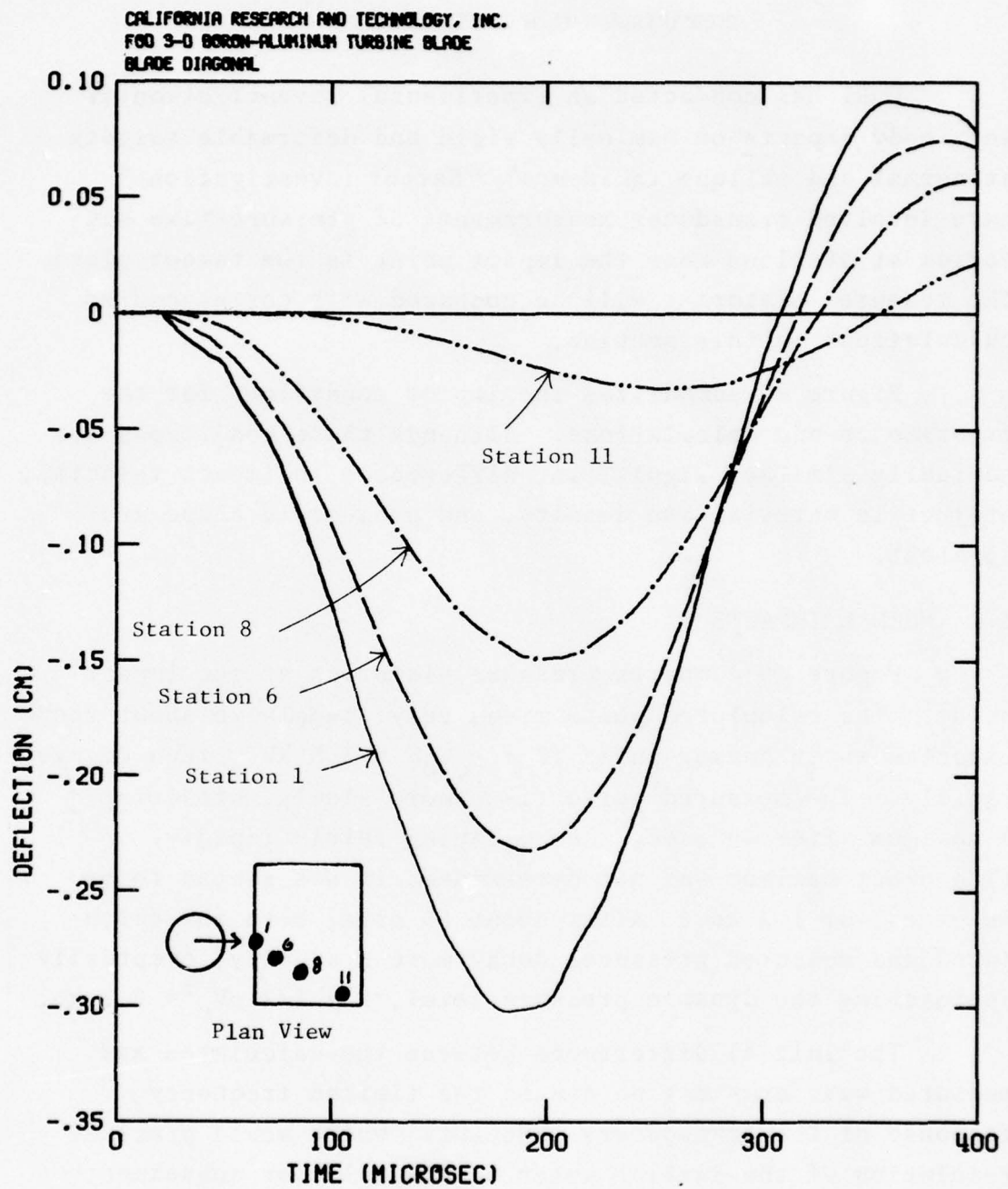


Figure 47. Vertical Displacement Histories at Selected Points on Surface of Bo-Al Turbine Blade Impacted on Leading Edge by 85-gm Water Sphere at 25° Obliquity (Case F)

SECTION III
COMPARISONS WITH EXPERIMENTS

UDRI has conducted an experimental investigation of soft body impacts on nominally rigid and deformable targets at normal and oblique incidence³. Recent investigations⁶ have involved transducer measurements of pressure-time histories at stations near the impact point in the target plate. The measured histories will be compared with corresponding calculations in this section.

Figure 48 summarizes the impact conditions for the experiments and calculations. Although these conditions are nominally similar, significant differences in impact velocity, projectile material and density, and projectile shape are apparent.

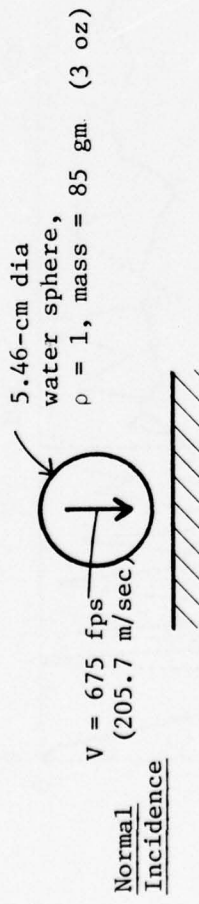
3.1 NORMAL IMPACTS

Figure 49 compares pressure histories at the impact point. The calculated pulse rises very steeply to about the expected water hammer pulse ($P_M = \rho_0 V_0 C = 2.8 \text{ kb}$), then decays rapidly. The measured pulse rises more slowly, attaining a maximum after 40 μsec , then decaying fairly rapidly. (The exact maximum was not determined; it was stated to be in excess of 1.5 kb.) After about 50 μsec , both the calculated and measured pressures decay more gradually, eventually approaching the dynamic pressure level, $P = 1/2 \rho V_0^2 \approx 0.2 \text{ kb}$.

The initial differences between the calculated and measured waveforms may be due to the limited frequency response of the transducers (100 kHz), which would preclude resolution of the initial water hammer pulse or subsequent rapid decay.

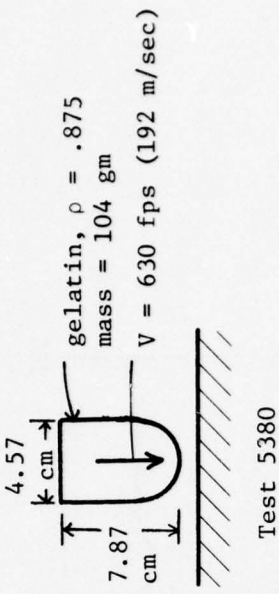
The oscillations in the numerical results can be smoothed if more artificial viscosity is used in these

CALCULATIONS:

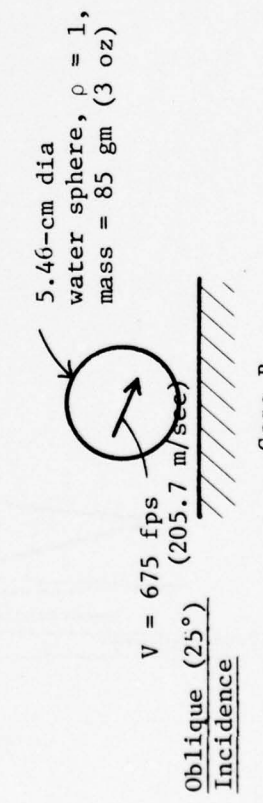


Case A

EXPERIMENTS:



Case A



Case B

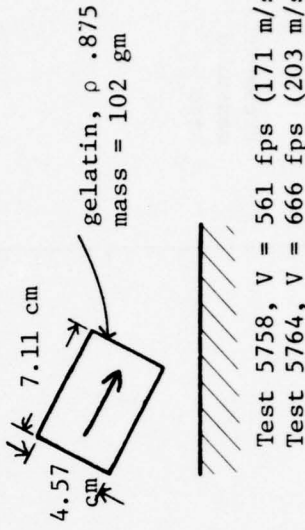


Figure 48. Summary of Impact Conditions for Calculations and Experiments

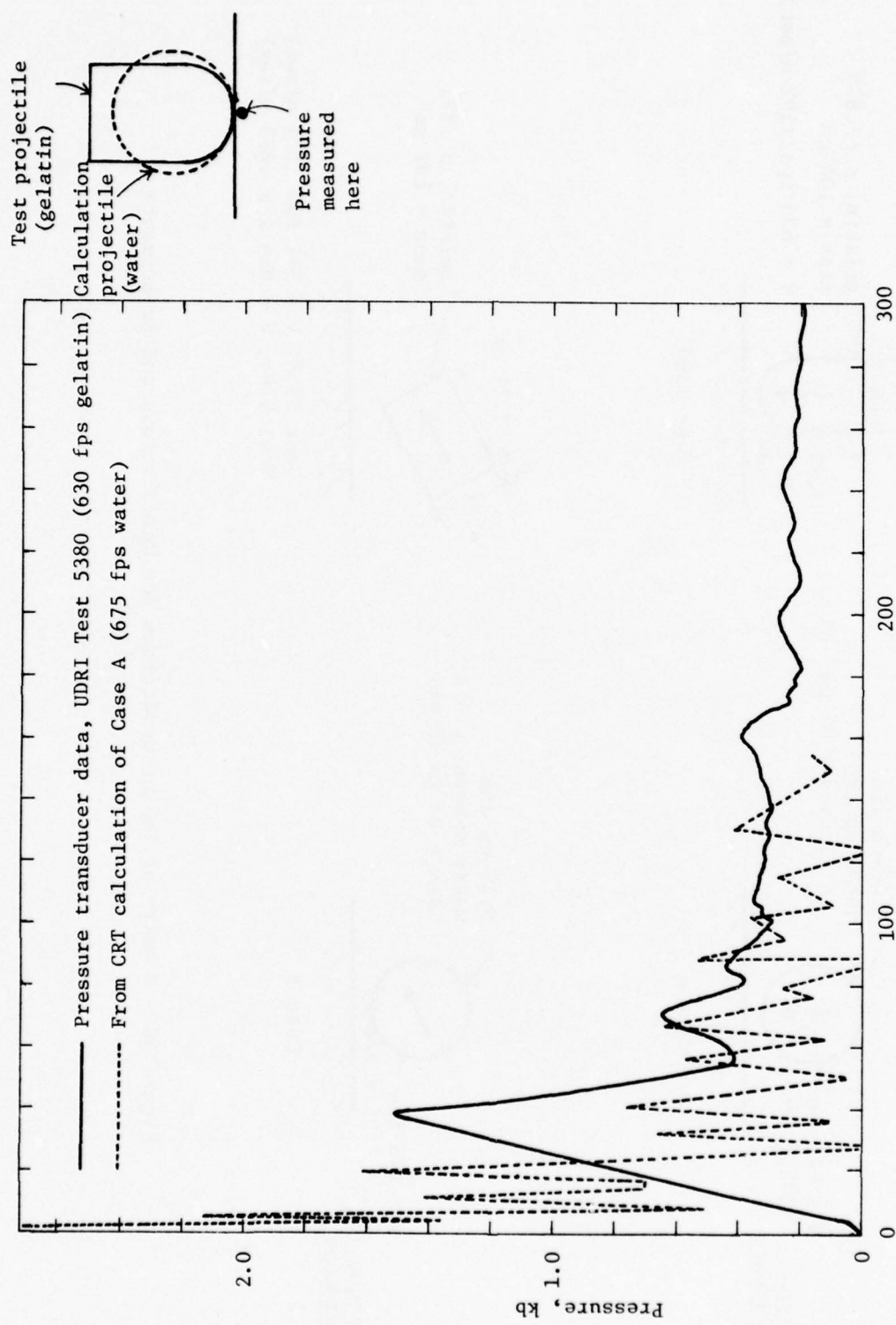


Figure 49. Comparison of Calculated and Measured Pressure Histories at Impact Point: Normal-Incidence Impacts on Rigid Surface

type analyses. Only a minimum of such viscosity was used in Case A, so as to allow the early pressure spike to more accurately develop.

Figures 50 and 51 compare measured and calculated pressure histories at stations 1/2-in. and 1-in. from the impact point, respectively. The experimental data has been shifted in time to agree with the expected time delay associated with stations at 1/2-in. and 1-in. from the impact. The comparisons for these stations are very good.

3.2 OBLIQUE IMPACTS

The oblique impact comparisons between calculated and measured pressure pulses are not as meaningful because of the distinct differences in projectile shape (sphere vs right cylinders) and the velocity variation between the two tests. Figure 52 shows the pressure pulses measured at three stations: at the impact center (i.e., intersection of the cylinder axis with the target surface), and at points 1-in. "upstream" and "downstream" from that point. None of the pulses show a water hammer spike. All rise relatively slowly, and remain fairly constant thereafter. However, the pressure levels are substantially different. The upstream station attains a pressure level of about 110 bars. This is below the dynamic pressure corresponding to the full velocity for the gelatin impact, i.e., $P = 1/2\rho V_o^2 = 180$ bars), but it is far above the dynamic pressure corresponding to the normal component of the velocity, $P = 1/2\rho (V_o \sin\theta)^2 = 32$ bars. The center-line and downstream stations attain pressures which correspond closely to the latter, i.e., $P = 1/2\rho(V_o \sin\theta)^2$. This behavior is qualitatively consistent with the tentative observation in Reference 7 that dynamic

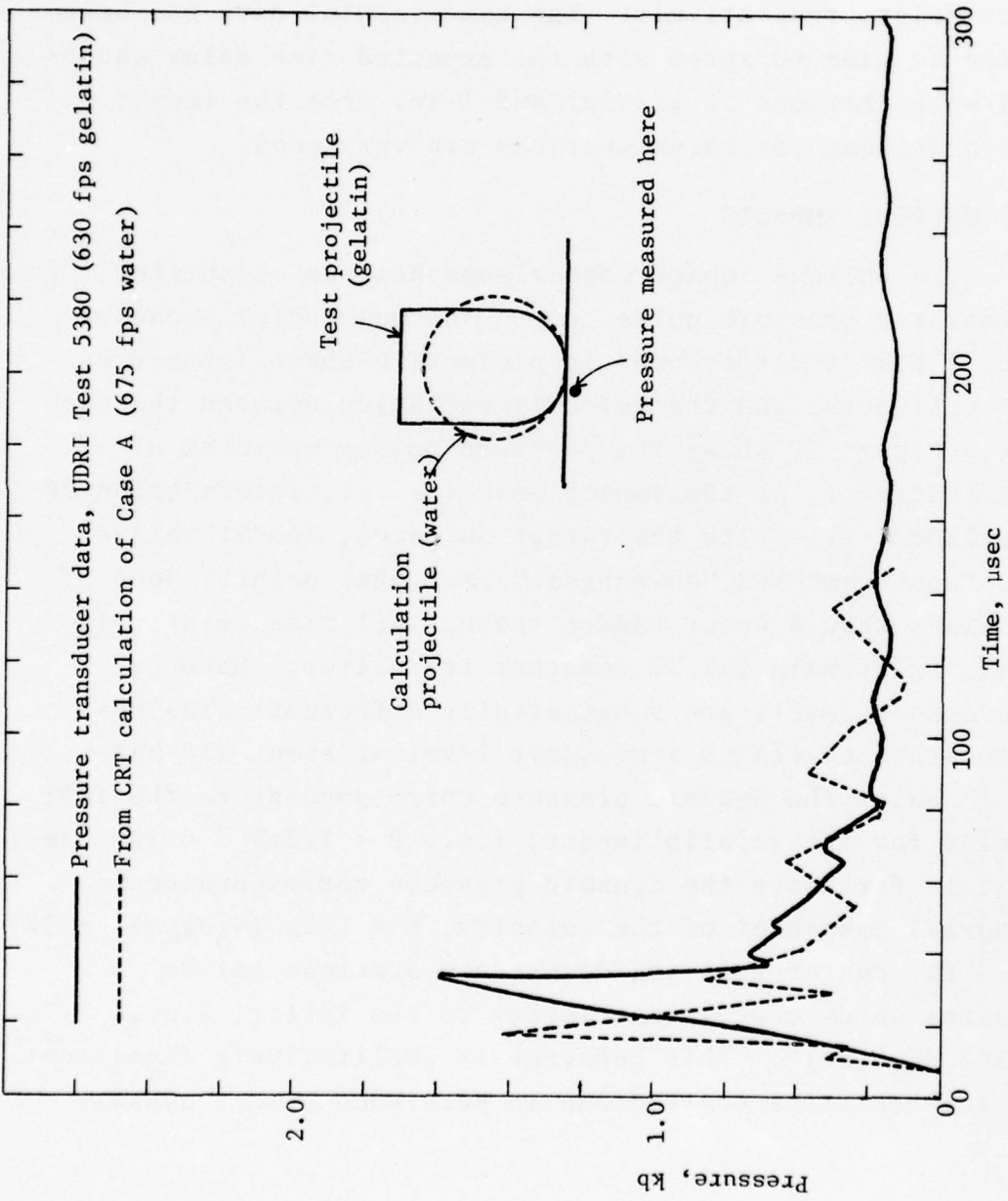


Figure 50. Comparison of Calculated and Measured Pressure Histories in Target Surface 12.7 cm (1.5 in) from Impact Point: Normal-Incidence Impacts on Rigid Surface

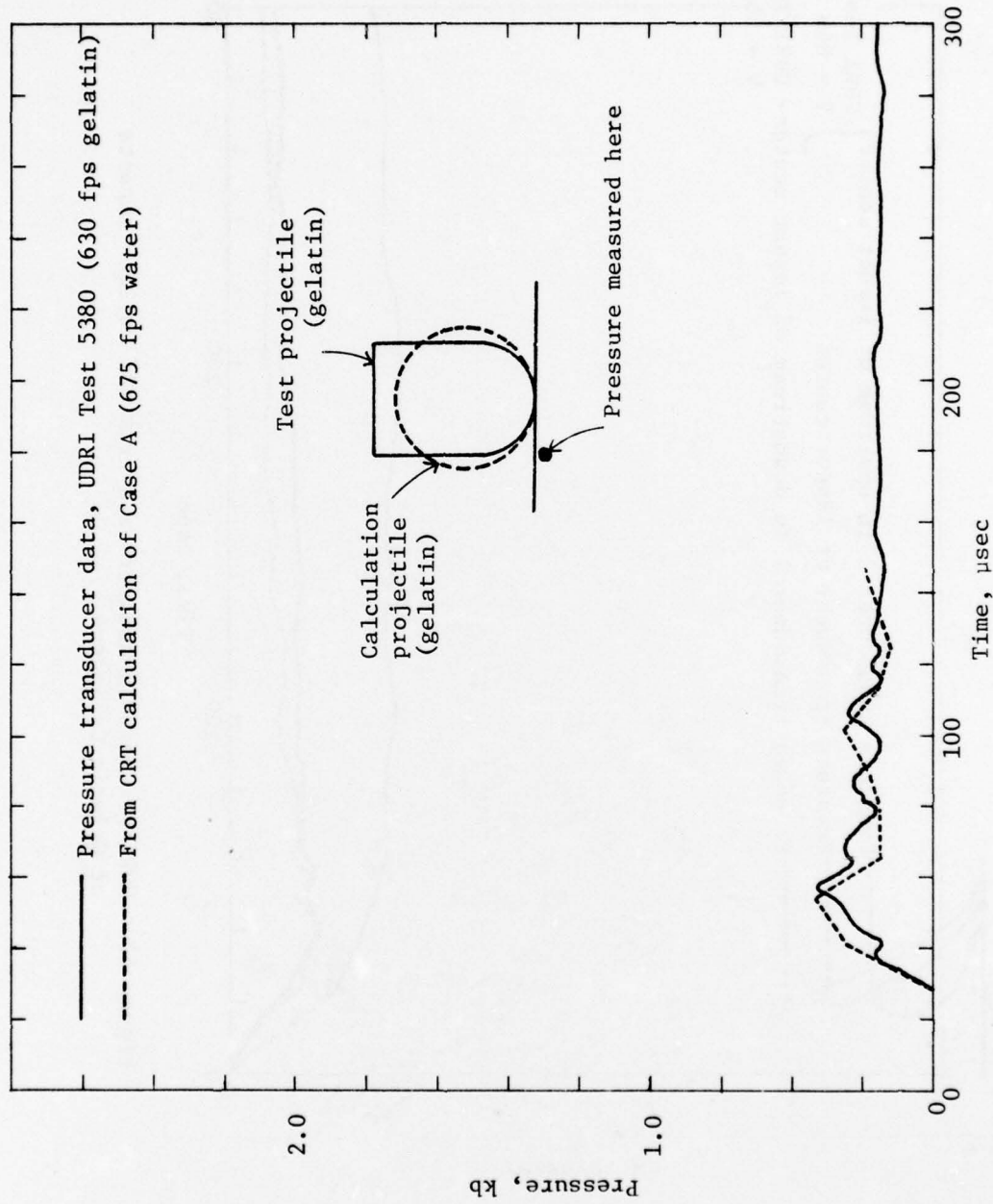


Figure 51. Comparison of Calculated and Measured Pressure Histories in Target Surface 25.4 cm (1 in) from Impact Point: Normal-Incidence Impacts on Rigid Surface

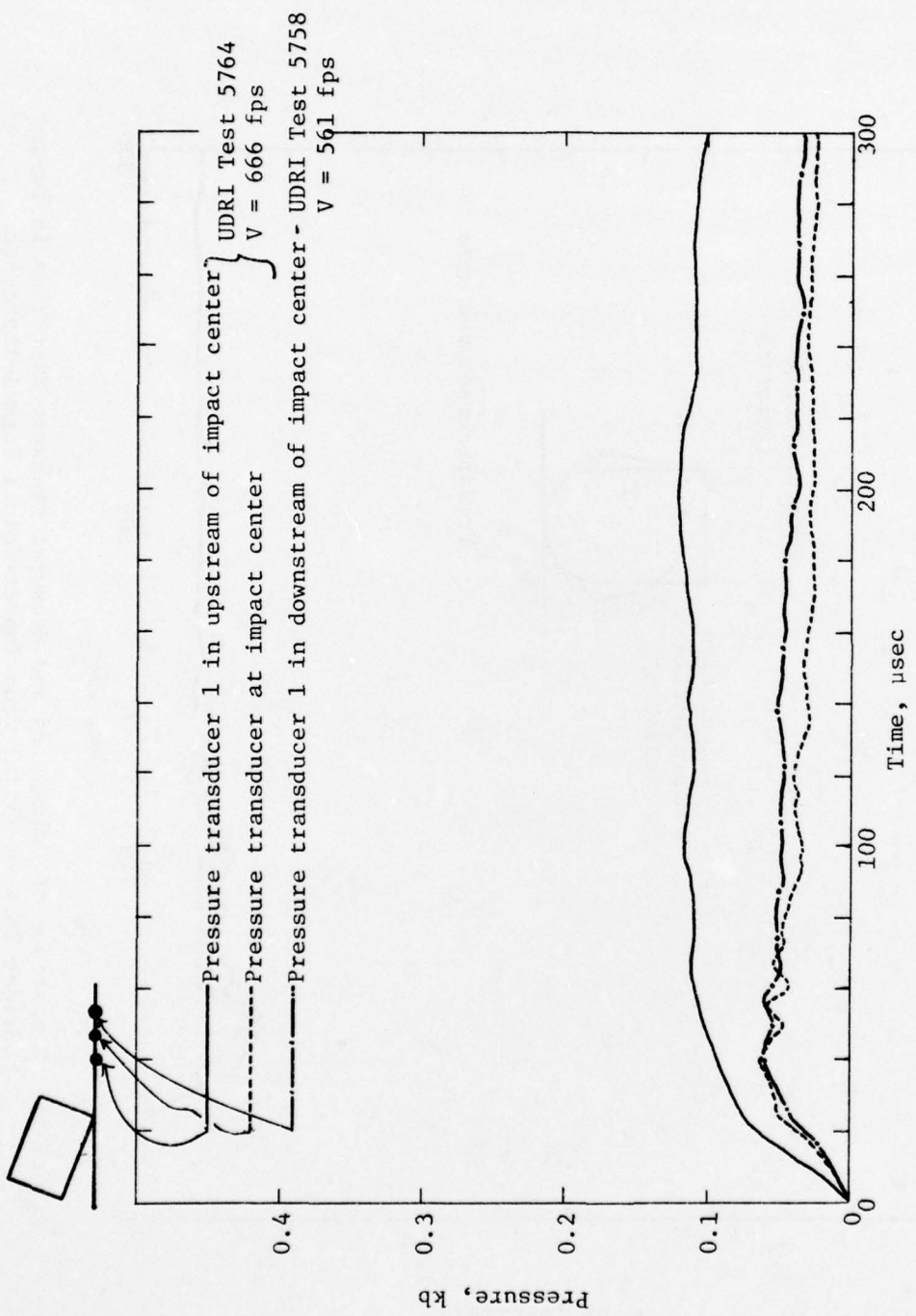


Figure 52. UDRI Pressure Transducer Data from 25° Oblique Impacts
of Gelatin Cylinders

pressures in substantially oblique impacts of cylinders approach $1/2\rho V_0^2$ at points on the upstream side of the stagnation point (which is upstream of the center-line intersection), and $1/2(V_0 \sin\theta)^2$ on the downstream side.

Figure 53 compares the calculated pulse (for a spherical water drop impact-Case B) with the measured pulse (for the gelatin cylinder) at the upstream station. *The waveforms are qualitatively very different.* The calculated pulse rises sharply to about 400 kbars, then decays gradually, reaching the 20-40 bar level by 15 μ sec. The measured pulse climbs gradually to 100-110 bars, and remains nearly constant at that level for 300 μ sec. These different behaviors indicate that geometry of the impacting body has a potentially important influence on the loading pulse.

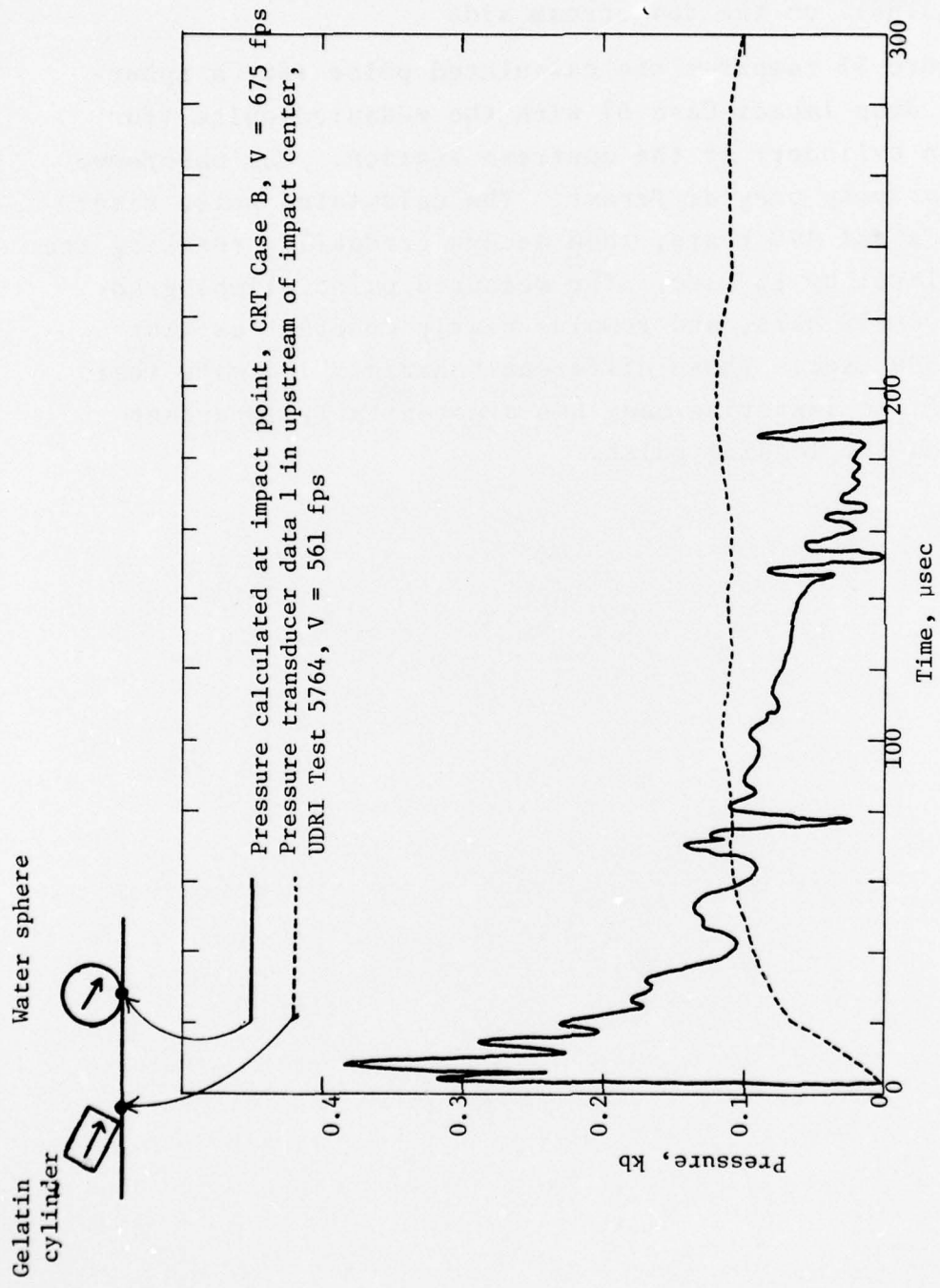


Figure 53. Comparison of Calculated and Measured Pressure Histories in Target Surface: 25° Oblique Impacts on Rigid Surface

SECTION IV
CONCLUSIONS AND RECOMMENDATIONS

The quantitative and qualitative results of this study demonstrate the detailed nature of the temporal and spatial descriptions which can be obtained with numerical codes for the dynamic impact phenomena involved in soft body impacts. Normal impacts on rigid or deformable plates can be treated from first principals using the 2-D finite difference WAVE-L code. Oblique impacts are more difficult to analyze because these impacts are generally 3-D in nature. For the case of a nominally-spherical body obliquely impacting an essentially frictionless surface which does not substantially distort during loading, a Galilean coordinate transformation (see Appendix B and Section 2.2) can be used to transform the 3-D oblique impact into an approximately equivalent 2-D axisymmetric impact problem. This transformation technique was applied to oblique impacts of spherical projectiles into rigid and semi-rigid targets. For oblique impact cases involving large target deformations, the technique is not applicable.

The time-resolved force loading functions from 675 fps normal and oblique soft body impacts on rigid and 0.136-in. stainless steel plates can be used to load complete 3-D finite element models of turbine blades, including the root design. Cases E and F in this study examined the local behavior in 3-D of a section of a turbine blade for an edge-on impact at 25°. A similar approach could be taken using a more complete 3-D finite element blade description.

Potentially important differences were seen between calculated loading pulses for obliquely-impacting spheres, and measured pulses for obliquely-impacting cylinders. The differences in these relatively low-velocity impacts are thought to be due to projectile geometry effects.

The following recommendations are made for additional efforts directed toward understanding the soft body (bird) impact problems:

1. Develop realistic material models for birds -

The numerical codes can be used to develop and/or evaluate material and loading models for the soft body impacts on aircraft components. In particular, the porosity muscle/skin strength, and bone structure of birds may influence impact loading and local damage mechanisms. Code solutions provide a precise and controllable approach for understanding the role of these properties, and can thereby lead to development of simpler models.

2. Investigate the importance of projectile shape factors -

Codes can directly evaluate differences in the force loading on a target for various shapes corresponding to possible bird impacts. This information is needed not only to evaluate the range of impact loading which can be expected for different birds and impact orientations, but also to help design realistic simulants.

3. Develop a rapid technique for using the early impact phenomena and force loading descriptions -

This is needed to allow for efficient 3-D finite element code prediction of survivability of turbine blade designs.

APPENDIX A

MATERIAL PROPERTIES

1. MATERIAL MODEL FOR TYPE 403 STAINLESS STEEL (SS403)

The material properties for SS403 described below have been chosen to match as closely as possible the properties of the steel being used in the experimental work³, which was specified by the supplier to have an ultimate tensile strength of 75520 psi, and a yield stress of 36540 psi.

The stress levels encountered in the present effort are such that an elastic-plastic material model is appropriate. Within the yield surface, deformations are considered to be elastic; excursions on the yield surface are made in accordance with the Prandtl-Reuss flow rule. The location of the yield surface for a material element is a function of the local generalized plastic strain 0, ϵ_p , where

$$\epsilon_p = \int_0^t \sqrt{\frac{2}{3} \dot{\epsilon}_{ij}^p \dot{\epsilon}_{ij}^p} dt$$

and $\dot{\epsilon}_{ij}^p$ is the plastic strain rate. Work hardening is thus included in the model. The elastic constants used in the model are given in Table A-1.

TABLE A-1. ELASTIC CONSTANTS FOR TYPE 403
STAINLESS STEEL

Young's Modulus	28.5×10^6 psi
Poisson's Modulus	0.285
Shear Modulus	11.1×10^6 psi
Bulk Modulus	22.1×10^6 psi

Figure A-1 shows a simple tension stress-strain curve for stainless steel taken from Reference 8. The yield stress (corresponding to 0.2% offset) is close to the value given for the steel used in the experiment. This curve was monotonically extended to the point of failure, which is taken to be 75520 psi at 30% strain. For efficient use in the solutions, the curve has been fit by a line segment and two parabolic segments, as shown in Figure A-2. The equations for the analytical fit are:

$$\sigma = a_0 e \text{ for } 0 \leq e \leq 0.9875$$

$$\sigma = -b_1 + b_1^2 - 4a_1(c_1 - e) / 2a_1 \text{ for } 0.9875 < e \leq .33$$

$$\sigma = -b_2 + b_2^2 - 4a_2(c_2 - e) / 2a_2 \text{ for } 0.33 < e \leq .30$$

where $a_0 = 2.857 \times 10^5$ psi

$$a_1 = 1.472 \times 10^{-9} \text{ psi}^{-2}, a_2 = 1.871 \times 10^{-8} \text{ psi}^{-2}$$

$$b_1 = 7.012 \times 10^{-5} \text{ psi}^{-1}, b_2 = -1.335 \times 10^{-3} \text{ psi}^{-1}$$

$$c_1 = .9202, c_2 = 24.14$$

2. WATER EQUATION OF STATE

The numerical fit of Walker and Sternberg⁹ is used for the equation of state of water. This equation of state of water is valid to about 250 kbars. Figure A-3 shows the Water Hugoniot up to 50 kbars.

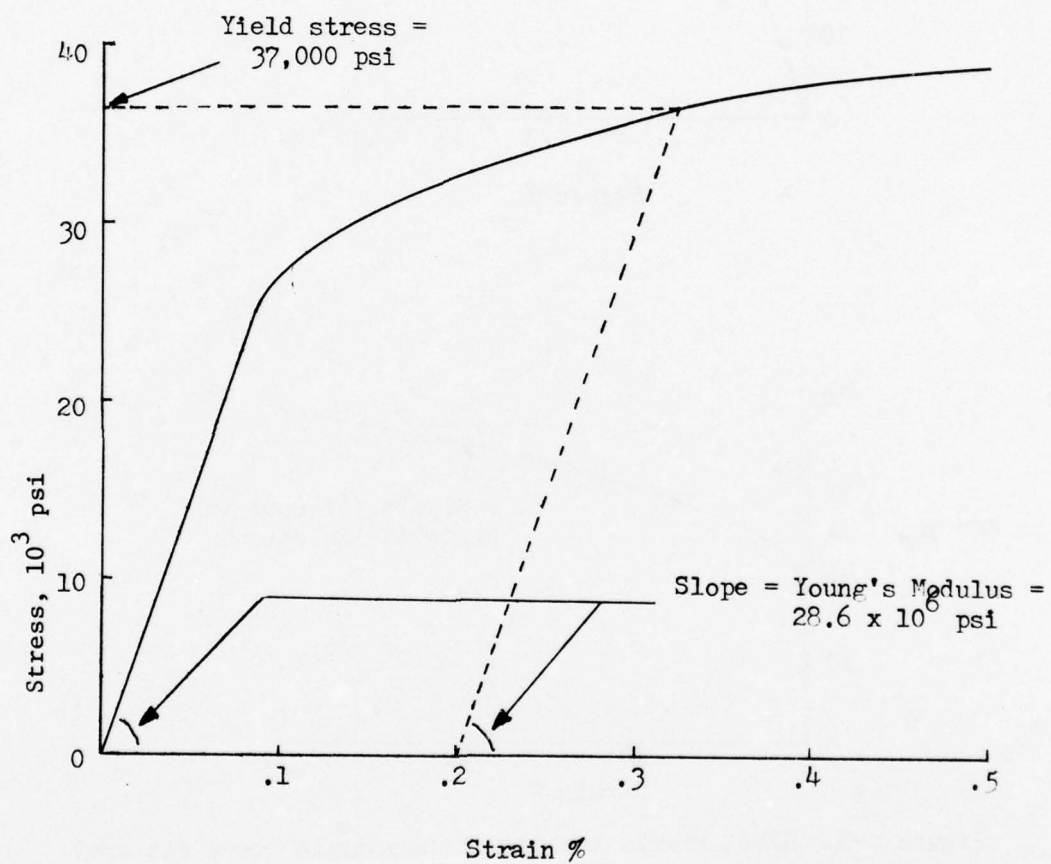


Figure A-1. Simple tension stress-strain function for annealed stainless steel, from Watter and Lincoln (Ref. 8)

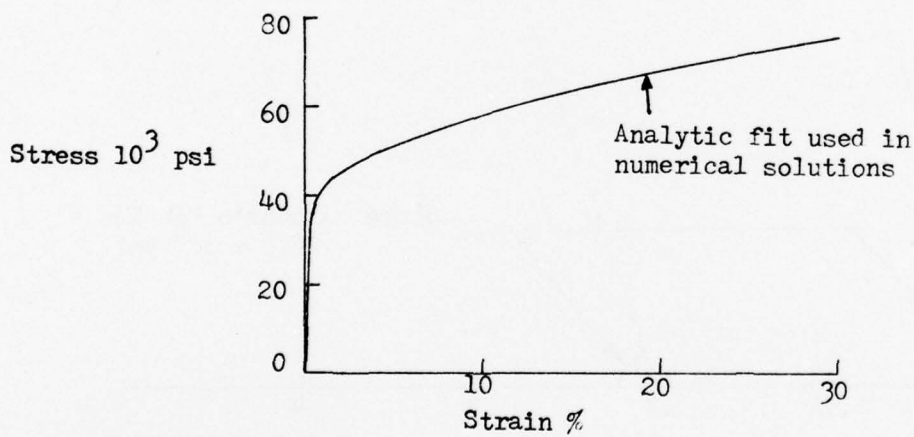
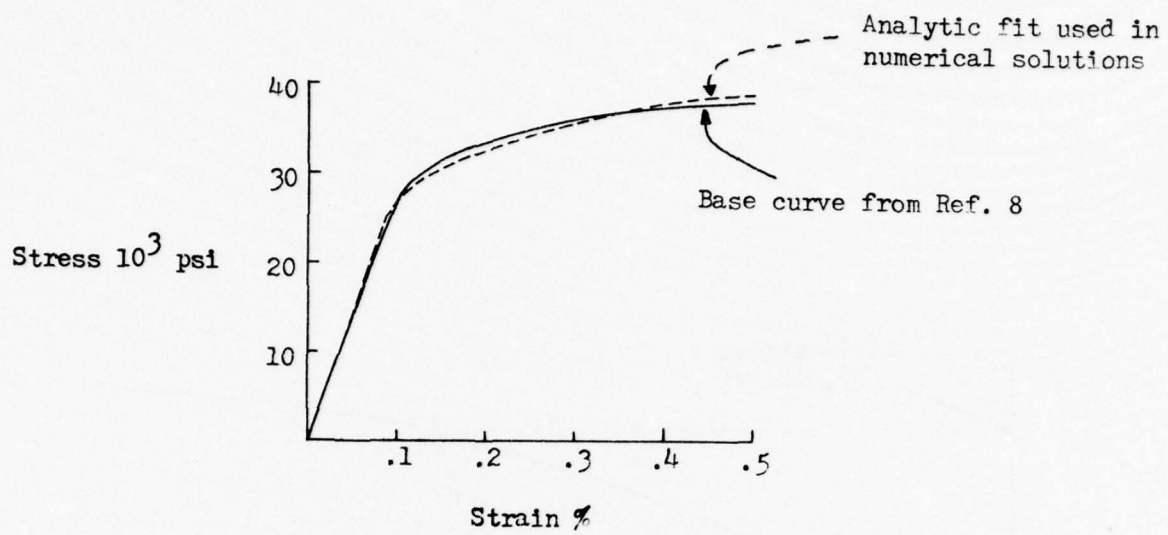


Figure A-2. SS403 simple tension stress-strain curve fit used in the numerical solutions showing the comparison with the base curve from Watter and Lincoln (Ref. 8) and the extrapolation to large strains

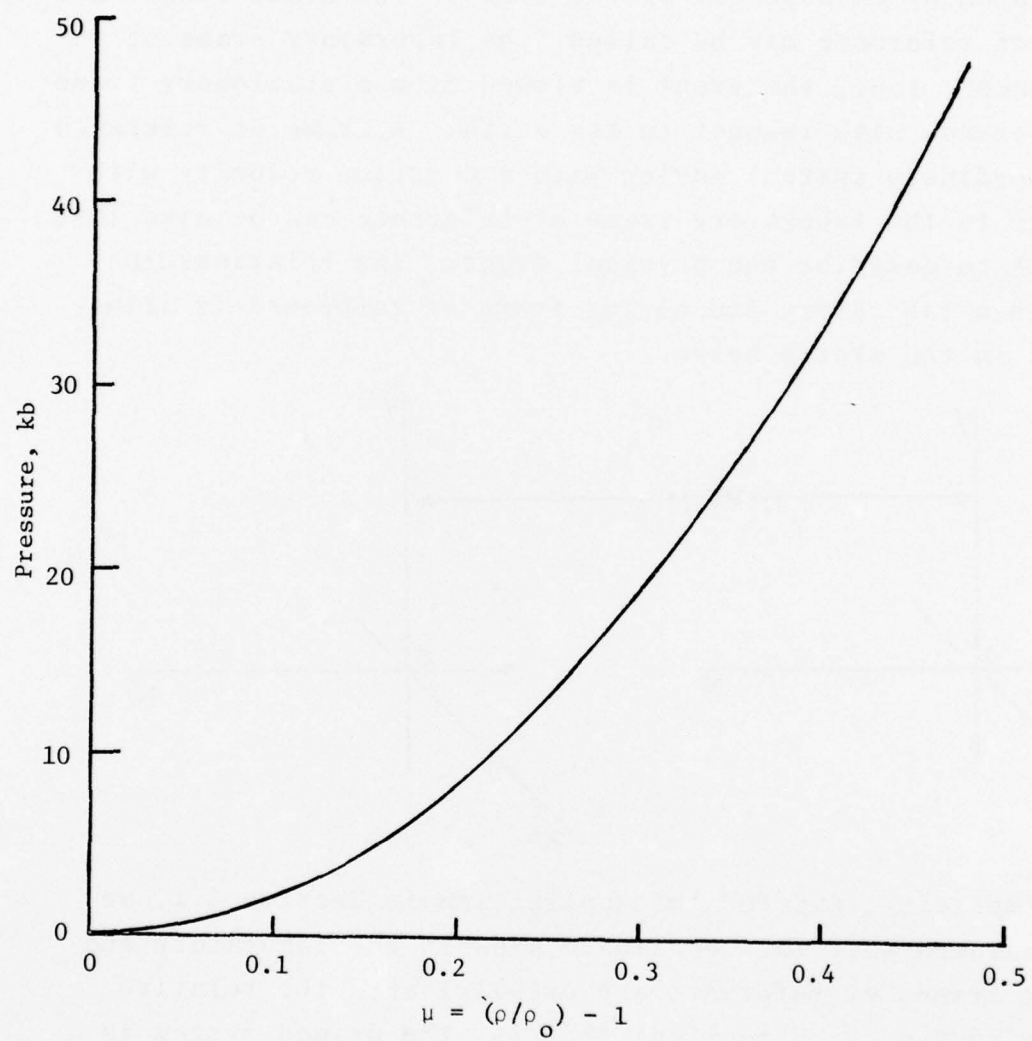
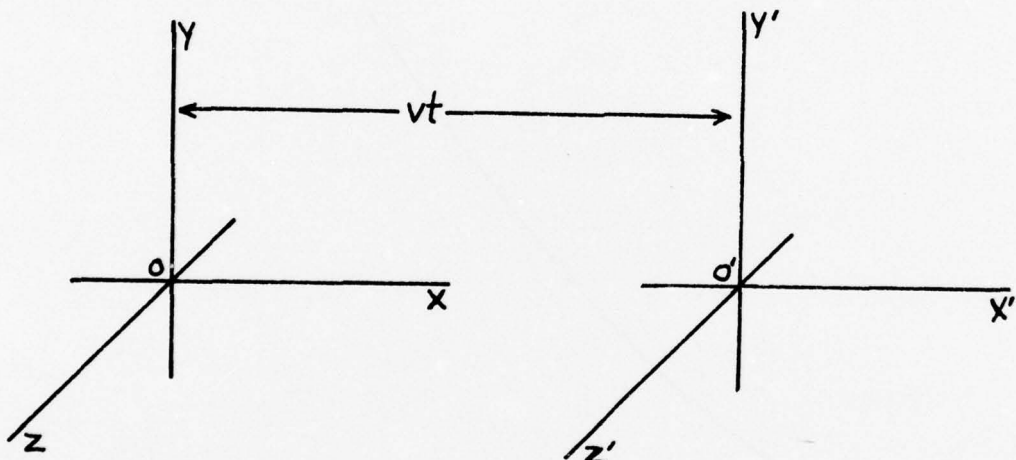


Figure A-3. Hugoniot Conditions for Water

APPENDIX B
GALILEAN COORDINATE TRANSFORMATION

A physical event, such as the impact of a soft body on a plate, cannot be influenced by the particular coordinate frame used by an observer of the event. The usual coordinate frame of reference may be called "the laboratory frame of reference", i.e., the event is viewed from a stationary frame of reference with respect to the earth. A frame of reference (or coordinate system) moving with a constant velocity with respect to the laboratory frame of reference can be used just as well to describe the physical event. The relationship between a laboratory and moving frame of reference is illustrated in the sketch below.



For simplicity, and for the application in Section 2.1, we have assumed that the coordinate axes in the laboratory and moving frames of reference are parallel with the relative motion in the x direction; that is, the primed system is moving in the x direction with speed v relative to the unprimed system.

Now if the two origins O and O' are coincident at time $t = 0$, then the distance OO' is equal to vt . The equations of transformation, according to classical or Newtonian kinematics, are then

$$\begin{aligned}x &= x' + vt \\y &= y' \\z &= z' \\t &= t'\end{aligned}$$

where x, y, z, t , are in the laboratory system, and x', y', z' , and t' are the coordinates of the moving frame of reference.

Velocities in the two frames of reference are then related by

$$\begin{aligned}\dot{x} &= \dot{x}' + v \\ \dot{y} &= \dot{y}' \\ \dot{z} &= \dot{z}'\end{aligned}$$

Thus the dynamic results of a physical event in one coordinate frame is sufficient to completely determine the dynamics in the other frame of reference.

REFERENCES

1. Mark L. Wilkins, "Calculation of Elastic-Plastic Flow", UCRL-7322 Rev. 1, Lawrence Livermore Laboratory, Livermore, California, January 1969
2. Klaus-Jurgen Bathe, Edward L. Wilson, and Robert H. Iding, "NONSAP - A Structural Analysis Program for Static and Dynamic Response of Nonlinear Systems", UC SESM 74-3, Structural Engineering Laboratory, University of California, Berkeley, California, February 1974
3. John P. Barber, John M. Klyce, Philip F. Fry, and Henry R. Taylor, "Impact of Soft Bodies on Jet Engine Fan Blades", UDRI-TR-76-33, University of Dayton Research Institute, Dayton, Ohio, June 1976
4. Yen C. Huang, F. G. Hammitt, and W-J Yang, "Hydrodynamic Phenomena During High-Speed Collision Between Liquid Droplet and Rigid Plane", Transactions of the ASME, Journal of Fluids Engineering, June 1973, pp. 276-294
5. M. C. Rochester and J. G. Brunton, "Surface Pressure Distribution During Drop Impingement", Proceedings of the Fourth International Conference on Rain Erosion, and Associated Phenomena, Meersburg, West Germany, May 1974
6. Personal communication of unpublished data, John Barber, University of Dayton Research Institute
7. Richard L. Peterson and John P. Barber, "Bird Impact Forces in Aircraft Windshield Design", unpublished manuscript, Air Force Flight Dynamics Laboratory, Wright-Patterson Air Force Base, Ohio
8. M. Watter and R. A. Lincoln, Strength of Stainless Steel Structural Members as Function of Design, Allegheny Ludlum Steel Corp., Pittsburg, Pennsylvania, 1950
9. W. A. Walker and H. M. Sternberg, "The Chapman-Jouget Isentrope and the Underwater Shockwave Performance of Pentolite", The Fourth Symposium on Detonation, Naval Ordnance Laboratory, White Oak, Maryland, October 1965